



2  
2007



This is to certify that the  
thesis entitled

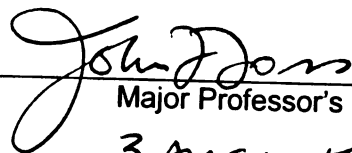
Intermittency and the Viscous Superlayer in a Single Stream  
Shear Layer

presented by

Aren Hellum

has been accepted towards fulfillment  
of the requirements for the

    M.S.     degree in     Mechanical Engineering    

  
Major Professor's Signature

    3 August 2006    

Date

**PLACE IN RETURN BOX** to remove this checkout from your record.  
**TO AVOID FINES** return on or before date due.  
**MAY BE RECALLED** with earlier due date if requested.

<b>DATE DUE</b>	<b>DATE DUE</b>	<b>DATE DUE</b>

INTERMITTENCY AND THE VISCOUS SUPERLAYER IN A SINGLE  
STREAM SHEAR LAYER

By

Aren Hellum

A THESIS

Submitted to

Michigan State University

in partial fulfillment of the requirements

for the degree of

Master of Science

Department of Mechanical Engineering

2006

## ABSTRACT

### INTERMITTENCY AND THE VISCOUS SUPERLAYER IN A SINGLE STREAM SHEAR LAYER

By

Aren Hellum

Time resolved velocity and vorticity measurements have been made in a high Reynolds-number Single Stream Shear Layer (SSSL). This work was motivated by interest in the Viscous Superlayer (VSL). The VSL is a thin interface region between vortical and non-vortical fluid. Processing algorithms were developed which allowed vorticity information to be used to locate the flow at time  $t$  on either the “vortical” or “non-vortical” side of the VSL. This information was used to create the time-resolved intermittency function  $I(t)$  at a location in space. Post-processing of  $I(t)$  implies that the scales characteristic of the VSL range from approximately  $0.3\theta$  to  $10\theta$ , where  $\theta$  is the momentum thickness of the shear layer. Velocity statistics conditioned upon the value of  $I(t)$  were also obtained. These conditional statistics strongly imply that unsheared fluid reaches the shear layer center from both the entrainment and primary streams. Similar conditioning was used to compare vortical and non-vortical autocorrelations and scales of motion near the high speed, irrotational flow domain. These observations reveal a significantly longer period of correlation in the non-vortical fluid.

Copyright by  
Aren Hellum  
2006

# TABLE OF CONTENTS

1.0	Introduction .....	1
1.1	Motivation.....	1
1.2	The Facility .....	1
1.3	Document Overview .....	3
2.0	Experimental Setup and Procedure .....	7
2.1	The Facility .....	7
2.1.1	Primary Flow .....	7
2.1.2	Entrainment Flow.....	8
2.2	Hot-wire Techniques and Processing.....	9
2.2.1	Apparatus .....	9
2.2.2	Calibration and Processing.....	11
2.2.3	X-array Probe.....	13
2.2.4	The transverse vorticity probe .....	14
3.0	Intermittency .....	29

3.1	Introduction .....	29
3.2	Defining “vortical”: surrogate methods .....	30
3.2.1	Townsend .....	30
3.2.2	Wynanski and Fiedler .....	32
3.2.3	Hedley and Keffer .....	32
3.2.4	Activity Intermittency .....	33
3.3	Defining vortical: detailed considerations.....	34
3.4	Comparison of Methods .....	37
4.0	VSL properties and conditional statistics .....	48
4.1	Properties of the VSL.....	48
4.1.1	Description of the VSL .....	48
4.1.2	Condition Duration .....	48
4.1.3	Appearance of the VSL.....	50
4.2	Conventional Statistics .....	51
4.3	Conditional Statistics .....	53
4.3.1	Description and Definition.....	53



4.3.2	Conditional Mean, Streamwise Component .....	54
4.3.3	Conditional Mean, Transverse Component .....	55
4.3.4	Conditional Standard Deviation, Streamwise and Transverse Velocity Components	56
4.3.5	Conditional Skewness, Streamwise Velocity Component.....	57
4.3.6	Reynolds Stress .....	59
4.4	Conditional Autocorrelation.....	60
4.5	Components of the Turbulence Kinetic Energy (TKE) Equation .....	62
4.5.1	Dissipation.....	63
4.5.2	Components of turbulent diffusion .....	64

# LIST OF FIGURES

## Figures, Chapter 1

Figure 1.1: General picture of a SSSL . . . . .	4
Figure 1.2: The MSU/TSFL Single Stream Shear Layer (SSSL) . . . . .	5
Figure 1.3: Self-similarity of mean velocity profile . . . . .	6

## Figures, Chapter 2

Figure 2.1: Side view of primary blower and flow treatment . . . . .	18
Figure 2.2: Contraction and leading edge of boundary layer . . . . .	19
Figure 2.3: (a): Boundary layer profile at separation lip. (b): Integrand of $\omega$ with the integrated smooth function superimposed. Note that the area under the curve at the 6 right-most locations (nominally free stream) is zero. . . . .	20
Figure 2.4: Schematic representation of a single wire hot-wire probe. . . . .	21
Figure 2.5: Schematic representation of a X Probe . . . . .	22
Figure 2.6: Transverse vorticity probe, side view (parallel wires come out of the page) . . . . .	23
Figure 2.7: Transverse vorticity probe, as seen by flow . . . . .	23
Figure 2.8: Transverse vorticity probe, 3D view . . . . .	24
Figure 2.9: Linear relationship of $\omega$ to $U$ with empirical constants . . . . .	24
Figure 2.10: Comparison of calibrations, quasi-steady method and “steady, point” method . . . . .	25
Figure 2.11: “Suction-side” calibration facility, with lid removed to reveal angle traverse and jet. . . . .	26
Figure 2.12: Assessment of speed and velocity from X-probe . . . . .	27

Figure 2.13: Measurement of separation between transverse velocity probe's parallel wires .....	27
Figure 2.14: The micro-circulation domain .....	28

### Figures, Chapter 3

Figure 3.1: Sample time series and sum of first and second derivatives computed for the Hedley and Keffer signal. Note that the ordinate on the second derivative's set of axes is a factor of 20 smaller than that of the first derivative's. ....	39
Figure 3.2: Sample vorticity time series with illustrative non-zero triggering thresholds. The transverse location from which these data were taken was $h = 2.46$ . Figures 3.3, 3.4, 3.5, 3.7, and 3.8 were also created using data from this location. ...	40
Figure 3.3: Average intermittency vs. vorticity threshold .....	41
Figure 3.4: Vorticity time series with trigger signal .....	42
Figure 3.5: Portion of vorticity time series illustrating the need for a "dwell" criteria. Location of the bottom axes is the boxed region on the upper axes. The "dots" on the bottom axes' curve represent individual data points. ....	43
Figure 3.6: Proposed structure of VSL .....	44
Figure 3.7: "Osculating" parabola of transverse velocity autocorrelationm illustrating the definition of the Taylor microscale. ....	45
Figure 3.8: Sensitivity of the technique to increasing dwell time. Each curve represents a different dwell time, measured as a multiple of . ....	46
Figure 3.9: Mean intermittency using the absolute magnitude of vorticity measure, the Wygnanski and Fiedler measure and the Hedley and Keffer measure, after the surrogate techniques have been "trained" to match the vortical measure. ....	46
Figure 3.10: Required threshold level, non-dimensionalized by $\sigma$ , needed to match the $\langle I \rangle$ measured by the vorticity method. ....	47

### Figures, Chapter 4

Figure 4.1: Illustration of a conceptual view of the VSL proposed by Phillips (1972)	64
--	----

**Figure 4.2:** Illustration of a nascent wedge increasing its positive curvature with respect to the non-vortical fluid. . . . . 65

**Figure 4.3:** Probability density distribution of conditional duration in time, non-dimensionalized by local Taylor microscale. The vertical lines in each distribution represent the mean value of each distribution. . . . . 66

**Figure 4.4:** Probability density distribution of conditional duration in time, non-dimensionalized by local Taylor microscale. The vertical lines in each distribution represent the mean value of each distribution. Note that the upper axes of this figure are the same as the lower axes of Figure 4.3. . . . . 67

**Figure 4.5:** Probability density distribution of conditional duration in time, non-dimensionalized by local Taylor microscale. The vertical lines in each distribution represent the mean value of each distribution. Note that the upper axes of this figure are the same as the lower axes of Figure 4.4. . . . . 68

**Figure 4.6:** Probability density distribution of conditional duration in time, non-dimensionalized by local Taylor microscale. The vertical lines in each distribution represent the mean value of each distribution. Note that the upper two axes of this figure are the same as the two lower axes of Figure 4.5. . . . . 69

**Figure 4.7:** Probability density distribution of conditional duration in length, non-dimensionalized by the momentum thickness (18.47 cm) at streamwise location . The vertical lines in each distribution represent the mean value of each distribution. . . 70

**Figure 4.8:** Probability density distribution of conditional duration in length, non-dimensionalized by the momentum thickness (18.47 cm) at streamwise location . The vertical lines in each distribution represent the mean value of each distribution. Note that the upper axes of this figure are the same as the lower axes of Figure 4.7. . . . . 71

**Figure 4.9:** Probability density distribution of conditional duration in length, non-dimensionalized by the momentum thickness (18.47 cm) at streamwise location . The vertical lines in each distribution represent the mean value of each distribution. Note that the upper axes of this figure are the same as the lower axes of Figure 4.8. . . . . 72

**Figure 4.10:** Probability density distribution of conditional duration in length, non-dimensionalized by the momentum thickness (18.47 cm) at streamwise location . The vertical lines in each distribution represent the mean value of each distribution. Note that the upper two axes of this figure are the same as the lower two axes of Figure 4.9. 73

**Figure 4.11:** Sample time series of streamwise component of velocity and intermittency. The measurement location is . . . . . 74

Figure 4.12: Illustration of the rake of probes used to measure the angle of the VSL relative to the transverse direction. The front angle is given by . . . . .	75
Figure 4.13: Timing scheme used in the algorithm to compute front angle. The pattern shown would be viewed as an “entering” edge. . . . .	76
Figure 4.14: Probability density distribution of VSL angle for both entering (vortical to non-vortical) and leaving (non-vortical to vortical) conditions. . . . .	77
Figure 4.15: Ratio of probabilities, $P(\text{entering})/P(\text{leaving})$ . . . . .	77
Figure 4.16: Mean value, streamwise component of velocity. Data from Morris (2002) are shown for comparison. . . . .	78
Figure 4.17: Standard deviation, streamwise component of velocity, Data from Morris (2002) are shown for comparison. . . . .	78
Figure 4.18: Standard deviation, transverse component of velocity. Data from Morris (2002) are shown for comparison. . . . .	79
Figure 4.19: Skewness, streamwise component of velocity. . . . .	79
Figure 4.20: Reynolds stress non-dimensionalized by square of free stream velocity. Data from Morris (2002) are shown for comparison. . . . .	80
Figure 4.21: Mean value, streamwise component of velocity. Vortical, non-vortical and unconditional values. (The mean value of intermittency is presented on the upper axis for reference.) . . . . .	80
Figure 4.22: Mean value, transverse component of velocity. Vortical, non-vortical and unconditional values. (The mean value of intermittency is presented on the upper axis for reference.) . . . . .	81
Figure 4.23: Standard deviation, streamwise component of velocity. Vortical, non-vortical and unconditional values. (The mean value of intermittency is presented on the upper axis for reference.) . . . . .	81
Figure 4.24: Standard deviation, transverse component of velocity. Vortical, non-vortical and unconditional values. (The mean value of intermittency is presented on the upper axis for reference.) . . . . .	82
Figure 4.25: Joint probability density distribution of fluctuating, non-vortical streamwise and transverse components of velocity at . Note that the solid black lines represent the unconditioned mean of streamwise and transverse velocity. . . . .	83

Figure 4.26: Skewness, streamwise component of velocity. Vortical, non-vortical and unconditional values. (The mean value of intermittency is presented on the upper axis for reference.) . . . . .	84
Figure 4.27: Probability density distributions of streamwise component of velocity, vortical condition, at three transverse locations . . . . .	85
Figure 4.28: Mean shear across the shear layer. The derivative was computed by fitting the streamwise velocity values with a piecewise polynomial spline, then differentiating that spline. . . . .	86
Figure 4.29: Reynolds stress divided by the product of standard deviations, also called the correlation coefficient ( $\rho$ ). Vortical, non-vortical and unconditional values. (The mean value of intermittency is presented on the upper axis for reference.) . . . . .	86
Figure 4.30: The Reynolds stress non-dimensionalized by the square of free-stream velocity ( $\rho^*$ ). Vortical, non-vortical and unconditional values. (The mean value of intermittency is presented on the upper axis for reference.) . . . . .	87
Figure 4.31: Model of non-vortical velocity fluctuations near the free stream--discredited by Figure 4.29's communication of distinctly non-zero correlation coefficient in non-vortical velocity near the free stream. In this model, negative streamwise fluctuations would have been equally associated with both positive and negative transverse fluctuations. . . . .	87
Figure 4.32: Conditional Autocorrelation of streamwise velocity component at seven positions on the high-speed side of the shear layer. . . . .	88
Figure 4.33: Dissipation, non-dimensionalized. Vortical, non-vortical, and unconditioned values. The equation defining the approximation of $\epsilon$ shown is Equation 4.13. . . . .	89
Figure 4.34: Unconditional dissipation, compared to values computed in Morris (2002). . . . .	90
Figure 4.35: Triple products of fluctuating velocity, non-dimensionalized by cube of free-stream velocity, unconditioned . . . . .	91
Figure 4.36: Triple products of fluctuating velocity, non-dimensionalized by cube of free-stream velocity, vortical . . . . .	92
Figure 4.37: Difference between vortical and unconditioned triple velocity products. . . . .	93
Figure 4.38: Triple products of fluctuating velocity, non-dimensionalized by cube of free-stream velocity, non-vortical. (Note that the ordinate has twice the range of Figs. 4.35 and 4.36.) . . . . .	94

# 1.0 Introduction

## 1.1 Motivation

An intermittent flow is one in which the motion at a given location is at times vortical and other times non-vortical. Intermittency is a characteristic of free turbulent shear flows and the turbulent boundary layer. A feature of intermittent flows termed the Viscous Super-Layer (VSL) is a central feature of the present discussion. This feature, the existence of which was first proposed by Corrsin (1943), is a thin interface between rotational and irrotational fluid. Since non-vortical fluid can only become vortical by the direct action of viscosity, the fluid on the “vortical” side of this interface represents fluid that is subject to viscous effects. Additional physical insight can be gained when statistics of these two vortical and non-vortical flow conditions are separately evaluated. These “conditional statistics” are the subject of Chapter 4.

## 1.2 The Facility

The subject flow is a high Reynolds number single-stream shear layer (SSSL) located in the Turbulent Shear Flows Laboratory at Michigan State University. This facility was created by and used in the thesis work of S.C. Morris (See Morris (2002)). A single stream shear layer, depicted in general form in Figure 1.1, is a flow in which a boundary layer has separated from its bounding wall. Following this separation, the sheared portion of the fluid entrains the unsheared fluid present in the free stream and the entrainment stream.

A schematic of the flow path and coordinate system of the SSSL used for the present work is depicted in Figure 1.2. This particular tunnel is well-suited to the investigation for several reasons. First, the large physical size of the tunnel allows hot-wire probes to

better approximate a point measurement. Second, since the vortical content of the flow is a variable of interest, it is important that the vorticity of the primary and the entrainment streams is very near zero. Two unique features of the facility were designed with this requirement in mind. The primary flow (marked with a “1” in Figure 1.2) at the separation lip has a very long (9.67 m) settling length following the final flow conditioning element. This is to ensure that the residual vorticity in the primary free stream is very small. The entrainment flow (marked with a “2” in Figure 1.2) is passed through flow treatment elements prior to entering the measurement region. These turbulence manipulators lower the level of vorticity in the entrainment stream. The pressure drop associated with these elements is recouped by driving the entrainment flow with four large fans upstream of the flow treatment. The details of this system are discussed in greater detail in Chapter 2.

Virtually all of the following discussion will be conducted in terms of non-dimensional quantities; hence, a discussion of these quantities is merited. Downstream of the separation lip ( $x = y = 0$ ), the turbulent boundary layer that has built up on the plate transitions into a free shear layer. The only flow scale that exists at this point is that of the boundary layer. The momentum thickness of this boundary layer,  $\theta_0$ , is the most natural scaling parameter for the streamwise axis. In the tunnel used in the present work,  $\theta_0$  was found to be 9.96 mm. The similarity variable which is used to scale the transverse axis is:

$$\eta(x, y) = \frac{y - y_{1/2}}{\theta(x)} \quad (1.1)$$



In equation 1.1,  $y_{1/2}$  is the transverse position at  $x$  where the streamwise component of velocity is half of that of the free stream value,  $\theta(x)$  is the momentum thickness of the shear layer at a given streamwise location  $x$ .

It has been shown in numerous prior studies, including Morris (2002), that this similarity variable can be used to collapse the data from different streamwise locations-- the domain for which this property holds is called the flow's self-preserving region. The present study verified this collapse. The results at several streamwise locations are shown in Figure 1.3.

### 1.3 Document Overview

Chapter 2 of this document presents the experimental apparatus and techniques used in the present study. Chapter 3 presents the process used to obtain the signal  $I(t)$ , where

$$I(t) \Big|_{\hat{x} = \text{constant}} = \begin{cases} 1, & \text{if fluid at } \hat{x} \text{ at time } t \text{ is vortical} \\ 0, & \text{if fluid at } \hat{x} \text{ at time } t \text{ is non-vortical} \end{cases} \quad (1.2)$$

Chapter 4 presents "conditional statistics" of the flow and measurements of the motions and appearance of the VSL.

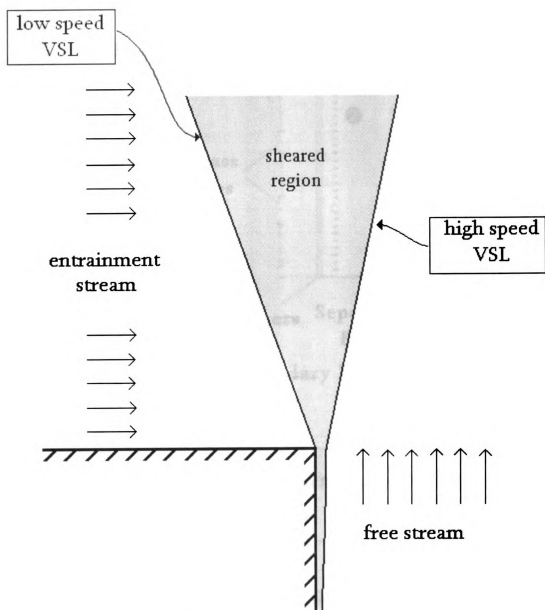


FIGURE 1.1 General picture of a SSL

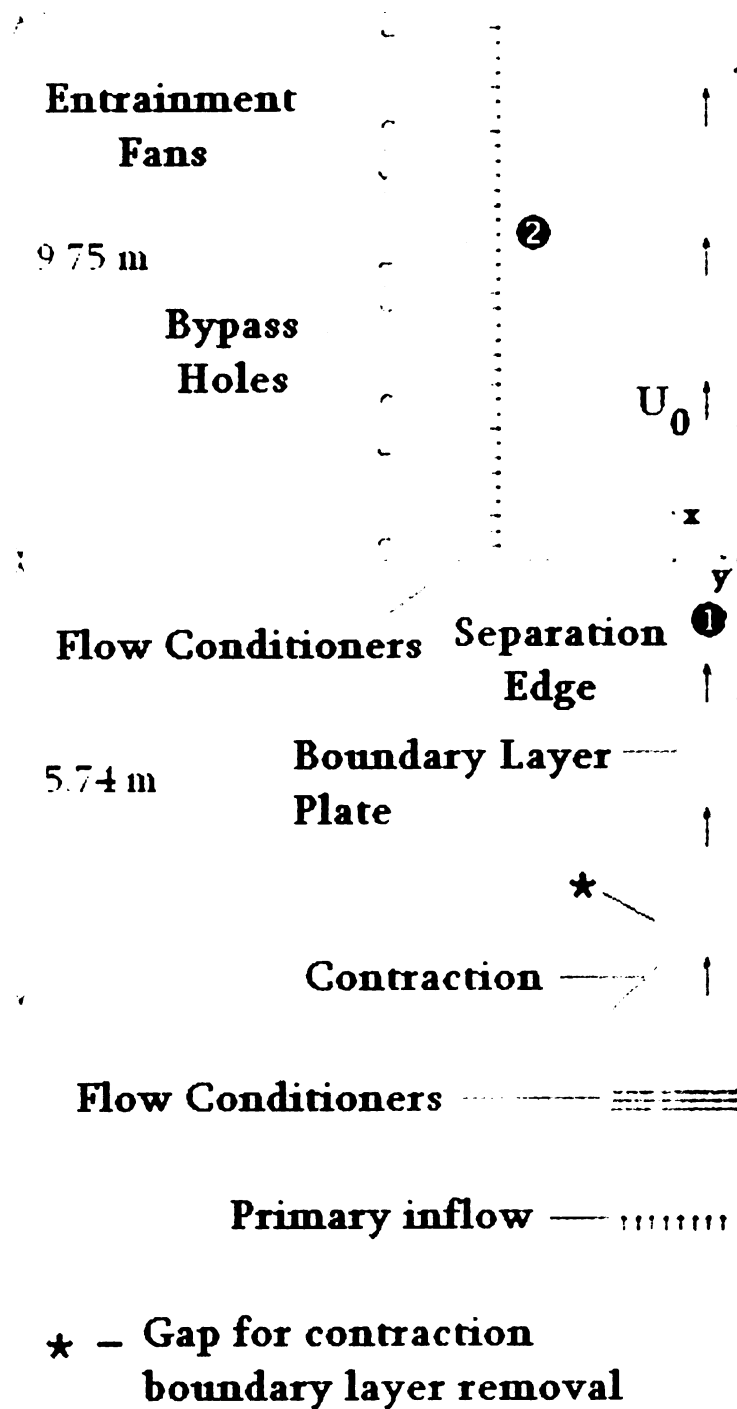
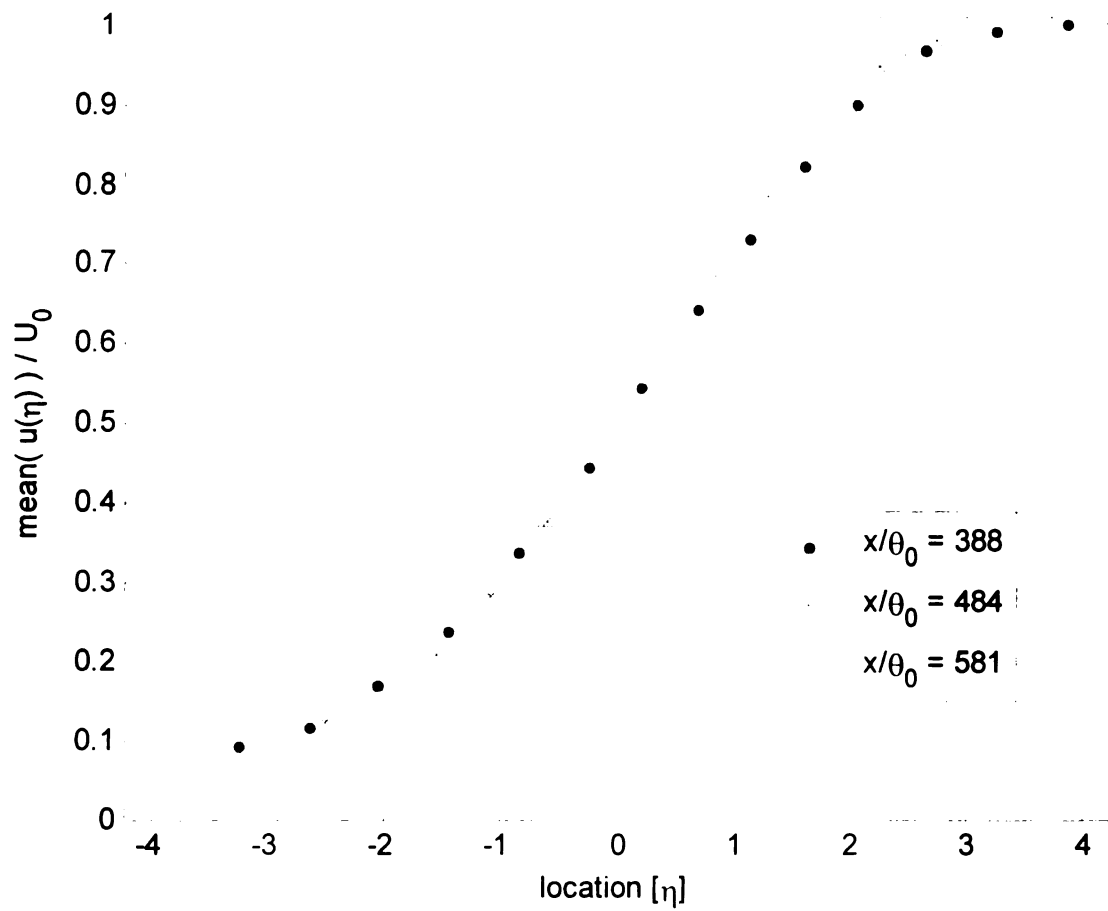


FIGURE 1.2 The MSU/TSFL Single Stream Shear Layer (SSSL)



**FIGURE 1.3 Self-similarity of mean velocity profile**

## 2.0 Experimental Setup and Procedure

### 2.1 The Facility

#### 2.1.1 Primary Flow

The primary flow is propelled by an axial fan at ground level. After leaving the fan, the fluid goes through two sets of turning vanes, each turning the flow 90 degrees so that the exit flow is brought to the level of the main tunnel, 2.1 m above the ground. This is depicted in Figure 2.1. Directly ahead of the lower set of turning vanes are furnace filters, used to smooth out variations in the velocity profile. After the flow exits the second set of turning vanes, it is delivered through a 2 meter by 2 meter opening covered by “honeycomb” flow treatment and three fine (mesh size = 0.76 mm, open area = 80%) steel screens separated by 10.2 cm. The honeycomb, which is used to break up large vortical motions, consists of cut soda straws ( $L/D = 8$ ,  $L = 2.54$  cm) pressed and glued together. The screens serve to even out variations in the velocity profile and further reduce the characteristic size of turbulent motions in their wakes.

After passing through the screens, the fluid passes through the portion of the tunnel depicted in Figure 2.2. The flow goes through a nominal 2:1 contraction. The leading edge of the boundary layer plate is offset from the end of this contraction by 2.5 cm and fitted with an elliptical edge. This offset serves to remove the boundary layer that has built up during the contraction. A boundary layer trip has been installed 30 cm downstream of the boundary layer leading edge. Its purpose is to ensure that the location of transition to turbulence is fixed in space. The resulting turbulent boundary layer is then allowed to develop over a length of 5.4 meters from this trip. The Reynolds number of the boundary layer at separation is  $Re(\theta_0) \approx 4500$ . This is quite a

large value for a laboratory single stream shear layer. The long (9.7 m) distance downstream from the final set of primary flow conditioners ensures that negligible vortical motions remain in the potential stream.

The momentum thickness of the turbulent boundary layer at the separation lip is used to scale the streamwise axis. This momentum thickness has been measured and was found to be 9.96 mm. The profile of the boundary layer at separation is shown in Figure 2.3 (a). The integrand of the expression

$$\theta_0 = \int_0^{\infty} \frac{u(y)}{U_0} \left(1 - \frac{u(y)}{U_0}\right) dy \quad (2.1)$$

is shown in Figure 2.3 (b). The smooth curve superimposed over the data in Figure 2.3 (b) is an interpolated piecewise cubic spline. The area under this curve was integrated, yielding the above value of 9.96 mm for  $\theta_0$ .

### 2.1.2 Entrainment Flow

The location  $x = y = 0$  is termed the separation edge. Downstream of this point, the wall along which the boundary layer has developed no longer exists, and the boundary layer transitions into a single stream shear layer. As this shear layer develops it will widen, entraining fluid from both the high speed primary flow ( $y > 0$ ) and from the low speed region ( $y < 0$ ). A typical SSSL facility allows this low-speed (entrainment) flow to be induced directly from the laboratory environment, without benefit of flow conditioning.

The MSU-TSFL facility is distinctive in that it introduces turbulence manipulators between the laboratory environment and the flow of interest. Specifically, “honeycomb” ( $L/D = 8$ ,  $L = 2.54$  cm) followed by three mesh (mesh size = 0.76 mm, open area = 80%) screens separated by 10.2 cm are employed to deliver a low disturbance entrainment flow. This flow treatment has the additional effect of imposing a pressure drop on the entrainment flow. This pressure drop must be balanced by a momentum-introducing element if the required zero pressure gradient in the streamwise direction is to be preserved.

Four large (48” diameter) axial fans, driven by 3-phase AC motors, were used to provide this momentum. The entrainment velocity provided by these fans must be adjusted such that the pressure gradient in the primary stream is equal to zero. If the entrainment velocity is too high, the shear layer will be “overfed”, causing a negative pressure gradient in the free stream. If the entrainment velocity is too low, the shear layer will be “starved”, causing a positive pressure gradient in the free stream. To ensure a zero pressure gradient condition, a Durapulse AC motor controller was used to modulate the frequency of the line voltage driving the motors. This allowed the fans’ rotational speed to be tuned to provide the required pressure-rise condition. The zero pressure gradient condition was ensured by measuring the free stream speed with a hot-wire at the exit plane ( $x = 0$ ) and at a large distance ( $x/\theta_0 = 400$ ) downstream. The fan speed was then adjusted until the two values were equal.

## 2.2 Hot-wire Techniques and Processing

### 2.2.1 Apparatus

Hot-wire anemometry has long been a standard tool of turbulence research. A good overview of the technique is found in Bruun (1995). An overview of the techniques and devices germane to the present document follows.

The anemometer used to collect the data presented in this document was a DISA 55M Constant Temperature anemometer. This proven device uses a Wheatstone bridge and compensating electronics to attempt to continuously maintain a constant temperature at the sensor. The sensor forms one leg of the bridge, and the voltage required to maintain the desired overheat ratio is monitored and sampled at discrete times.

The basic sensor is depicted in Figure 2.4. It consists of a 5 micrometer diameter tungsten filament electroplated with copper on the ends to a diameter of 50 micrometers. The unplated portion is commonly referred to as the wire's "active region" and it is approximately 1 mm in length. The copper is soldered to stainless steel jeweler broaches fixed to the main body of the probe. The copper serves two purposes. First, it allows the probe fabricator to solder, rather than weld, the wire to the broaches. Second, and more importantly, it decreases the aerodynamic effect of the broaches on the sensor. To clarify: the increased diameter in the plated region, as well as the choice of copper, serves to greatly reduce the electrical resistance in the plated region, reducing the temperature in this region. Since broach effects (boundary layer and wake) will be confined to the area nearest the broach, a lower temperature near the broach reduces the impact of these aerodynamic effects. This consideration is of particular importance when the probe is a multi-wire probe.



A X-wire probe is depicted in Figure 2.5. It consists of two wires, as described above, mounted at approximately right angles to each other. A hot-wire sensor is sensitive to both the velocity and angle of the fluid cooling it. A single-sensor probe cannot recover both of these quantities, whereas a two-sensor probe constructed as shown is able to do so. The procedure to accomplish this will be discussed in Section 2.2.3.

The transverse vorticity probe, or Mitchell probe, is depicted in various views in Figures 2.6, 2.7, and 2.8. It consists of two parallel straight wires at a known distance<sup>1</sup> apart whose long axes are at a right angle to the plane of an X array. The four cooling velocities measured can then be processed such that a measurement of transverse vorticity is obtained. This processing procedure will be discussed in Section 2.2.4.

## 2.2.2 Calibration and Processing

The transfer function used to compute a cooling velocity from the measured voltage is a modified version of what is known as King's law:

$$E^2 = A + BQ^n \quad (2.2)$$

where E is the measured voltage across the wire, Q is the cooling velocity and A, B and n are empirically determined constants. In order to determine this relationship, the wire must be calibrated. That is, the response of the wire must be known at certain known velocities.

The basic method of calibrating a sensor involves placing the wire in a steady, inviscid, incompressible flow. This flow is therefore amenable to velocity measurement via a

---

1. It is important that the measurement of this distance be very accurate. To ensure this, a procedure which will be detailed in Section 2.2.4 is employed.

pressure measurement and the Bernoulli principle. The hot-wire voltage and pressure data are obtained, then the flow is adjusted, and voltage and pressure information are measured at this new speed. This process is then repeated until the range of velocities expected in the flow of interest have been covered with sufficient density to be confident in the obtained fit. An example of the curve to be fitted along with its accompanying constants is depicted in Figure 2.9.

This procedure can be altered slightly to save calibration time. Rather than use a truly steady flow, the flow can be continuously varied over the range of velocities. It is worth noting that this does violate one of the assumptions of the Bernoulli principle; however, if the rate of change of velocity is sufficiently small, the error introduced by this effect is similarly small. In Figure 2.10, the calibrations obtained by the same wire by both the “steady, point” method and the “quasi-steady” method are shown. The continuous curve in this figure represents the transfer function found by the quasi-steady method over the range of  $E^2$ . The discrete points represent the mean values of  $E^2$  found during the “steady, point” calibration which have been put through the transfer function found by the “steady, point” method. It is clear that the error introduced by the quasi-steady effect is negligibly small.

During either of the two above procedures, the local temperature near the wire is monitored throughout. This measurement is made for two reasons. First, the local density must be known in order to establish local velocity by the Bernoulli relationship. Second, a hot-wire is not able to measure simply a cooling velocity—it measures its local cooling environment. The effect of ambient temperature change was examined in

Abdel-Rahman et al (1987). The changes in ambient temperature between calibration and data acquisition have been found to be small in the facilities used in the present discussion; as such, a linear correction as described in Abdel-Rahman [1] was employed.

### 2.2.3 X-array Probe

This procedure is fundamentally unchanged for an X-array probe, with the additional consideration that the probe must now be placed at various angles<sup>2</sup> to assess the effects of flow angle on the response of each wire. The calibration facility shown in Figure 2.11 was constructed to accomplish this. The facility is a “suction-side” unit—that is, a jet is created by allowing a nozzle flow to exhaust into a sub-atmospheric plenum that is evacuated by a centrifugal blower. The wire is placed at the exit of this jet, along with the supporting pressure and temperature measurements. The primary advantage of a “suction-side” box (compared to a “pressure-side” unit, in which the nozzle exhausts to atmospheric pressure) is a lower disturbance exit velocity. Elimination of fluctuations in the jet velocity is important, because these fluctuations directly affect the uncertainty associated with the technique. It is this consideration which justifies the increased effort involved in the fabrication and operation of a suction-side unit.

A stepper motor has been mounted to the probe-holding fixture to allow adjustment of the probe angle inside the plenum. A potentiometer has been affixed to this angular

---

2. It is this need to determine wire response at many angles which motivates the use of the quasi-steady calibration. Obtaining enough discrete data points to accurately assess wire response in two dimensions (orientation angle and velocity) requires nominally an hour for a single probe. In contrast, the quasi-steady procedure accomplishes this same task in about 15 minutes.

traverse to provide a resistance which changes proportionally to the change in angle. This potentiometer forms one side of a voltage divider circuit. The voltage across the other side of the circuit was then measured. This voltage relates the angular position of the probe.

The calibration procedure as it relates to X-array probes is therefore as follows: position the probe at a known angle to the oncoming flow. Vary the oncoming flow velocity slowly per the quasi-steady procedure described above. Reposition the probe at a new known angle and repeat the process, until a satisfactory number and range of angles have been obtained. For the present work, 13 angles in 6 degree increments from -36 degrees to 36 degrees were deemed satisfactory.

The result of this procedure is a set of 13 transfer functions in the form of Equation 2.2 for each wire--one function for each calibration angle. Given a voltage for each wire, the velocity for each wire that would result from that voltage, at that angle, is computed. Since the angles at which these possible velocities exist is also known, we can view this calibration information as two sets of speed/angle pairs. These sets of pairs are can be viewed on a Cartesian coordinate system, depicted in Figure 2.12. Since each wire is (assumed to be) at the same angle to the flow and the fluid passing over each is at the same velocity, the intersection of these curves determines the speed and angle of the flow experienced by the probe<sup>3</sup>.

#### 2.2.4 The transverse vorticity probe

---

3. This processing method is very similar to one introduced by Browne et al. (1989). The method as described above was independently developed by Morris (2002).

A time-resolved measurement of transverse vorticity<sup>4</sup> is also desired. The basic method for accomplishing this with the probe depicted in Figures 2.6, 2.7, and 2.8 was originally communicated in Wallace and Foss (1995), but will be repeated here with mention made of subsequent additions to and refinements of the method.

This four-wire probe can be considered to be comprised of two arrays: an X-array, identical to that described in Section 2.2.3, and an array of parallel wires. The procedure for calibrating the probe is similar to that of an X-array--the probe is placed at various angles to assess the effects of flow angle on the response of each wire. Some previous iterations of this method did not take into account the effects of varying flow angle on the array of parallel wires. These effects were accounted for in the present work.

The vorticity measurement is made by approximating the relevant terms of the curl of velocity. The following discussion concerns the spanwise component of vorticity. This component of vorticity is best able to define the average behavior of the vorticity filaments comprising the VSL. Since the mean flow field is homogenous in the spanwise direction, and nearly homogenous in the streamwise direction, the only component of vorticity having a non-zero mean value is the spanwise component. Note that the other components may have distinctly non-zero fluctuations.

To approximate the spanwise component of vorticity, the terms which must be approximated are the derivative of the streamwise component in the transverse direc-

---

4. The measurement procedure and supporting algorithms detailed describe a procedure which is time-resolved and *approximates* a point measurement. Since the circulation is calculated about a finite volume, all derivatives are approximations of their infinitesimal form.

tion and the derivative of the transverse component in the streamwise direction. Or, following the common nomenclature,

$$\omega_z = \frac{\partial v}{\partial s} - \frac{\partial u_s}{\partial y} \quad (2.3)$$

The above derivatives are not directly approximated. Instead, a construct known as the “micro-circulation domain”, shown in Figure 2.14, is employed, along with Green’s Theorem (Equation 2.4) in the approximation of vorticity.

$$\iint \bar{\omega} dA = \Gamma = \oint \vec{V} d\vec{s} \quad (2.4)$$

Equation 2.4 states that the average vorticity through the area IJKL (see Figure 2.14) is equal to the circulation around the perimeter  $\overline{IJKL}$ . The average vorticity through the area IJKL is therefore:

$$\omega_z = \frac{\Gamma}{(ds)(dy)} = \frac{v(N) - v(M)}{ds} + \frac{\overline{u_s(\vec{JK})} - \overline{u_s(\vec{IL})}}{dy} \quad (2.5)$$

The length  $dy = |\vec{IJ}| = |\vec{LK}|$  is the separation between the probe’s two parallel wires, as shown in Figure 2.6. Measurement of the distance between the parallel wires is performed by traversing a calibrated probe across a steep velocity gradient. A boundary layer or a thin free shear layer is appropriate for this task. The velocity is recorded at a series of known locations, and this information is plotted for each wire on a set of axes, shown in Figure 2.13. The distance between these two curves is the separation between the parallel wires.

The length  $ds$  is calculated iteratively:

$$ds(m) = \frac{1}{2m+1} \sum_{i=n-m}^{n+m} \cos(\gamma(t_i) - \langle \gamma_n \rangle) \times \frac{q1(t_i) + q2(t_i)}{2} \times \Delta t \quad (2.6)$$

Where  $\langle \gamma_n \rangle$ , the mean angle over a domain of size  $m$  about point  $n$ , is given by:

$$\langle \gamma_n \rangle(m) = \frac{1}{2m+1} \sum_{i=n-m}^{n+m} \gamma(t_i) \quad (2.7)$$

$\Delta t$  is the amount of time between acquired realizations.  $q1$  and  $q2$  are the velocity magnitudes at each time step. The value of  $m$  is increased until  $ds > dy$ .

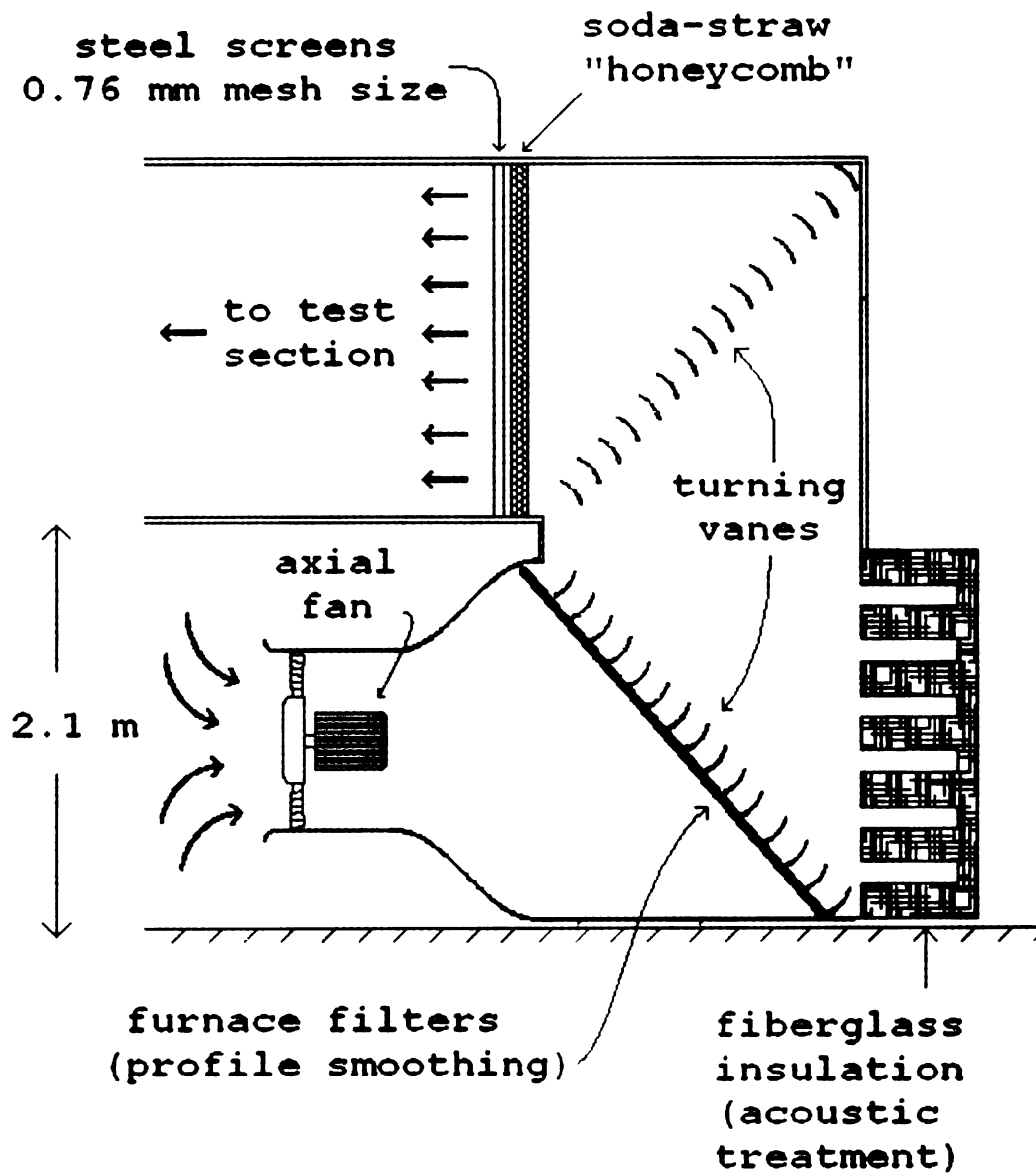


FIGURE 2.1 Side view of primary blower and flow treatment



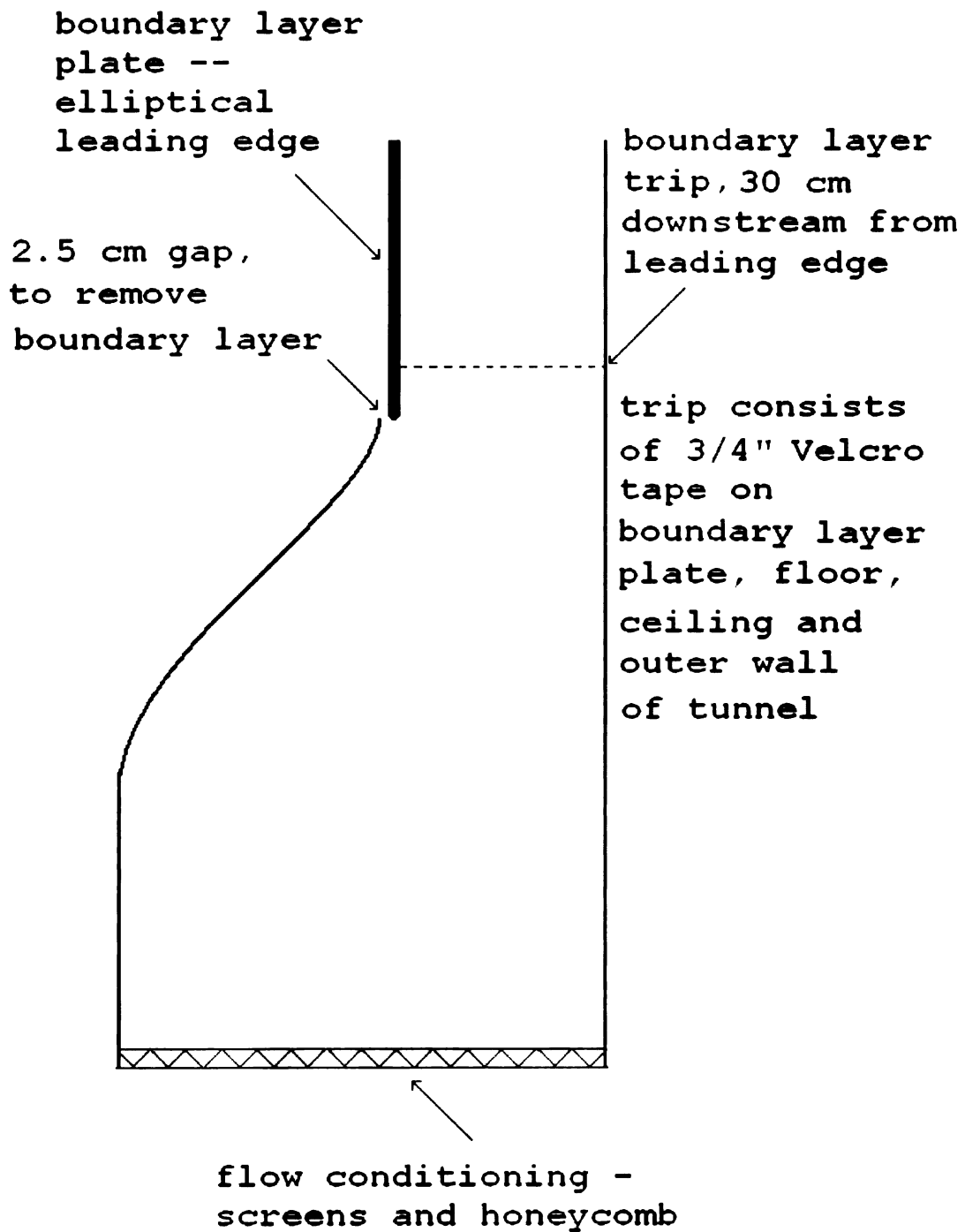
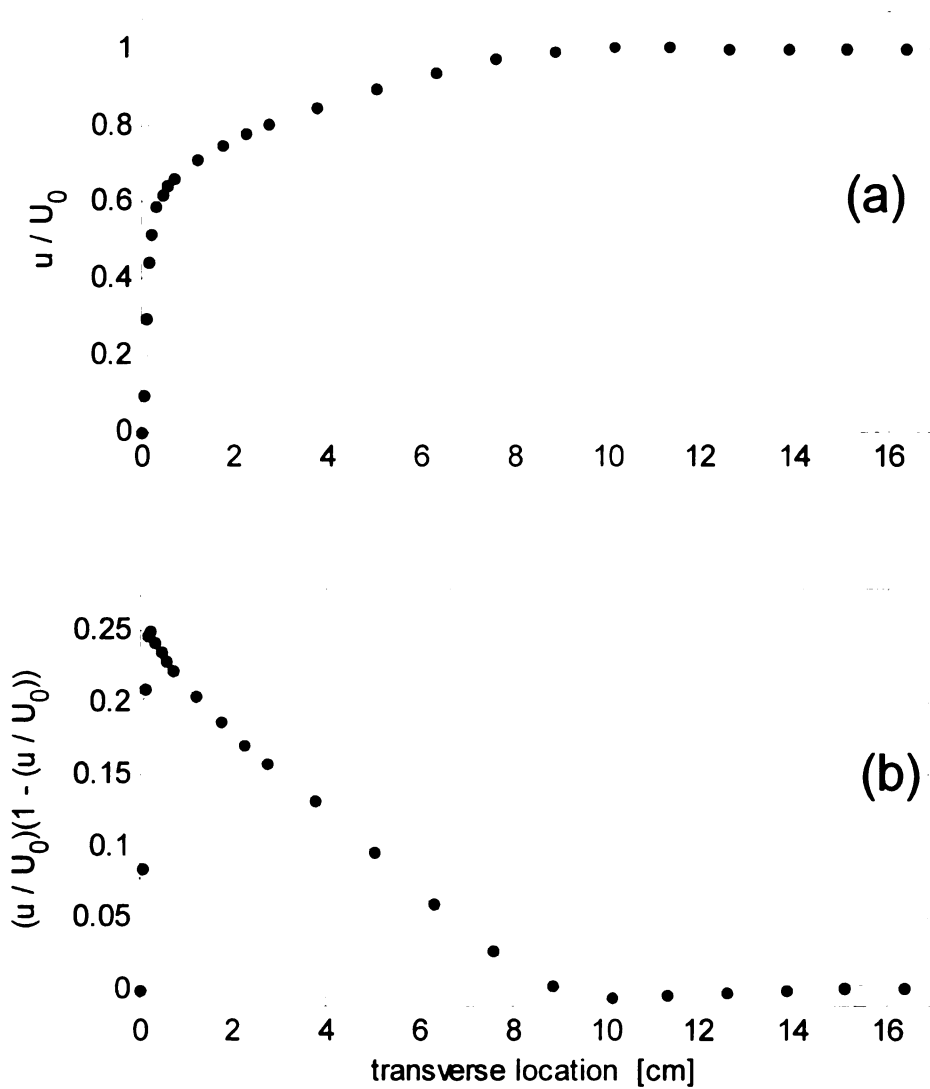
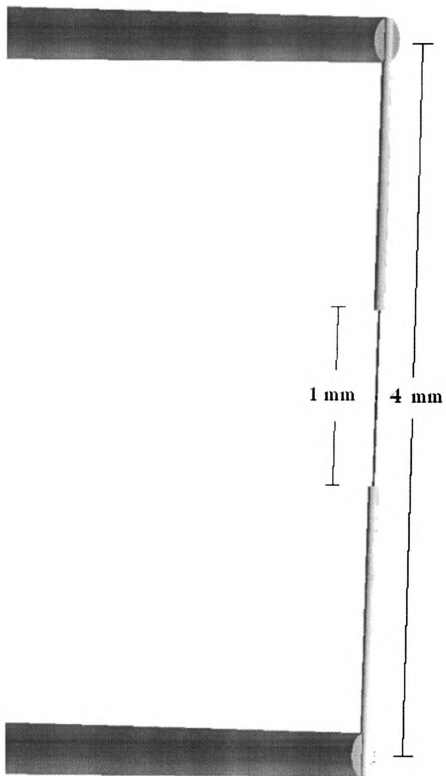


FIGURE 2.2 Contraction and leading edge of boundary layer



**FIGURE 2.3 (a): Boundary layer profile at separation lip. (b): Integrand of**

**$\int_0^{\infty} \frac{u(y)}{U_0} \left(1 - \frac{u(y)}{U_0}\right) dy$  with the integrated smooth function superimposed. Note that the area under the curve at the 6 rightmost locations (nominally free stream) is zero.**



**FIGURE 2.4** Schematic representation of a single wire hot-wire probe

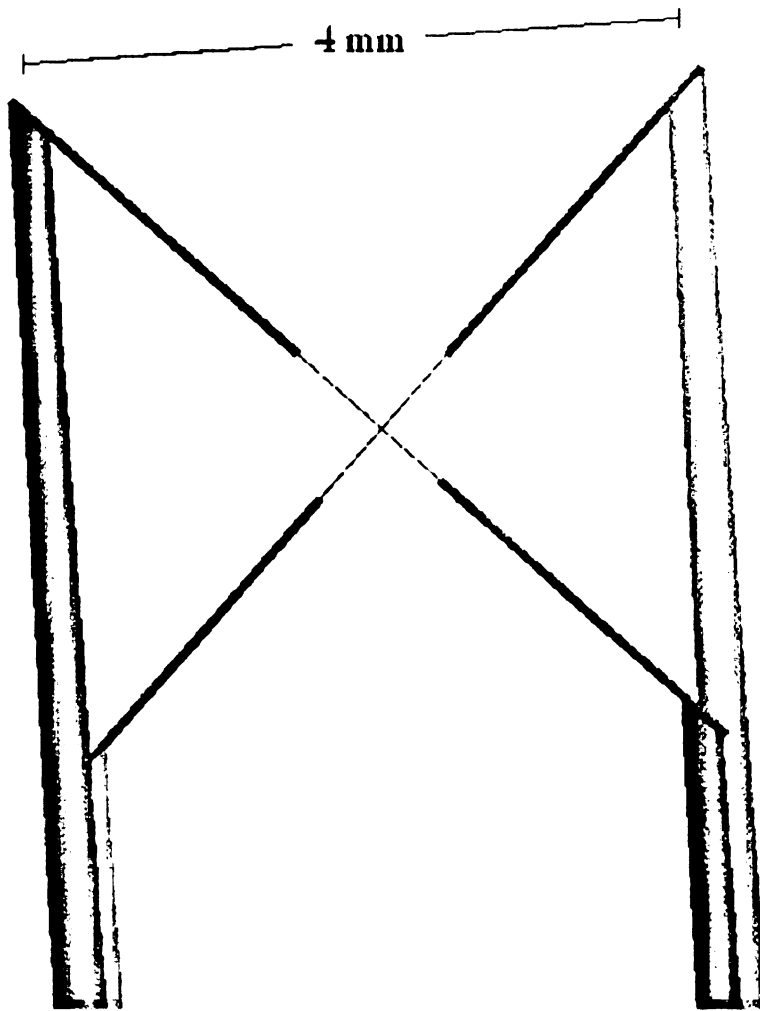


**FIGURE 2.5 Schematic representation of a X Probe**

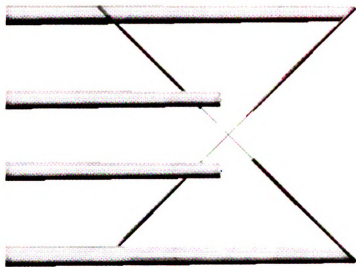


**FIGURE 2.6** Transverse vorticity probe, side view (parallel wires come out of the page)

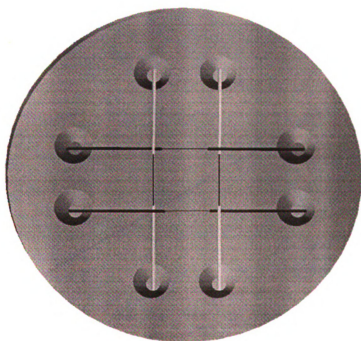


**FIGURE 2.7** Transverse vorticity probe, as seen by flow

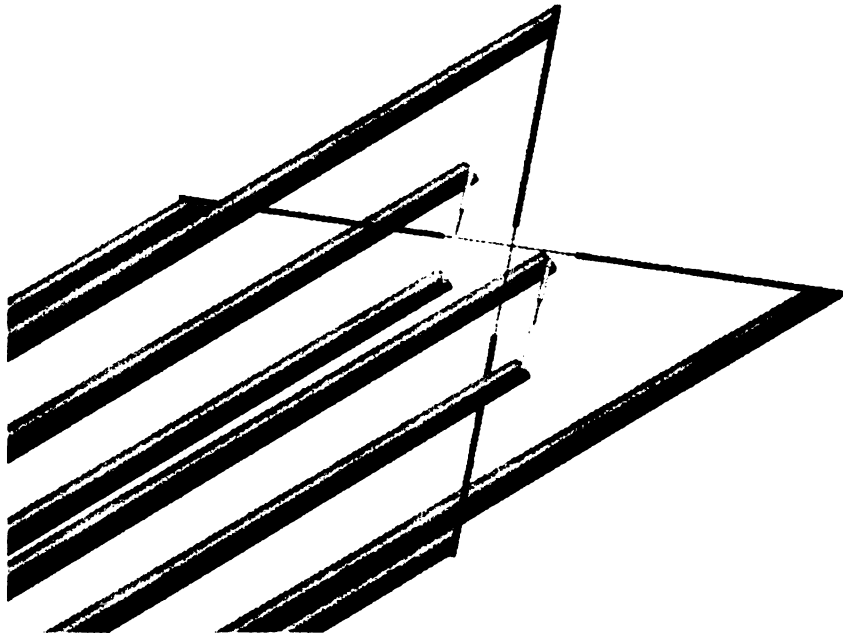


**FIGURE 2.8 Transverse vorticity probe, 3D view**

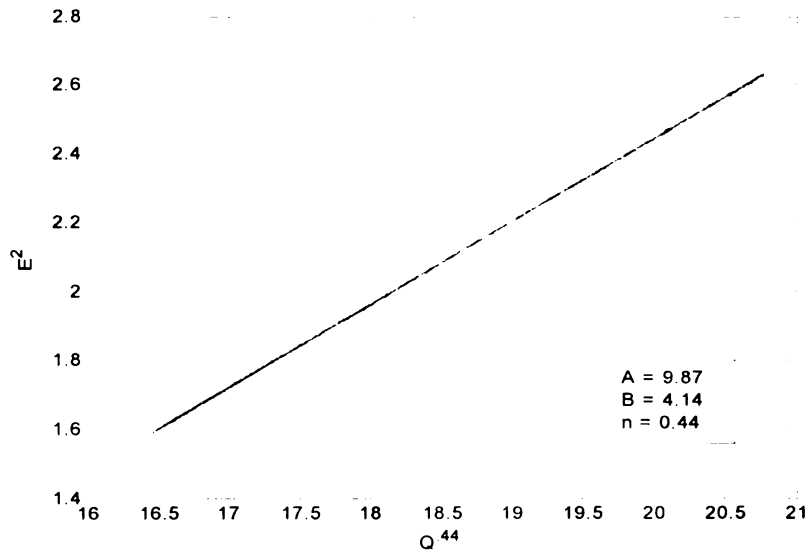


**FIGURE 2.9 Linear relationship of  $E^2$  to  $Q^n$  with empirical constants**

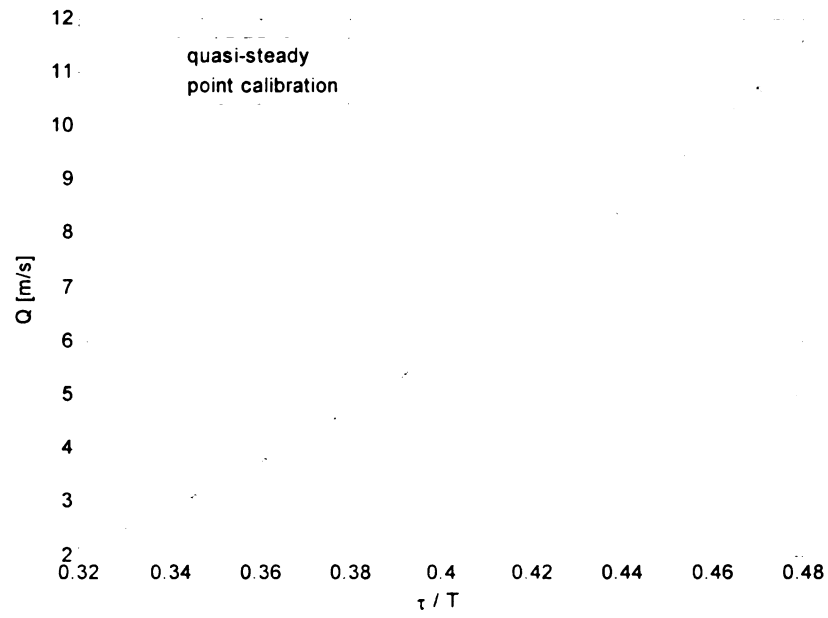


**FIGURE 2.10 Comparison of calibrations, quasi-steady method and “steady, point” method**

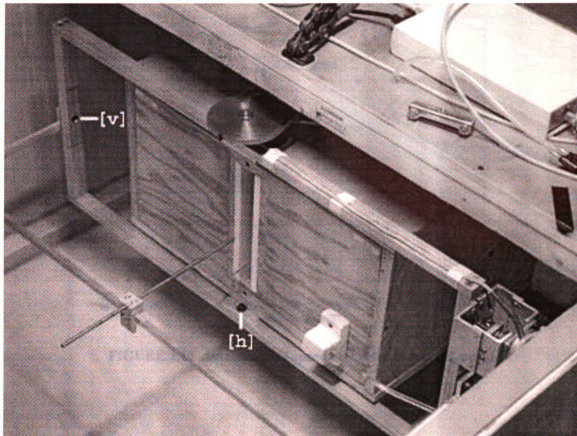


**FIGURE 2.11** “Suction-side” calibration facility, with lid removed to reveal angle traverse and jet.

Note: this traverse is capable of rotating the measurement region of the probe about both the horizontal and vertical axes, marked on the above figure with [h] and [v] respectively.



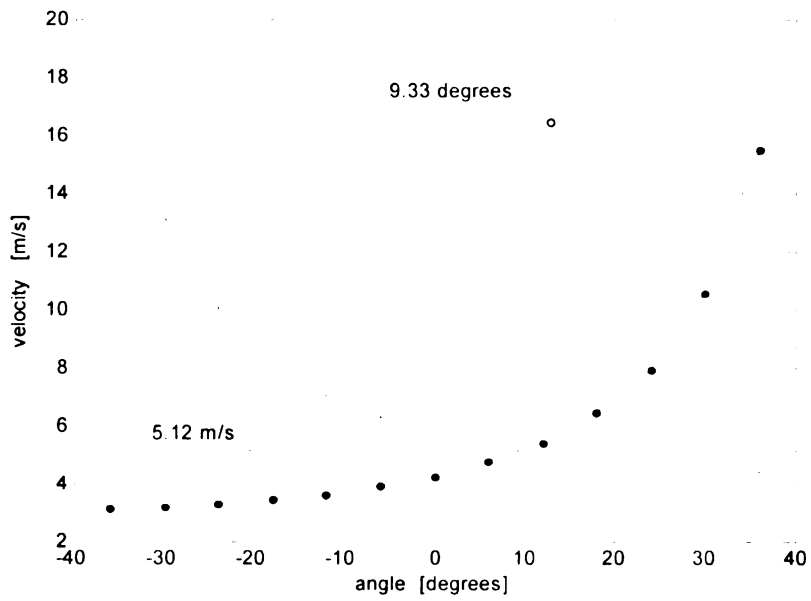


**FIGURE 2.12 Assessment of speed and velocity from X-probe**

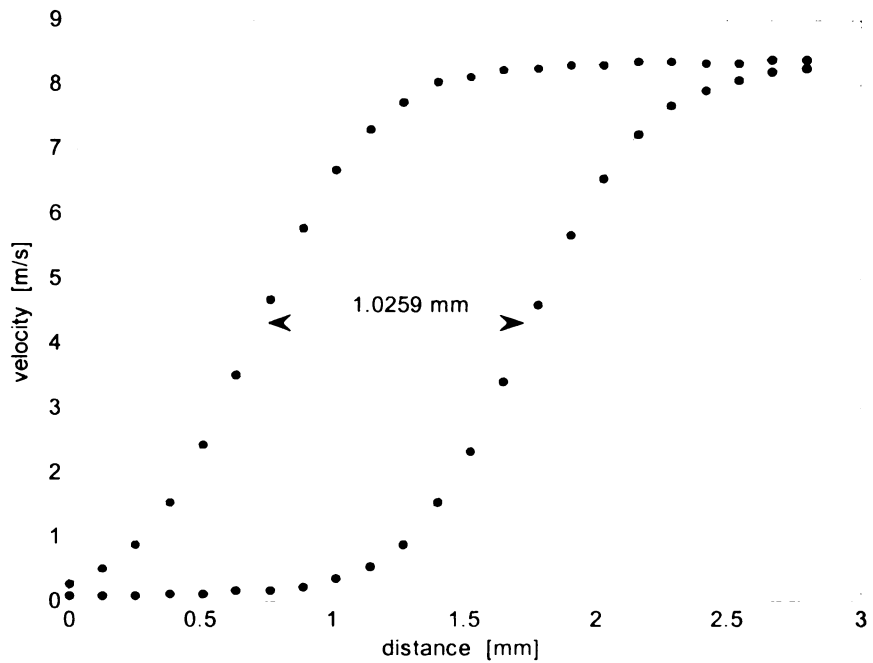
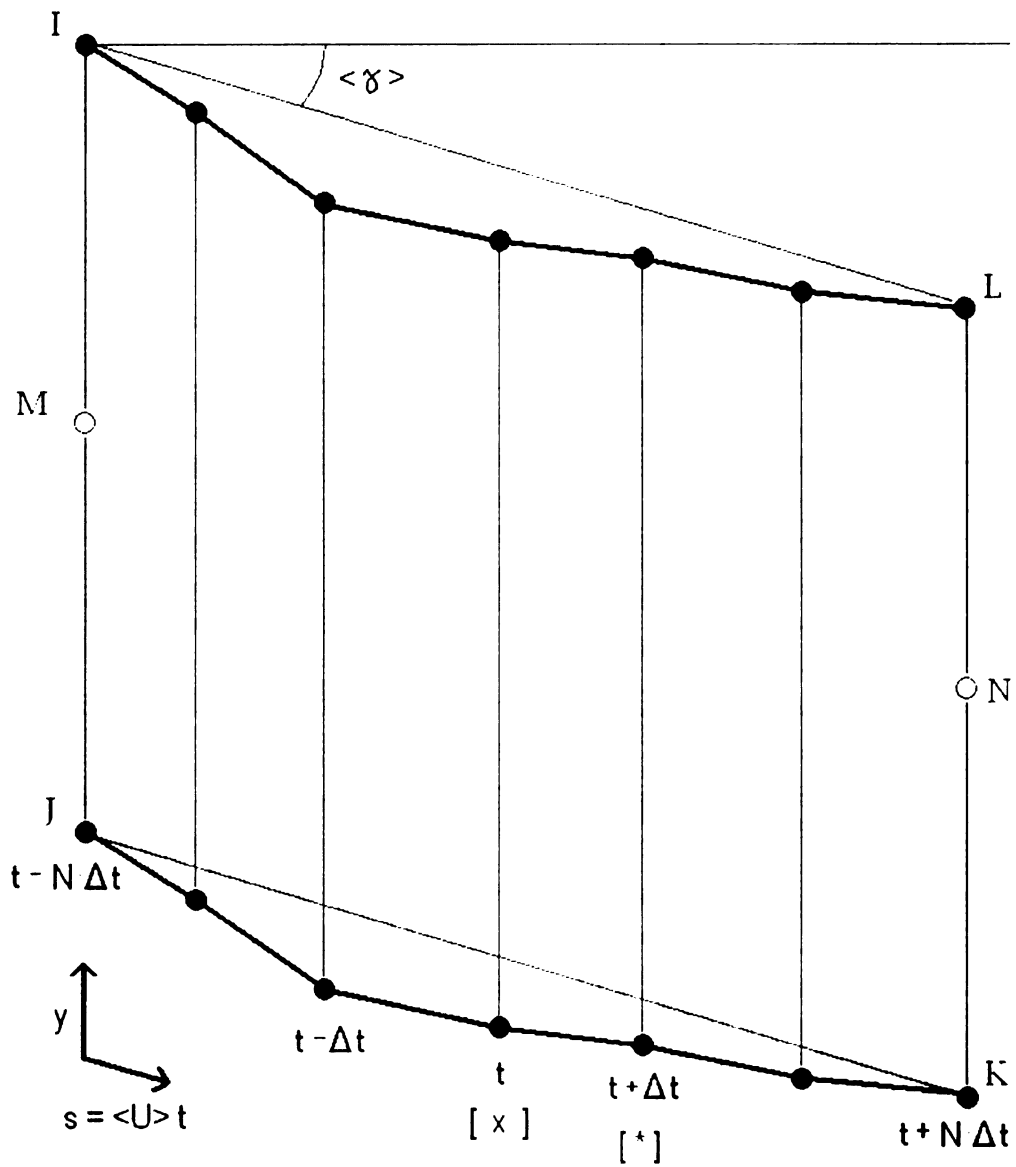


**FIGURE 2.13 Measurement of separation between transverse velocity probe's parallel wires**



$$* = x - (\Delta t)u(t + \Delta t)\cos(\gamma(t + \Delta t) - \langle \gamma \rangle)$$

FIGURE 2.14 The micro-circulation domain

## 3.0 Intermittency

### 3.1 Introduction

The curl of the Navier Stokes equation,

$$\frac{D\omega}{Dt} = (\vec{\omega} \bullet \nabla) \vec{V} + \nu \nabla^2 \vec{\omega} \quad (3.1)$$

is known as the vorticity transport equation. Flows which are bounded by fluid possessing negligible vorticity, that is,  $\omega \approx 0$ , often exhibit “intermittent” properties. Within the field of interest, there exist locations at which the fluid could at times be described as vortical, and at other times, non-vortical. The boundary between vortical and non-vortical fluid is known as the Viscous Superlayer (VSL).

It can be argued that the VSL is a sharp boundary by analysis of Equation 3.1. The term

$\frac{D\omega}{Dt}$  represents the time rate of change of vorticity for a fluid element. A non-vortical

fluid element can only become vortical via the direct action of viscosity, hence the

term  $\nu \nabla^2 \vec{\omega}$  must be of the same order of magnitude as  $\frac{D\omega}{Dt}$ . Note that  $\nabla^2$  has units of

$1/(\text{length})^2$ , where (length) characterizes the thickness of the VSL. Since  $\nu$  is

“small”,  $1/(\text{length})^2$  must be “large”, and therefore (length) is “small”.

The result of this procedure is a function  $I(\vec{x}, t)$  such that:

$$I(t) \Big|_{\vec{x} = \text{constant}} = \begin{cases} 1, & \text{if fluid at } \vec{x} \text{ at time } t \text{ is vortical} \\ 0, & \text{if fluid at } \vec{x} \text{ at time } t \text{ is non-vortical} \end{cases} \quad (3.2)$$

The time-mean of this function,  $\langle I \rangle$ , therefore represents the fraction of time that the fluid passing a point in space is vortical. Both the time record and the time-mean of  $I(\vec{x}, t)$  have application in characterizing the flow.

Those sections of flow deemed vortical can be separated from the rest of the record and quantities representative of only the vortical portions determined. These conditional statistics are the primary focus of Chapter 4. The number and frequency of transitions between vortical and non-vortical at a given point gives some measure of the structure of the VSL.

### 3.2 Defining “vortical”: surrogate methods

Previous works have discussed the topic of intermittency. These works made use of a different signal than vorticity to construct the function  $I(t)$ . These surrogate methods construct  $I(t)$  such that  $I(t) = 1$  if  $\frac{\partial}{\partial t} \text{velocity}$  is sufficiently large, and  $I(t) = 0$  otherwise. For reasons stated in the previous section, the author believes the current method of constructing  $I(t)$  to be the most closely tied to the physics of the flow. However, the surrogates are appropriate indicators of dissipation and turbulent mixing. They are therefore not without technical importance. Details of and comparisons between the various methods follows.

#### 3.2.1 Townsend

One of the earliest works on the topic of intermittency was Townsend (1956), who used even powers of the spatial derivative of velocity and compares it to the analogous

even powers of a known “fully turbulent” flow to obtain the average value of intermittency at some location.<sup>1</sup> That is,

$$\langle I \rangle = \frac{\left[ \overline{\left( \frac{du}{dx} \right)^4} \right]}{\left[ \overline{\left( \frac{du}{dx} \right)^2} \right]^2} \bigg/ \frac{\left[ \overline{\left( \frac{du}{dx} \right)^4} \right]}{\left[ \overline{\left( \frac{du}{dx} \right)^2} \right]^2} \quad (3.3)$$

The single bar notation,  $\overline{(\dots)}$ , refers to the ordinary time mean, and the double bar notation,  $\overline{\overline{(\dots)}}$ , refers to the mean taken only during the turbulent portion of the flow.

The claim is made in Townsend (1956y) that the flow being examined (planar wake behind a cylinder) was always turbulent near its centerline, The “turbulent mean” derivative is therefore computed at this location. Note that this method assumes

implicitly that  $\overline{\overline{\left( \frac{\partial u}{\partial x} \right)^2}}$  is the same in the turbulent flow regardless of distance from the mean position of the VSL. This will be further discussed in Section 4.5.1.

It is notable that this method is only able to estimate the mean value of intermittency over some given period of time. Townsend (1956), also proposes a measure able to recover  $I(t)$ :

$$signal = \left( \frac{\partial u}{\partial x} \right)^2 \quad (3.4)$$

---

1. It should be noted that in the 1976 edition of the Monograph, Townsend does not make mention of the measures listed. It is not known whether this omission represents a retraction.

If this signal passes some determined threshold at some time  $t$ , the flow is considered to be turbulent. It is assumed that the unmodified “frozen-flow hypothesis” was used to convert between the time derivative of velocity and the spatial derivative required.

This signal is physically interesting in that it is proportional to the dissipation in a homogenous, isotropic turbulent flow<sup>2</sup>. Implicit in the use of this signal as an indicator of turbulence is that dissipation in turbulent fluid is larger than in non-turbulent fluid, which is a reasonable claim.

### 3.2.2 Wygnanski and Fiedler

Another measure was presented in Wygnanski and Fiedler (1970). The identifier used in this work was the sum of squares of two time derivatives of velocity:

$$signal = \left( \frac{\partial^2 u}{\partial t^2} \right)^2 + \left( \frac{\partial u}{\partial t} \right)^2 \quad (3.5)$$

A threshold can then be set, such that if the signal exceeds said threshold, for a determined “dwell time” the value of  $I(t) = 1$  at that time. Assuming that the measure described in Townsend (1956) did indeed use an unmodified frozen-flow hypothesis to obtain its spatial derivative, this measure is the same as Townsend’s with the addition of the second-derivative term.

### 3.2.3 Hedley and Keffer

Another measure, similar to the Wygnanski and Fiedler measure, was presented by Hedley and Keffer (1974). The identifier employed therein took into account both

---

2. A good derivation of this can be found on pp. 133-4 of Pope (2000).

streamwise and transverse components of velocity, but was identical in principle to the Wygnanski and Fiedler signal:

$$signal = \left( \frac{\partial^2 u}{\partial t^2} \right)^2 + \left( \frac{\partial u}{\partial t} \right)^2 + \left( \frac{\partial^2 v}{\partial t^2} \right)^2 + \left( \frac{\partial v}{\partial t} \right)^2 \quad (3.6)$$

This signal contains two components of the dissipation and the accompanying second derivative terms. The second derivative is employed in both this signal and the Wygnanski and Fiedler signal to account for realizations which are near an instantaneous “peak” in the  $u(t)$  time series. A sample time series which illustrates this is presented as Figure 3.1. Note that the first and second derivatives are frequently “out of phase”, in that one signal reaches a local maximum near the time of the other’s local minimum.

### 3.2.4 Activity Intermittency

An interesting “missing link” between the Wygnanski and Fiedler-type measure and measures using the absolute value of vorticity was the notion of “activity intermittency”. Certain portions of a time series of vorticity are observed to have a distinctly non-zero vorticity while possessing little to no high frequency content. This observation is contrary to the notion that a vortical flow should possess, to paraphrase Richardson, “big whorls, which have smaller whorls, and so on to viscosity”. To separate these apparently vortical, inactive regions from those regions clearly “vortical” both by measure of vorticity and activity, a measure based on a local standard deviation level was used. This method was employed by Haw et al. (1989).

### 3.3 Defining vortical: detailed considerations

With the general technical review of Section 3.2 accepted, the task of constructing a definition of what constitutes vortical flow remains. Ideally, all points in time not having a zero vorticity would be deemed vortical. Measurement uncertainty requires some non-zero threshold to be set. That is, if the vorticity at some time is beyond some determined threshold, it is deemed vortical. Figure 3.2 is a sample portion of one of the measured time series, and serves to illustrate this point. The question now arises as to what this threshold ought to be.

In the present work, this value was set by the following method: compute  $I(t)$  for some small threshold, with the understanding that all  $t$  having an  $\omega_z$  greater than threshold shall have an  $I(t)$  value of 1. Use this  $I(t)$  to compute  $\langle I \rangle$ , then increase the threshold by some small increment. Compute  $I(t)$  for this new threshold and compute the new  $\langle I \rangle$ . This procedure is repeated at many thresholds<sup>3</sup>. Figure 3.3 illustrates the results of such a procedure. Observe the sharp initial fall, followed by a “knee”, then a much lower rate of descent. The initial fall can be viewed as the “noise” region of the graph—the threshold is clearly too small. The slow fall in the higher threshold regions indicates that the value of  $\langle I \rangle$  is reasonably insensitive to changes in threshold. Therefore, the appropriate threshold is at the beginning of this slow fall region, or at the end of the “knee”. It should be noted that this precise location is not well defined, and is subject to the data analyst’s interpretation.

---

3. The computational time associated with this procedure can become quite large. It is recommended that the maximum threshold at which  $\langle I \rangle$  is computed be no more than the standard deviation of vorticity at the measurement location. This value should be large enough to observe the described trend in most flows.



The need for another necessary consideration in this procedure is illustrated by Figure 3.5. Clearly, the portions above and below the marked threshold limits are deemed vortical. In a vortical field, there exists regions of strongly negative and strongly positive vorticity. There also exists regions within this field which connect these strongly vortical regions. These connecting regions are measured as having near-zero vorticity (as shown in Figure 3.5). Despite their low magnitude of vorticity, these regions are understood to lie on the “vortical” side of the VSL.

To separate these connecting regions from truly non-vortical fluid, it is necessary to incorporate another consideration into the  $I(t)$  construction. Corrsin and Kistler (1955) proposed that the thickness of the VSL should be on a “viscous” length scale, the Kolmogorov scale. If the VSL has a characteristic thickness, it is easy to imagine that the folds in the interface also have some characteristic length scale associated with them. To the eye, this length scale would be characteristic of the smallest “lobe” of vortical fluid capable of projecting itself into the non-vortical fluid. Figure 3.6 is intended to clarify this point.

The most natural choice for this scale seems to be the local Taylor microscale ( $\lambda_t$ ). This quantity is computed by finding the zero-crossing of the “osculating” parabola of the initial portion of the autocorrelation of the transverse component of velocity. See Figure 3.7 for clarification. Landahl and Mollo-Christensen (1994) view the length analog of this scale (defined:  $\lambda_v = \lambda_t \times u$ ) as characterizing the size of the smallest “dynamically significant” eddies in the flow. Townsend (1956) proposed that since

$\lambda_v^2/\nu$  is proportional to the ratio of the total turbulent energy of the flow to the rate of loss of turbulent energy by dissipation, that  $\lambda_v^2/\nu$  is best viewed as a time scaling for the dissipative motions. Both interpretations are interesting, but it is the first which is perhaps most appropriate in the context of the current discussion.

If the smallest “dynamically significant” eddies in the flow are indeed characterized by the Taylor microscale, it is likely that this scale also characterizes the smallest “lobe” of vortical fluid capable of projecting itself into the non-vortical fluid. To separate the previously discussed “connecting regions” from truly non-vortical fluid, the Taylor time scale,  $\lambda_t$ , is used to scale a “dwell” parameter. That is, the measured vorticity must fall within the determined non-vortical thresholds for more than some (small) multiple of  $\lambda_t$  to be considered non-vortical.

Independent of an *a priori* notion of the proper scale, a procedure for finding a numerically appropriate “dwell” can be used. This is similar to the procedure used to determine the appropriate vorticity threshold. Figure 3.8 is intended to clarify this procedure. Each curve in Figure 3.8 represents the  $\langle I \rangle$  over a range of thresholds at different dwell time, measured as a multiple of  $\lambda_t$ . The smaller the spacing between curves, the less sensitive the measurement of  $\langle I \rangle$  is to a change in dwell time near that dwell time.

It should be noted that the character of Figure 3.3 is not preserved as the mean intermittancy value approaches 1. The algorithm is “trained” at a location where the  $\langle I \rangle$  is

near 0.3. This  $\langle I \rangle$  ensures that there is enough vortical and non-vortical fluid passing the probe to establish a rational threshold level. At this location, the appropriate threshold is assessed from a plot like Figure 3.3, and this value is used as the threshold for all transverse locations. The dwell time at each location was equal to  $2\lambda_t$ , where  $\lambda_t$  is the local Taylor time scale. The “2” multiplier was determined empirically, from Figure 3.8.

### 3.4 Comparison of Methods

It is clear that the threshold for each time-resolved method at a given transverse location can be set such that all of the methods yield very nearly the same mean. The “correct” level for each surrogate method can be set using the  $\langle I \rangle$  that is derived from the vorticity signal, as described in Section 3.3. Figure 3.9 depicts the  $\langle I \rangle$  at each transverse location after this setting procedure.

It should be noted that even though the values of  $\langle I \rangle$  are very close--the difference between each surrogate method and the “known” value from the absolute vorticity method is less than 0.5%--the measured transitions between vortical and non-vortical for  $I(t)$  are not the same for each processing method. The implications of this become clear in the context of the conditional statistics, examined in Chapter 4.

It is interesting to compare these results to the values of  $\langle I \rangle$  that are obtained when one of the surrogate methods is used independently. The

It is of some interest to assess how amenable the alternate methods are to a “training” procedure, as was employed for the vorticity-based method. Figure 3.10 shows, at each transverse location, the threshold level required to make the  $\langle I \rangle$  from the alternate

method match that of the vorticity-based method. It is instructive to note the degree to which the level changes as the measurement location moves in the transverse direction.

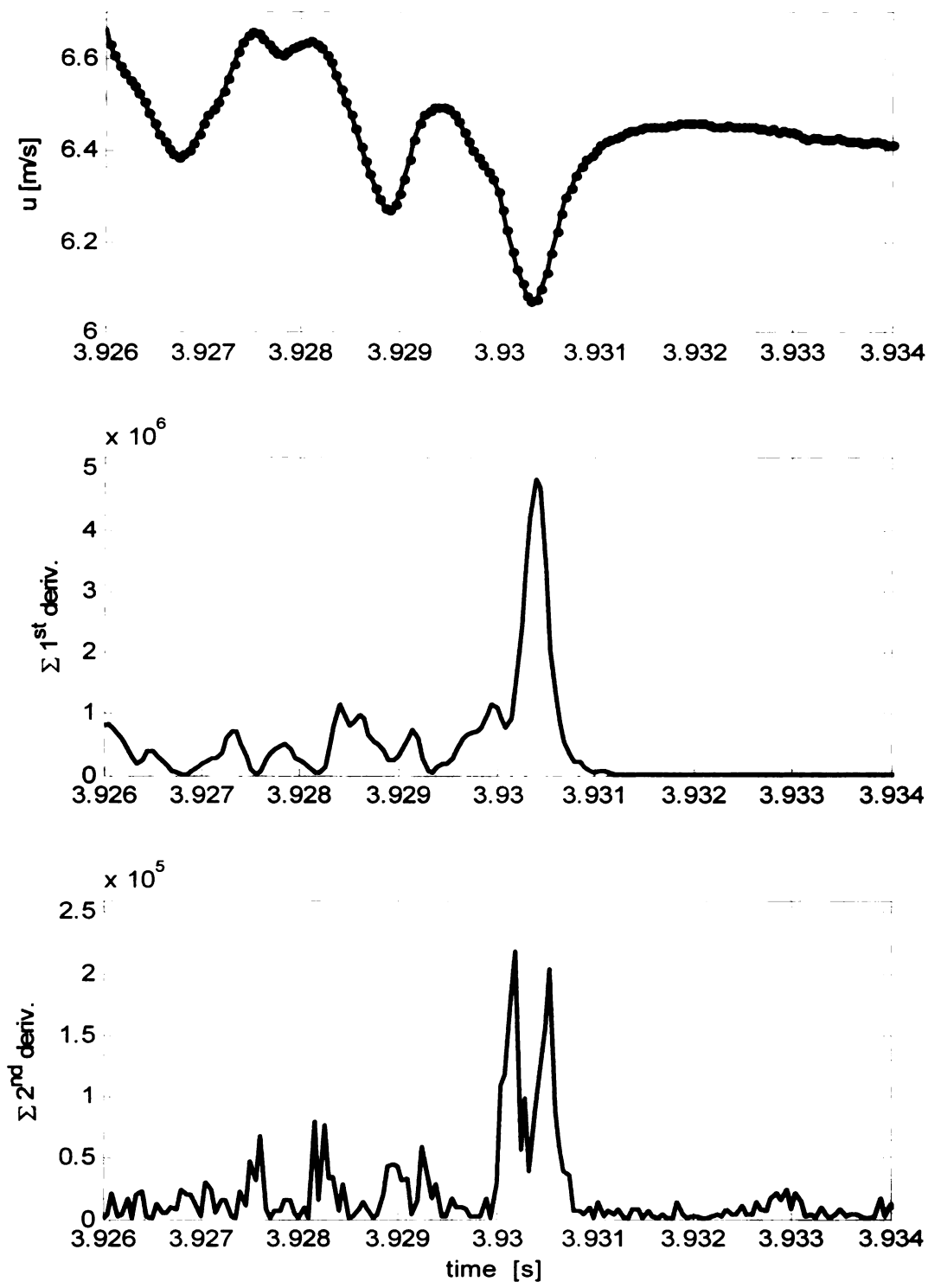
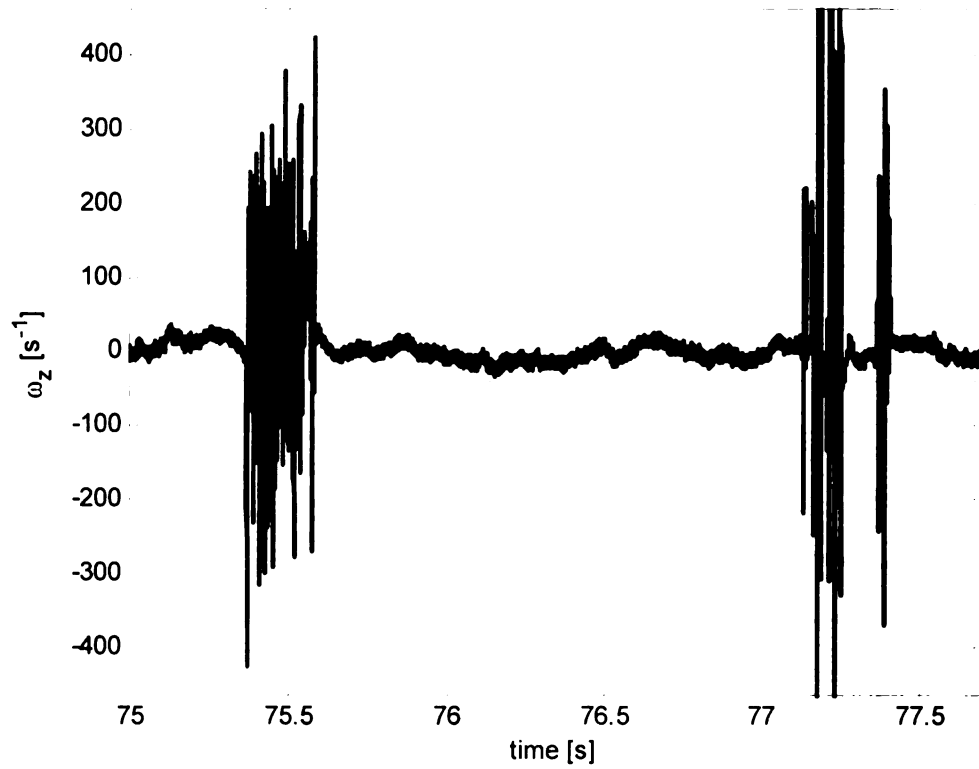


FIGURE 3.1 Sample time series and sum of first and second derivatives computed for the Hedley and Keffer signal. Note that the ordinate on the second derivative's set of axes is a factor of 20 smaller than that of the first derivative's.



**FIGURE 3.2** Sample vorticity time series with illustrative non-zero triggering thresholds.  
 The transverse location from which these data were taken was  $\eta = 2.46$ .  
 Figures 3.3, 3.4, 3.5, 3.7, and 3.8 were also created using data from this location.

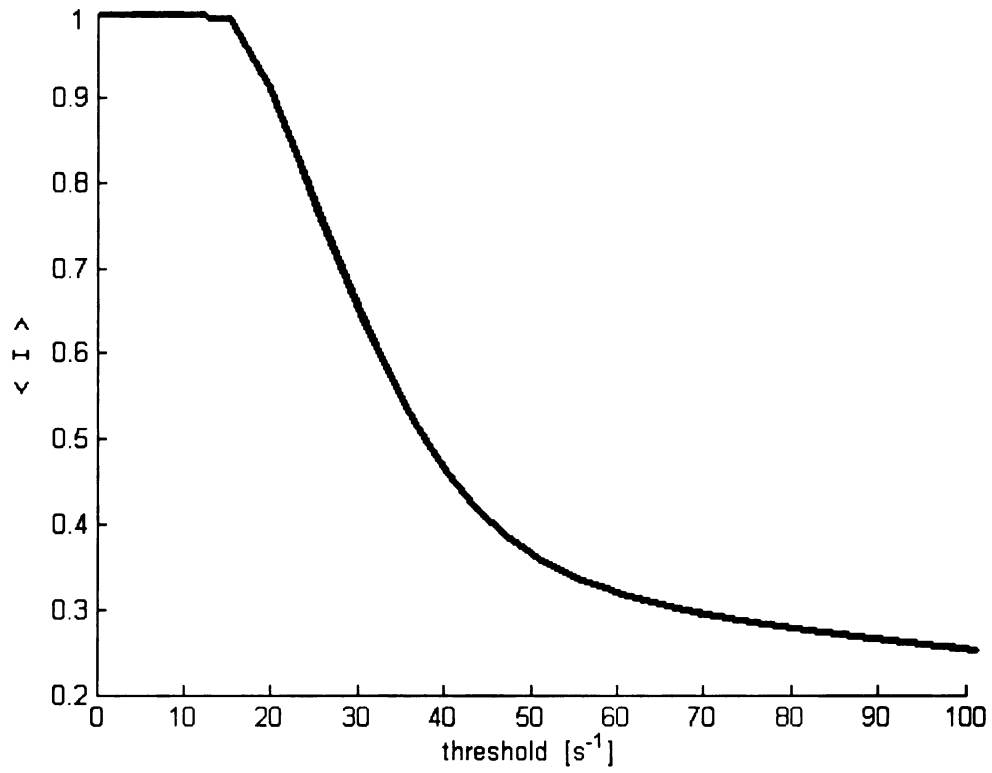


FIGURE 3.3 Average intermittency vs. vorticity threshold

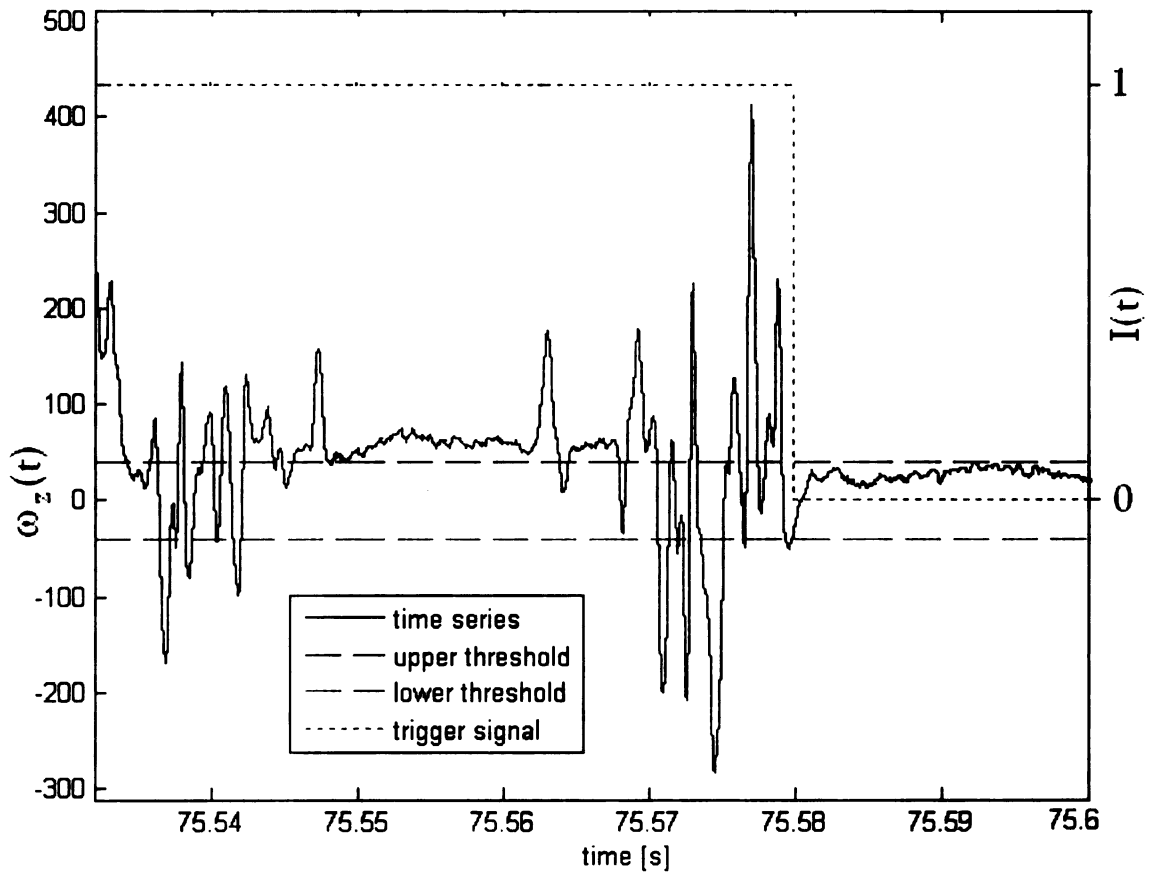
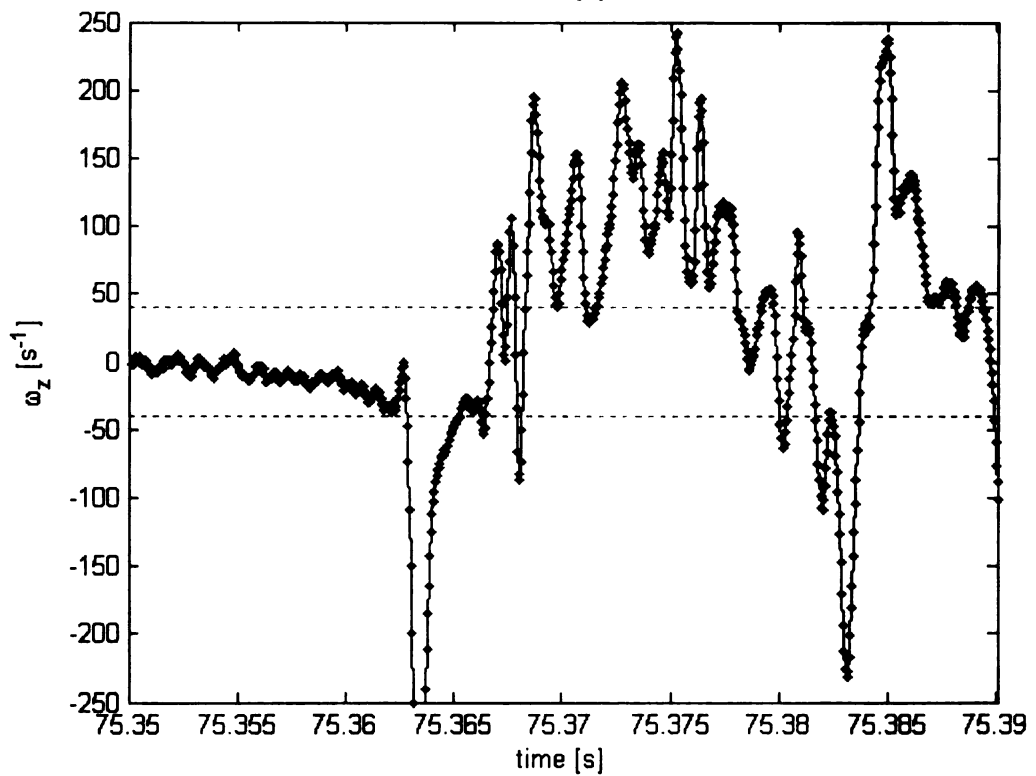
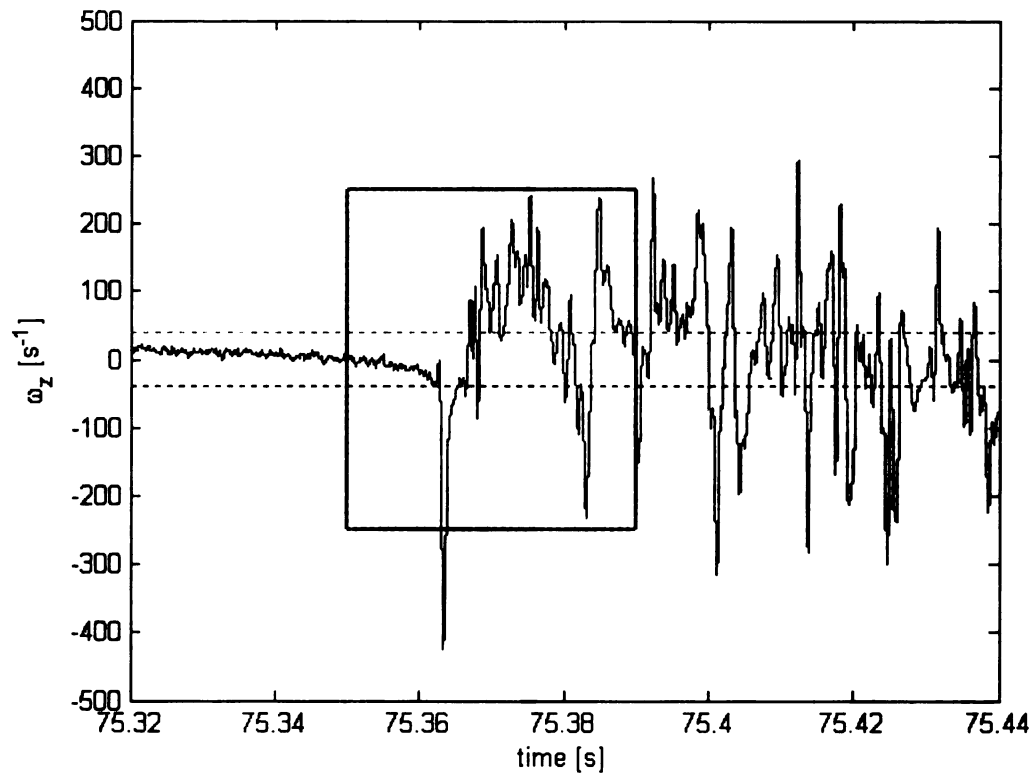


FIGURE 3.4 Vorticity time series with trigger signal





**FIGURE 3.5** Portion of vorticity time series illustrating the need for a “dwell” criteria. Location of the bottom axes is the boxed region on the upper axes. The “dots” on the bottom axes’ curve represent individual data points.

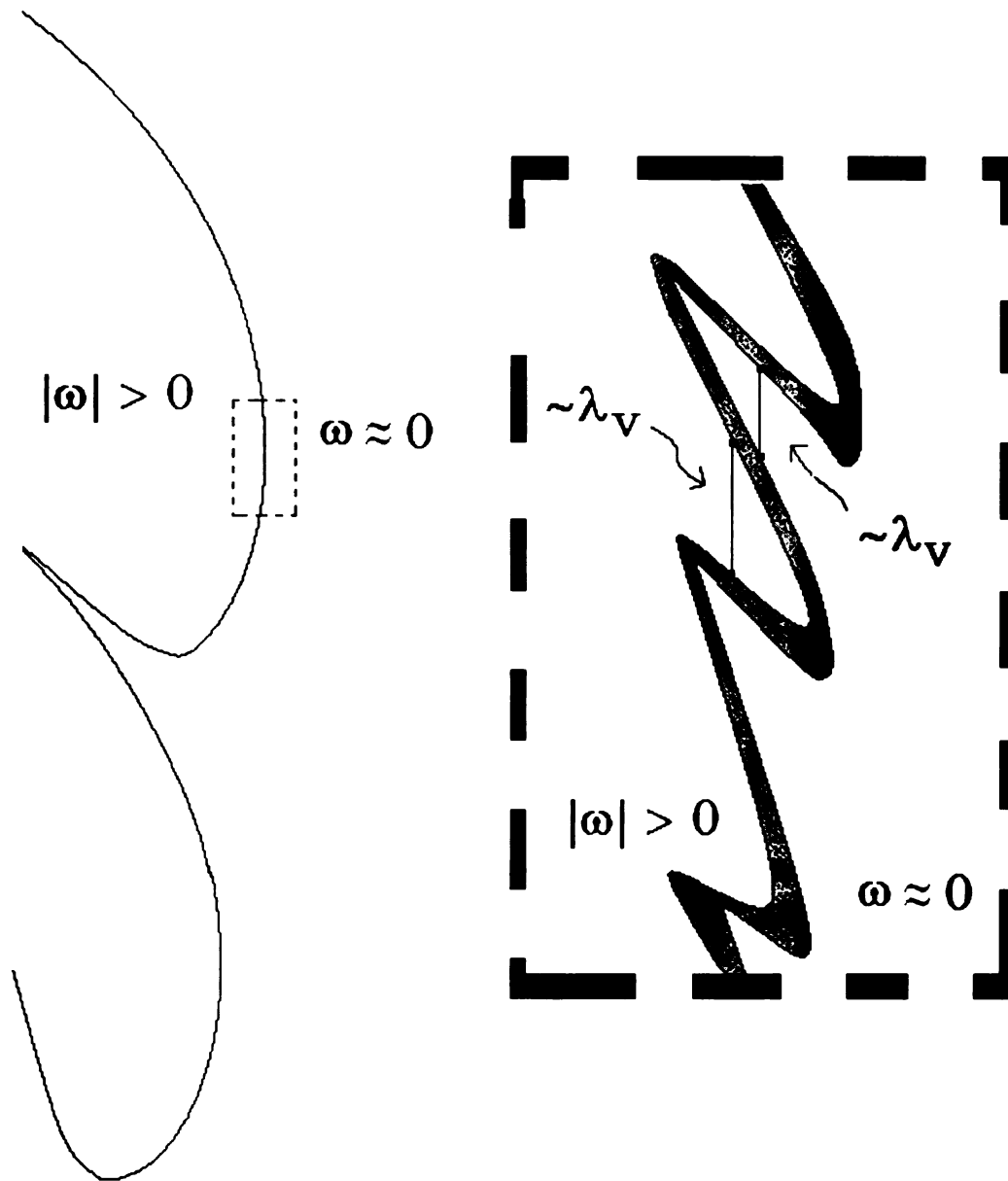
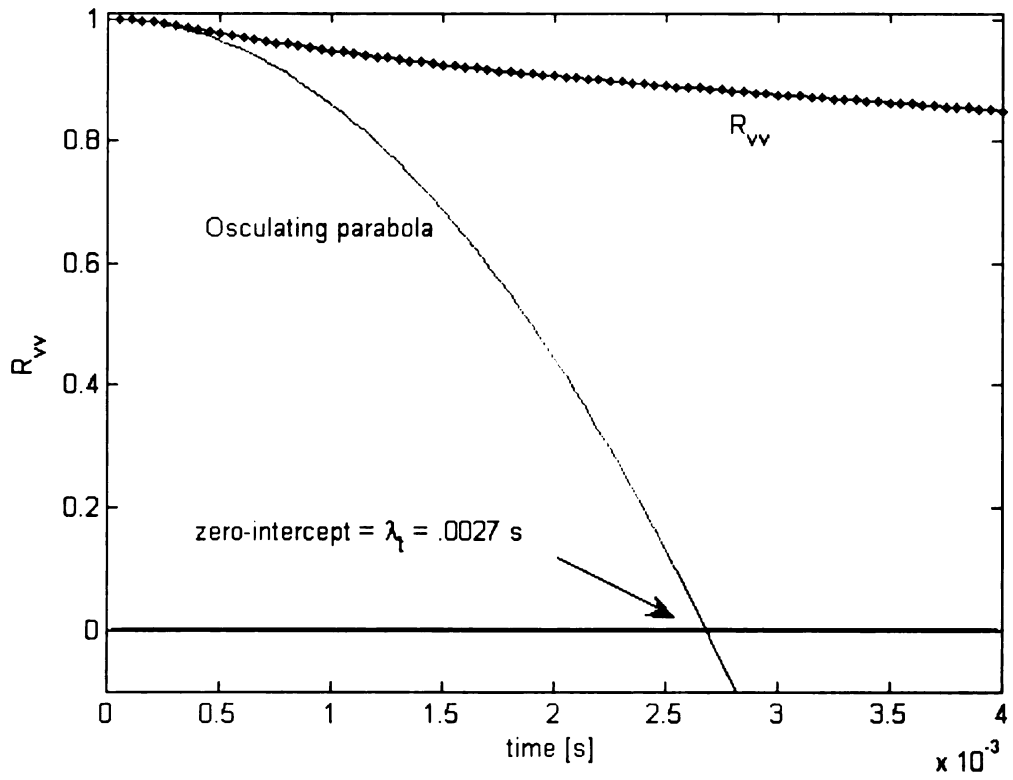


FIGURE 3.6 Proposed structure of VSL



**FIGURE 3.7 “Osculating” parabola of transverse velocity autocorrelation illustrating the definition of the Taylor microscale.**

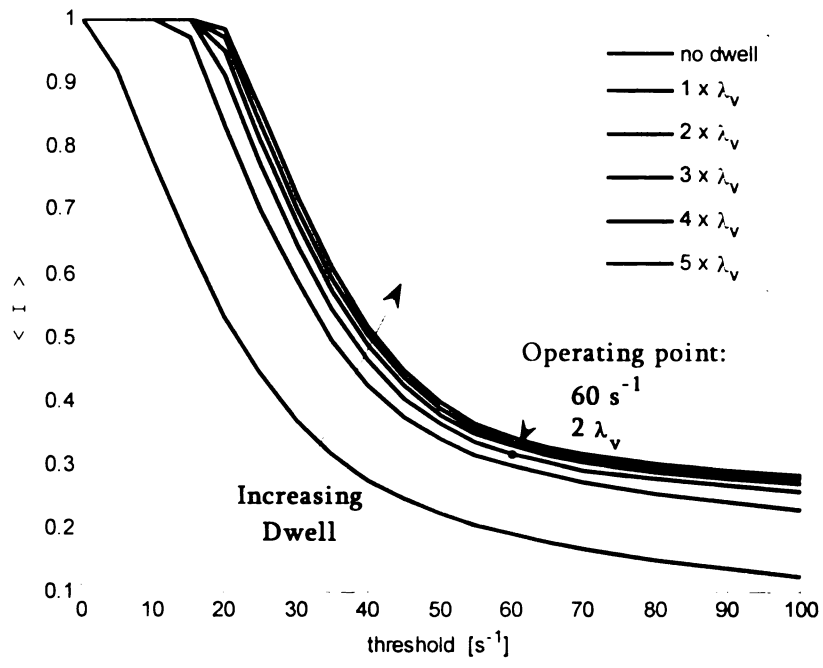


FIGURE 3.8 Sensitivity of the technique to increasing dwell time. Each curve represents a different dwell time, measured as a multiple of  $\lambda_t$ .

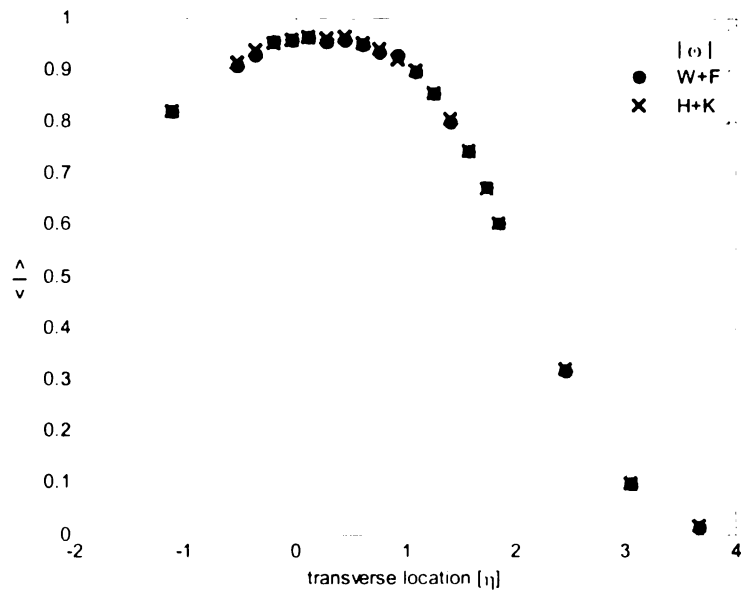


FIGURE 3.9 Mean intermittency using the absolute magnitude of vorticity measure, the Wygnanski and Fiedler measure and the Hedley and Keffer measure, *after* the surrogate techniques have been “trained” to match the vortical measure.

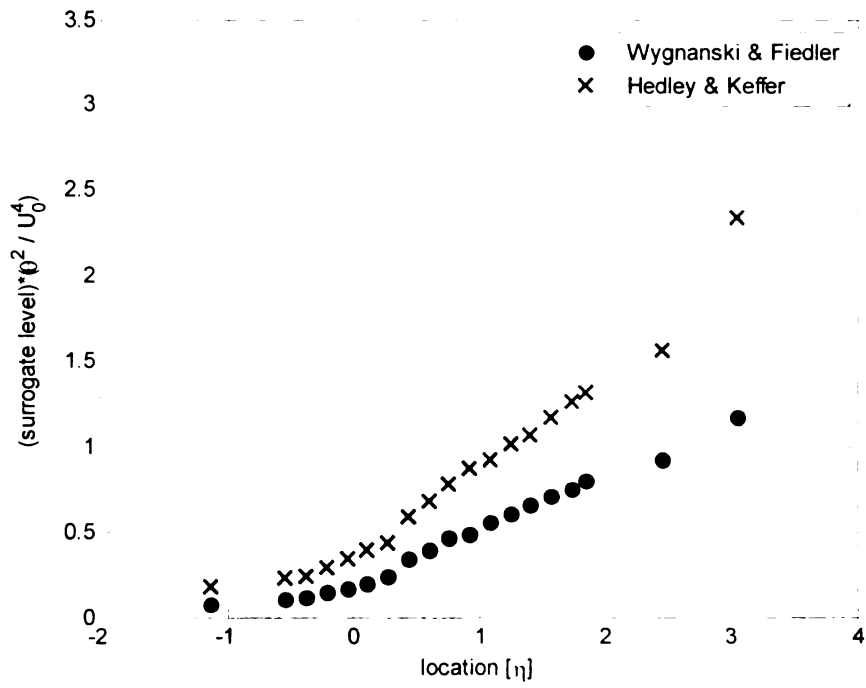


FIGURE 3.10 Required threshold level, non-dimensionalized by  $\theta^2 / U_0^4$ , needed to match the  $\langle I \rangle$  measured by the vorticity method.'

## 4.0 VSL properties and conditional statistics

### 4.1 Properties of the VSL

#### 4.1.1 Description of the VSL

Phillips (1972), describes the VSL as consisting of “billows” of vortical fluid propagating into the vortical fluid separated by re-entrant “wedges” of non-vortical fluid. An illustration of this is provided as Figure 4.1. An important result derived by Phillips is that a region of positive curvature with respect to the non-vortical fluid--a nascent wedge--will continue to increase its positive curvature until it becomes infinite or reaches some physical maximum. A cartoon illustrating this process is provided as Figure 4.2. This result is used to justify the view of the small-scale features of the VSL proposed by Figure 3.6, and which will be further elaborated upon in the following sections.

#### 4.1.2 Condition Duration

Once a passage of the VSL has been detected, it is natural to ask for what amount of time or space this particular vortical/non-vortical region lasts. The probability density distributions of conditional duration in time at each transverse location are presented on logarithmic axes in Figures 4.3, 4.4, 4.5, and 4.6. The values have been non-dimensionalized by the local Taylor microscale  $\lambda_T$ .

As the duration becomes long, the probability that a condition's region will last for a particular time becomes extremely small. This leads to regions of zero probability in the distribution, since the flow at each measurement location could not be sampled for a long enough time to capture the true probability of these rare events. To better

approximate the true (continuous) distribution, the probability of 20% of each decade was averaged. These average probabilities form a more continuous distribution than the “raw” computed probabilities. Notice that all distributions are strongly non-Gaussian and positively skewed. The strong positive skewness of these distributions implies that the VSL is rich in small-scale features. The mean values of each distribution, shown as one vertical line in per condition, per distribution, demonstrate the expected trend. Near the free stream, the mean duration for the non-vortical condition is very long, and decreases as the shear layer center is approached. The mean duration for the vortical condition is shorter near the free stream, and increases as the shear layer center is approached.

The probability density distribution of conditional duration in space is presented in Figures 4.7, 4.8, 4.9, and 4.10. The values have been non-dimensionalized by the momentum thickness of the shear layer at  $x/\theta_0 = 484$ . Figure 4.11 is intended to clarify the method used to obtain these statistics. The durations in time were computed, as for Figures 4.3- 4.6. Then the average streamwise velocity between the passings of the VSL was multiplied by each duration. These “durations in space” imply, per a local Taylor approximation, the relative size of the “bulges” from Phillips’ model of the VSL.

These figures have several interesting features. First, note the similar character of the trends with respect to transverse location in mean duration length for each condition, compared to the mean duration times from Figures 4.3- 4.6. The vortical mean length becomes longer as the measurement location moves toward the shear layer center, and

the non-vortical mean length becomes shorter. The vortical mean duration in time increases by a factor of 8 as the measurement location moves from  $\eta = 3.04$  to  $\eta = 0.60$ . In contrast, the vortical mean duration in length increases by only a factor of 2.5 over the same span.

#### 4.1.3 Appearance of the VSL

A “rake” of hot-wire probes was used to obtain information about the geometry of the VSL. An illustration of this rake, as well as a cartoon of the approaching VSL, is provided in Figure 4.12. The rake consists of a single vorticity probe flanked by two X probes. The distance between neighboring probes’ measurement regions was 1 cm. The Hedley and Keffer (1974) algorithm, from Section 3.2.3, was employed to obtain an  $I(t)$  signal from the X probes.

The quantity measured by this rake was the angle of the VSL relative to the transverse direction, as shown in Figure 4.12. The timing scheme used in computation is shown in Figure 4.13. The angles  $\theta_1$  and  $\theta_2$  were computed as follows:

$$\theta_1 = \text{atan} \frac{\overline{u(t_b \leq t \leq t_a)} \times \delta t_1}{\text{probe spacing}} \quad (4.1)$$

$$\theta_2 = \text{atan} \frac{\overline{u(t_c \leq t \leq t_b)} \times \delta t_2}{\text{probe spacing}} \quad (4.2)$$

As noted previously, probe spacing was 1 cm. Note that a “locally frozen” Taylor hypothesis was employed. This hypothesis assumes that the velocity of the VSL relative to the local convection velocity is small with respect to the local convection veloc-



ity. A restriction was also imposed on the measured “sharpness” of the front. Referring back to Figure 4.12, the difference between  $\theta_1$  and  $\theta_2$  was capped at 45 degrees.

This result of this processing was two bodies of data. One body will consist of the “entering” angles, when the VSL passage implies a change from non-vortical fluid to vortical fluid. The other body of data comprises the “leaving” angles, when the VSL passage implies a change from vortical fluid to non-vortical fluid. The result of this processing is presented in Figure 4.14 as probability density distributions. It is notable that an “entering” VSL is preferentially associated with positive angles and a “leaving” VSL with negative angles. These data are qualitatively consistent with Phillips’ view of the VSL. (Refer to Figure 4.1)

It is also interesting to view these data as the ratio of the probability “entering” to the probability of a “leaving” for a given angle. This is presented in Figure 4.15, with a logarithmic ordinate. An example interpretation of this figure is as follows: if the VSL is measured to have crossed at an angle of 60 degrees, it is approximately 10 times more likely that the flow at the measurement location went from non-vortical to vortical (entering).

## **4.2 Conventional Statistics**

It is useful, prior to the discussion of the velocity field’s conditional statistics, to examine the unconditioned (conventional) statistics of the field. Comparisons to the data presented in Morris (2002), henceforth “Morris”, will be the focus of this section.

The mean value of streamwise velocity, non-dimensionalized by free stream velocity, is shown in Figure 4.16. The matching data of Morris are also presented. These data agree to within 1.5% of free stream speed.

The standard deviation values of the streamwise and the transverse components of velocity, non-dimensionalized by free stream velocity, are presented in Figure 4.17 and Figure 4.18, respectively. The matching data of Morris are also presented. Note that the peak streamwise value from the current work is slightly lower than that presented in Morris, while the peak transverse value from the current work is slightly higher than that of Morris.

The skewness values of the streamwise component of velocity are presented in Figure 4.19. Note that the skewness decreases from near the free stream to a minimum value near  $\eta = 1.6$ . This is reasonable, since positive fluctuations are nominally bounded by the free stream velocity, while negative fluctuations are bounded by zero. The value of  $\bar{u}/U_0$  at  $\eta = 1.6$  is approximately 0.85. The increasing skewness in the range  $-1.09 < \eta < 1.6$  is a reflection of the increasing positive excursions from the mean relative to the negative excursions from the mean.

The Reynolds stress,  $\overline{u'v'}$ , non-dimensionalized by the square of free stream velocity, is presented in Figure 4.20. The matching data of Morris from two streamwise locations,  $x/\theta_0 = 384$  and  $x/\theta_0 = 675$  are also presented. The spread of data within Morris indicates that the agreement between Morris and the present work is not unreasonable.

## 4.3 Conditional Statistics

### 4.3.1 Description and Definition

Conditional statistics can be defined as follows: “Given a set of observations for which condition A holds, what is the value of statistical measure B?” For example, one may be interested in the skewness (measure) of the streamwise component of velocity during the vortical (condition) portions of the record. The import of these types of statistics is in separating effects unique to the vortical flow from those unique to the irrotational flow.

The conditional properties discussed in the present work were computed as follows: (understanding that a single overbar implies standard mean, shown below)

$$\bar{\alpha} = \lim_{T \rightarrow \infty} \frac{1}{T} \int_0^T \alpha dt \approx \frac{1}{N} \sum_{i=1}^N \alpha_i \quad (4.3)$$

where N is the number of samples.

Vortical mean:

$$\bar{u}_\omega = \frac{\overline{u(x, t)I(x, t)}}{\overline{I(x, t)}} \quad (4.4)$$

Vortical rms:

$$\tilde{u}_\omega = \left( \frac{\overline{(u(x, t) - \bar{u}_\omega)^2 I(x, t)}}{\overline{I(x, t)}} \right)^{1/2} \quad (4.5)$$

Vortical skewness:

$$u_{\omega Sk} = \frac{\overline{(u(x, t) - \bar{u}_{\omega})^3 I(x, t)}}{(\tilde{u}_{\omega})^3 \overline{I(x, t)}} \quad (4.6)$$

Vortical cross-correlation coefficient:

$$\left. \frac{\overline{u'v'}}{\tilde{u}\tilde{v}} \right|_{\omega} = \frac{\overline{(u(x, t) - \bar{u}_{\omega})(v(x, t) - \bar{v}_{\omega})I(x, t)}}{\tilde{u}_{\omega}\tilde{v}_{\omega}\overline{I(x, t)}} \quad (4.7)$$

The non-vortical conditional properties can be computed by substituting  $(1-I(x,t))$  for  $I(x,t)$ , and the appropriate conditional mean and rms, where appropriate. The subscript “ $\omega = 0$ ” will be used to designate these conditional statistics.

Note that the conditional mean and standard deviation have been used in the definition of the higher-order statistics. This is to remove the effects of any offset between these conditional statistics and those statistics taken from the total record.

#### 4.3.2 Conditional Mean, Streamwise Component

The streamwise vortical mean and streamwise non-vortical mean velocity are presented in Figure 4.21. Several features are evident. In the high-speed region, vortical fluid has a lower mean streamwise velocity, and in the low-speed region, vortical fluid has a higher mean streamwise velocity. This is reasonable--consider that the sheared fluid comprising the flow's vortical region has reached this state by the mixing of high velocity fluid with low velocity fluid. The mixed fluid at any location contains some amount of accelerated low speed fluid and decelerated high-speed fluid. Thus, the mixed fluid should be expected to have a velocity closer to the average velocity between the potential streams ( $0.5 U_0$ ) than will the nearby unmixed fluid.

### 4.3.3 Conditional Mean, Transverse Component

The transverse vortical mean and transverse non-vortical mean velocity are presented in Figure 4.22. Several features are evident. Mean transverse vortical velocity goes from a positive value near the free stream, to a negative value as the shear layer center is approached. This result is reasonable. Since vorticity is imparted to a fluid element only through the direct action of viscosity, a vortical fluid element cannot originate in the free stream. The mean positive transverse velocity of these vortical elements is likely a reflection of these elements' origin nearer the shear layer center.

The mean transverse non-vortical velocity goes from near zero to a strong negative value to a positive value as the measurement location moves from  $\eta = 3.04$  to  $\eta = 0$ . These results are reasonable, especially when viewed in the context of the VSL. Since a non-vortical fluid element originated in either the high-speed free stream or the entrainment stream, it is reasonable that a non-vortical fluid element which exists near the shear layer center has a large (positive or negative) transverse velocity reflecting its origin in one of the two non-vortical streams<sup>1</sup>. The increasingly negative mean transverse velocity as the measurement location approaches the shear layer center is a likely indication that a large fraction of the non-vortical elements at these locations originated in the free stream. Similarly, the increasing sign in the region  $-0.37 \leq \eta \leq 0.75$  is a likely indication that an increasing fraction of the non-vortical elements originated in the entrainment flow.

---

1. Figure 4.24 and its accompanying discussion provides further evidence of this claim.

#### 4.3.4 Conditional Standard Deviation, Streamwise and Transverse Velocity Components

The vortical and non-vortical streamwise velocity standard deviations are presented in Figure 4.23. The vortical standard deviation is considerably higher than the non-vortical value in the region  $0.60 \leq \eta \leq 3.04$ . This is rational in the sense that fluid elements comprising the non-vortical ensemble near the free stream all originated in the free stream, whereas the vortical ensemble is comprised of fluid elements having a much wider range of velocity histories.

The vortical and non-vortical streamwise standard deviation values are of comparable magnitude in the region  $-1.13 \leq \eta \leq 0.43$ . The likely explanation for this phenomenon is that the comparatively large non-vortical values are the result of the unsheared fluid entering from both the entrainment stream and the primary stream. Under this hypothesis, the large measured standard deviation is the result of two distinct “processes” bringing unsheared fluid at two widely disparate speeds to the shear layer center.

This explanation is supported by the measured values of the standard deviation of the transverse component of velocity, presented in Figure 4.24. The non-vortical value is smaller than the vortical value in the region  $3.04 \geq \eta \geq 0.65$ . In the region  $0.65 \geq \eta \geq 1.13$ , the conditions have similar standard deviation.

To assess whether large streamwise fluctuations are correlated with large transverse fluctuations, a joint probability density distribution of the non-vortical streamwise and transverse velocity fluctuations at  $\eta = 0.05$  was evaluated. It is presented in

Figure 4.25. The character of this plot supports the “two-process” explanation of the large standard deviation values. The “island” in Quadrant II is composed of lower than mean streamwise velocities and higher than mean transverse velocities. The ensemble of fluid elements this island represents likely originated in the entrainment flow. Conversely, the “island” in Quadrant IV is composed of higher than mean streamwise velocities and lower than mean transverse velocities, indicating that the ensemble of fluid elements it represents likely originated in the primary flow.

#### 4.3.5 Conditional Skewness, Streamwise Velocity Component

The vortical and non-vortical streamwise velocity skewness values are presented in Figure 4.26. Note that the skewness of the vortical streamwise component of velocity increases approximately monotonically from the free stream to the low speed side. This result is reasonable. Near the free stream, the distribution is negatively skewed. The nominal upper bound of streamwise velocity (velocity of the free stream) is closer to these distributions’ mean than is the streamwise velocity lower bound (zero). Therefore, it is reasonable that the magnitude of negative deviations from the mean are larger than positive deviations from the mean. As the observation point moves toward the center of the shear layer, the distribution becomes more symmetric. Near the entrainment stream, the distribution is positively skewed. Since the streamwise velocity lower bound (zero) is closer to these distributions’ mean than is the streamwise velocity upper bound (velocity of the free stream), a positive skewness in this region is reasonable. Three representative histograms that demonstrate these skewness values are presented in Figure 4.27.

The skewness of the non-vortical streamwise component of velocity is nearly zero in the free stream, and remains so until  $\eta \approx 1.85$ . This is reasonable, since the fluid elements making up the non-vortical ensemble in the near free stream locations likely all originated in the free stream. These elements have not undergone shearing, and thus variations in the non-vortical velocity values are random and unskewed.

For values of  $\eta < 1.85$ , the skewness of the non-vortical streamwise velocity decreases to a minimum at approximately  $\eta = 0.92$ , then increases, becoming positive at approximately  $\eta = 0.24$ . A hypothesis explaining this behavior is as follows: the increasingly negative skewness for  $1.85 \geq \eta \geq 0.92$  implies that an increasing amount of the non-vortical fluid at these locations has come to the measurement location from the entrainment stream. Near  $\eta = 0.92$ , the number of “entrainment elements” is sufficiently small that the mean is not greatly affected. As a statistical moment’s order increases, it is affected more by large excursions from the mean. Therefore, the skewness is made negative by these entrainment elements.

As the measurement location moves toward the shear layer center from  $\eta = 0.92$ , an increasingly larger fraction of the non-vortical ensemble is composed of fluid which originated in the entrainment stream. This decreases the mean non-vortical streamwise velocity. The “bounding” arguments proposed earlier regarding the vortical skewness are again useful. A decrease in an ensemble’s mean value likely causes the magnitude of positive deviations from the mean to be larger than negative deviations



from the mean. This effect increases the skewness of the distribution representing the ensemble. The non-vortical streamwise skewness is approximately zero at  $\eta = 0.24^2$ .

#### 4.3.6 Reynolds Stress

The vortical and non-vortical kinematic Reynolds shear stresses, divided by the product of the transverse and streamwise standard deviation--that is, the conditional correlation coefficients--are presented in Figure 4.29. It is interesting to see that the vortical coefficient remains reasonably constant as the measurement location moves in the transverse direction. This implies that the vortical flow is of reasonably universal character throughout. Per the Prandtl argument (see Potter and Foss (1975)) as it applies to this geometry, flow with a higher streamwise velocity than the vortical average possesses a lower than average transverse velocity, and vice-versa. Thus, the mean product of the streamwise and transverse fluctuations will have a negative sign. The non-dimensional Reynolds stress is presented in Figure 4.30.

It is also instructive to note that the correlation between streamwise and transverse fluctuations in the non-vortical fluid near the free stream is not as strong as for vortical fluid. The likely explanation for this is that the vortical fluid's fluctuations are increased by both the pressure field and shear forces, whereas the non-vortical fluid's fluctuations result only from the pressure field. It is interesting to note that the non-vortical correlation coefficient is non-zero at the measurement location nearest the free stream ( $\eta = 3.04$ ). Since the non-vortical velocity fluctuations near the free

---

2. It is interesting to note that the location of peak mean shear corresponds very closely with  $\eta = 0.24$ . This is shown in Figure 4.28.

stream are a result only of fluctuations in the pressure field, the model of fluctuations presented in Figure 4.31 could have been reasonably expected. In this scenario, the velocity magnitude would have remained relatively constant, with fluctuations in velocity components resulting from fluctuations in the flow direction. Since the scenario shown in Figure 4.31 is not reflected in the data, it is likely that the pressure field is related to the large-scale structure of the vortical region.

In contrast to its small values near the free stream, the non-vortical coefficient is strongly negative near the shear layer center, more so than the vortical flow there. The previous discussion of Figure 4.25 (see Section 4.3.4) is useful for explaining this observation. This figure shows the strong correlation between negative transverse/positive streamwise fluctuations and vice-versa. Furthermore, Figure 4.25 supplies more evidence in support of the hypothesis that the strong correlation near the shear layer center is not the result of one ensemble of fluid with strongly coupled streamwise and transverse fluctuations, but instead of two ensembles of fluid which together create a strong correlation.

#### 4.4 Conditional Autocorrelation

The standard short time averaged autocorrelation is defined (Bendat and Piersol (1986)) as follows:

$$R_{uu}(t_1, t_1 + \tau) = \frac{1}{T} \int_{t_1}^{(t_1 + T)} u(t)u(t + \tau)dt \quad (4.8)$$

A conditional autocorrelation can also be defined, provided some care is taken. The number of time steps to which the correlation was computed was half of the dwell time (described in Section 3.3 on page 34).

$$R_{uu}(t_1, t_1 + \tau) = \frac{1}{N} \sum_{n=0}^N (u(t_n) - \bar{u})(u(t_n + \tau) - \bar{u}) \quad (4.9)$$

In Equation 4.9,  $N = (\text{dwell time}) \times (\text{data frequency})$ ,  $t_1$  is  $N/2$  samples after the crossing of the VSL. The complete autocorrelation for one vortical or non-vortical burst is given by computing  $R_{uu}$  for  $\tau = \frac{(-N/2, -(N/2)+1, \dots, (N/2)-1, N/2)}{(\text{data frequency})}$ . The resulting autocorrelation can then be averaged at each time lag over the set of all bursts. This average is analogous to the averaged autocorrelation of the entire (conditioned) signal. Note the use of the conditional average rather than that of the full record.

Figure 4.32 depicts the vortical and non-vortical autocorrelation of streamwise fluctuations at several transverse locations on the high speed side of the shear layer. Two things are immediately evident. First, the non-vortical velocity remains more correlated over time than does the vortical velocity. This result is reasonable, since the strongly irregular nature of the vortical field will cause the vortical flow at some time  $t + \Delta t$  to look less like the flow at time  $t$  than would have been the case in a non-vortical flow.

Second, the non-vortical correlation is far less sensitive to transverse position than is the vortical correlation. This relative insensitivity of the non-vortical correlation is

likewise reasonable--a patch of non-vortical fluid looks essentially uniform throughout its duration. The relative sensitivity to position of the vortical fluid is perhaps best examined in light of Figure 4.23. As the measurement location approaches the shear layer center, the magnitude of fluctuations in the vortical fluid increases, increasing the rate at which its autocorrelation descends. It is important to note that this same process is not in effect on the non-vortical flow at these central locations, despite the fact that the conditional standard deviation of the non-vortical fluid (Figure 4.23) is similar in magnitude to that of the vortical fluid at these locations. This is further support of the hypothesis that the large magnitude of non-vortical fluctuations near the shear layer center is not the result of one highly-fluctuant process but instead of non-vortical fluid being brought to near the center from both the low-speed and high-speed sides.

#### 4.5 Components of the Turbulence Kinetic Energy (TKE) Equation

The turbulence kinetic energy (TKE) equation is written as<sup>3</sup>:

$$\frac{\partial K}{\partial t} + \overline{U_j} \frac{\partial K}{\partial x_j} = - \frac{\partial U_i}{\partial x_j} \overline{u_i u_j} - \varepsilon - \frac{1}{\rho} \frac{\partial}{\partial x_i} \overline{(p u_i)} + \nu \nabla^2 K - \frac{\partial}{\partial x_j} \overline{(u_j (u_i^2 / 2))} \quad (4.10)$$

where  $i, j = 1, 2, 3$ , and 1,2,3 are understood to refer to the streamwise, transverse and spanwise directions, respectively.

A small subset of these terms will be considered in the present work. A more complete treatment of the terms of this equation in the SSSL can be found in Morris (2002). The

---

3. A derivation of the equation in its presented form can be found in Bernard & Wallace (2002).

dissipation  $\varepsilon$ , will be modeled using an isotropic assumption. Components of the turbulent diffusion that are contained in that term's transverse derivative,  $u^2\nu$ ,  $uv^2$  and  $v^3$ , will also be considered.

#### 4.5.1 Dissipation

Dissipation is defined as

$$\varepsilon = \nu \overline{\left(\frac{\partial u_i}{\partial x_j}\right)^2} + \nu \overline{\left(\frac{\partial u_i}{\partial x_j} \times \frac{\partial u_j}{\partial x_i}\right)} \quad (4.11)$$

where the second term of Equation 4.11 is identically zero in homogeneous turbulence<sup>4</sup>. In homogenous turbulence, the identity

$$\frac{\varepsilon}{\nu} = \overline{\omega_i^2} \quad (4.12)$$

also holds. If a further simplification to isotropy is also made, the relation

$$\varepsilon = 3\nu\overline{\omega_z^2} \quad (4.13)$$

holds. This final relation was conditionally evaluated and is presented as Figure 4.33.

The large difference between vortical and non-vortical dissipation are clear from this

figure. This result was expected since  $\overline{\omega_z^2}$  is by definition larger in vortical fluid. That

the dissipation is not measured to be zero in non-vortical fluid is a relic of the non-

zero threshold and finite dwell time used to determine whether the fluid at time  $t$  is

vortical. These considerations were detailed in Section 3.3.

---

4. Bernard and Wallace (2002) presents evidence that the magnitude of this term is very small even in the presence of large mean shear.

It is of interest to know whether the values of  $\varepsilon$  obtained by the above approximation are reasonable. To assess this, the unconditioned dissipation was compared to four measures computed in Morris (2002). This is shown in Figure 4.34. Note that the unconditioned isotropic approximation of dissipation computed (see Equation 4.13) for the present work lies relatively close to the isotropic approximation of Morris (2002). This agreement gives some confidence that the conditional measures are reasonable.

#### 4.5.2 Components of turbulent diffusion

The triple products of unconditioned and vortical fluctuating velocity are presented in Figure 4.35 and Figure 4.36 respectively. These figures show a strong resemblance to one another, with the major qualitative difference being the larger magnitudes of the vortical value near the free-stream. The difference between vortical and unconditioned values is shown in Figure 4.37. The larger magnitude in the vortical values near the free stream is intuitively reasonable--it is expected that terms characteristic of turbulent kinetic energy will be larger in vortical fluid.

The triple products of non-vortical fluctuating velocity are presented in Figure 4.38. Comparison to Figure 4.36 reveals that the analogous products for the vortical condition are approximately half the magnitude of the non-vortical condition. This result, contrary to what might be expected, is likely related to the "two-process" behavior proposed previously in light of Figure 4.25. Under this hypothesis, the large values of these triple products are not the result of what would be called true turbulent diffusion, but are instead the result of the non-vortical ensemble being composed of fluid which originated from two sources of different velocity.

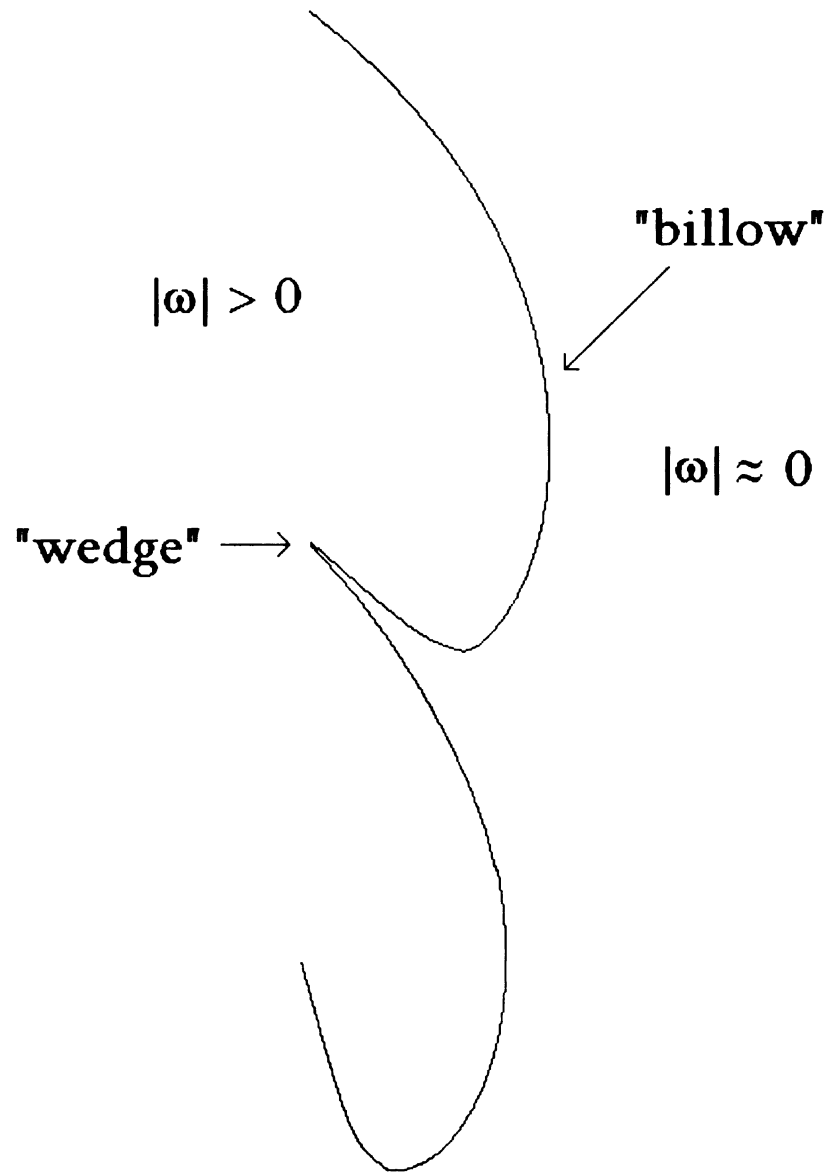


FIGURE 4.1 Illustration of a conceptual view of the VSL proposed by Phillips (1972)

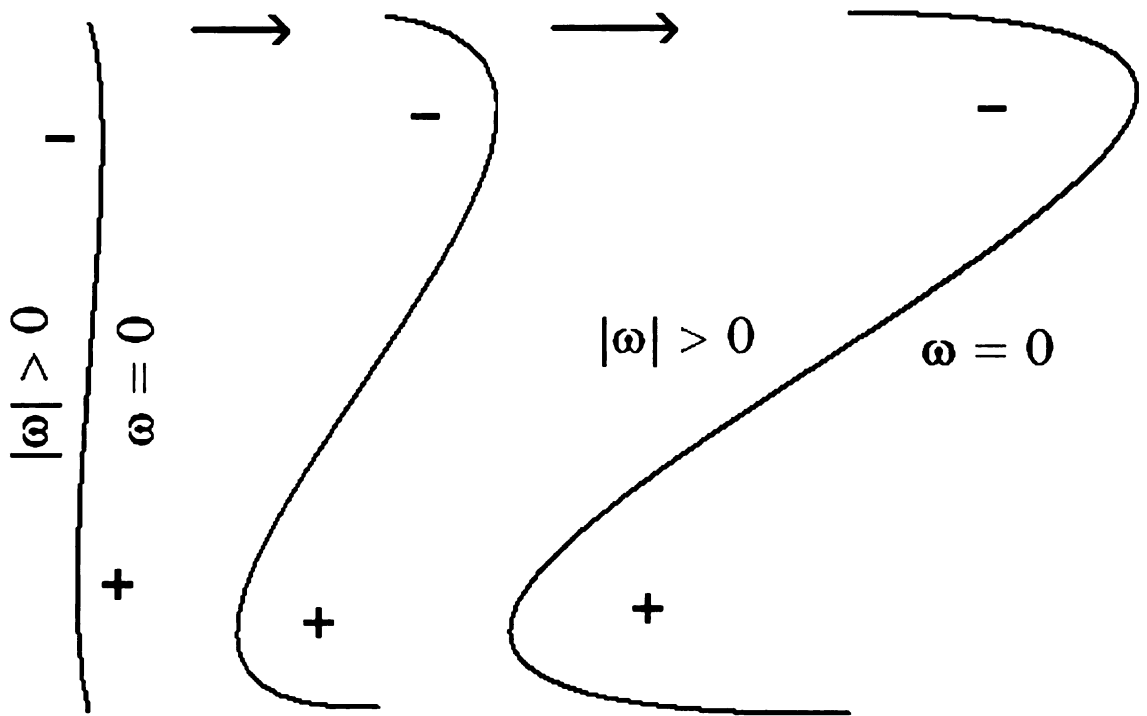
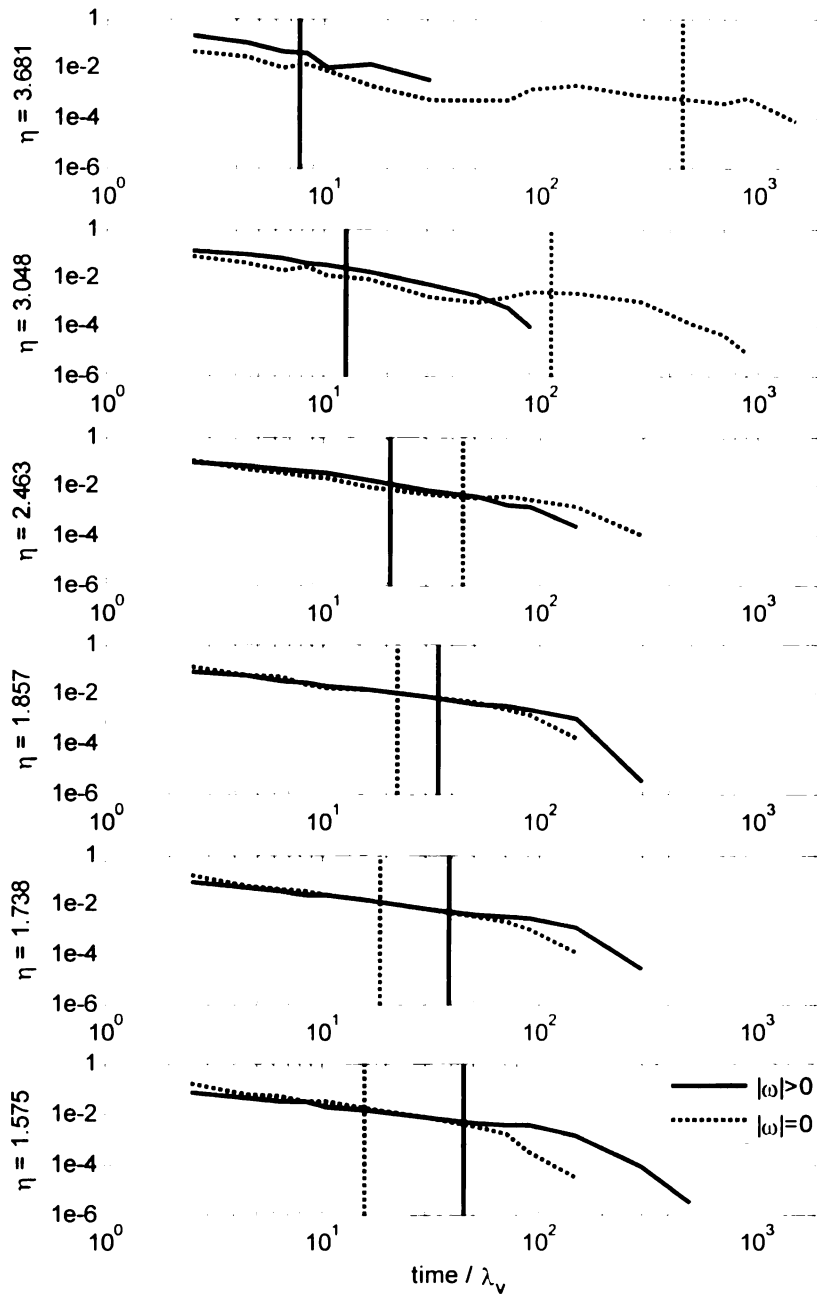
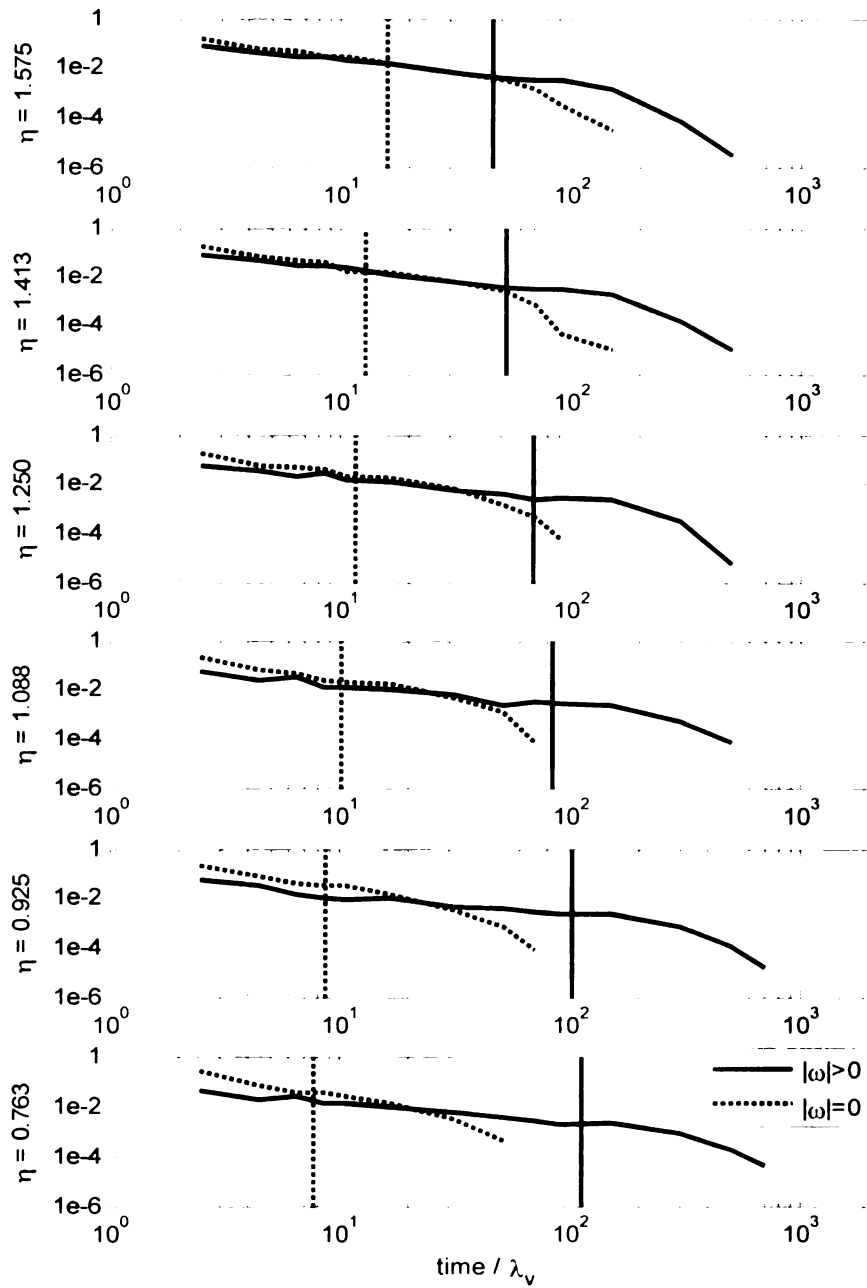


FIGURE 4.2 Illustration of a nascent wedge increasing its positive curvature with respect to the non-vortical fluid.





**FIGURE 4.3** Probability density distribution of conditional duration in time, non-dimensionalized by local Taylor microscale. The vertical lines in each distribution represent the mean value of each distribution.



**FIGURE 4.4** Probability density distribution of conditional duration in time, non-dimensionalized by local Taylor microscale. The vertical lines in each distribution represent the mean value of each distribution. Note that the upper axes of this figure are the same as the lower axes of Figure 4.3.

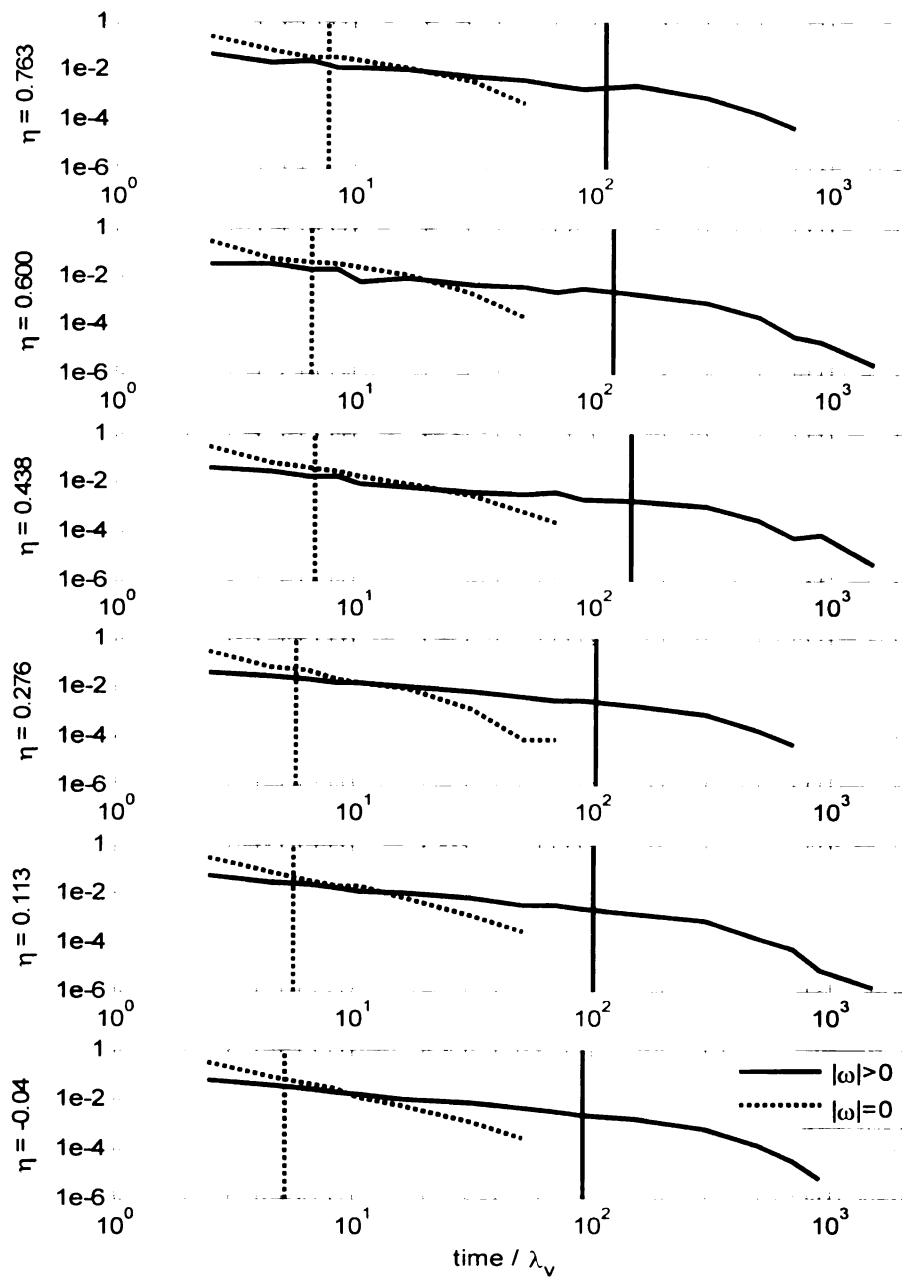


**FIGURE 4.5** Probability density distribution of conditional duration in time, non-dimensionalized by local Taylor microscale. The vertical lines in each distribution represent the mean value of each distribution. Note that the upper axes of this figure are the same as the lower axes of Figure 4.4.

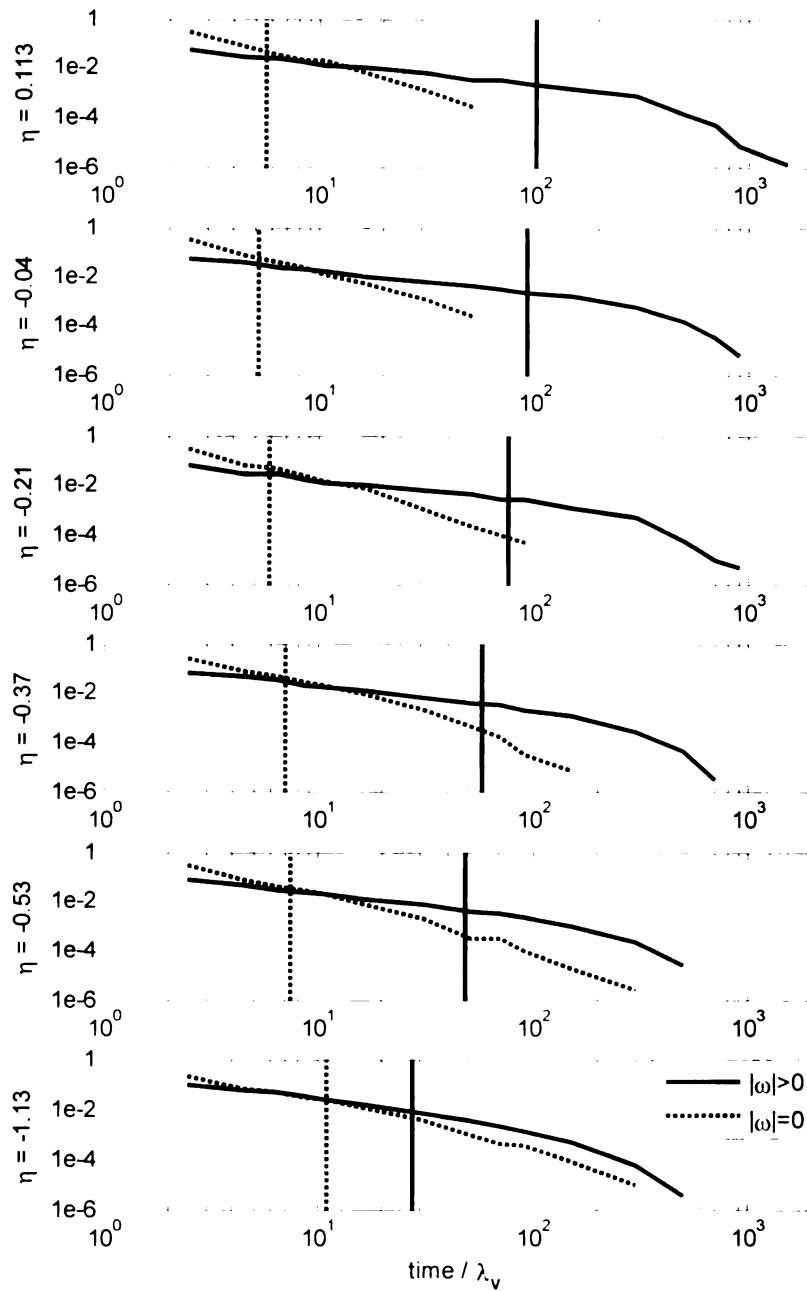
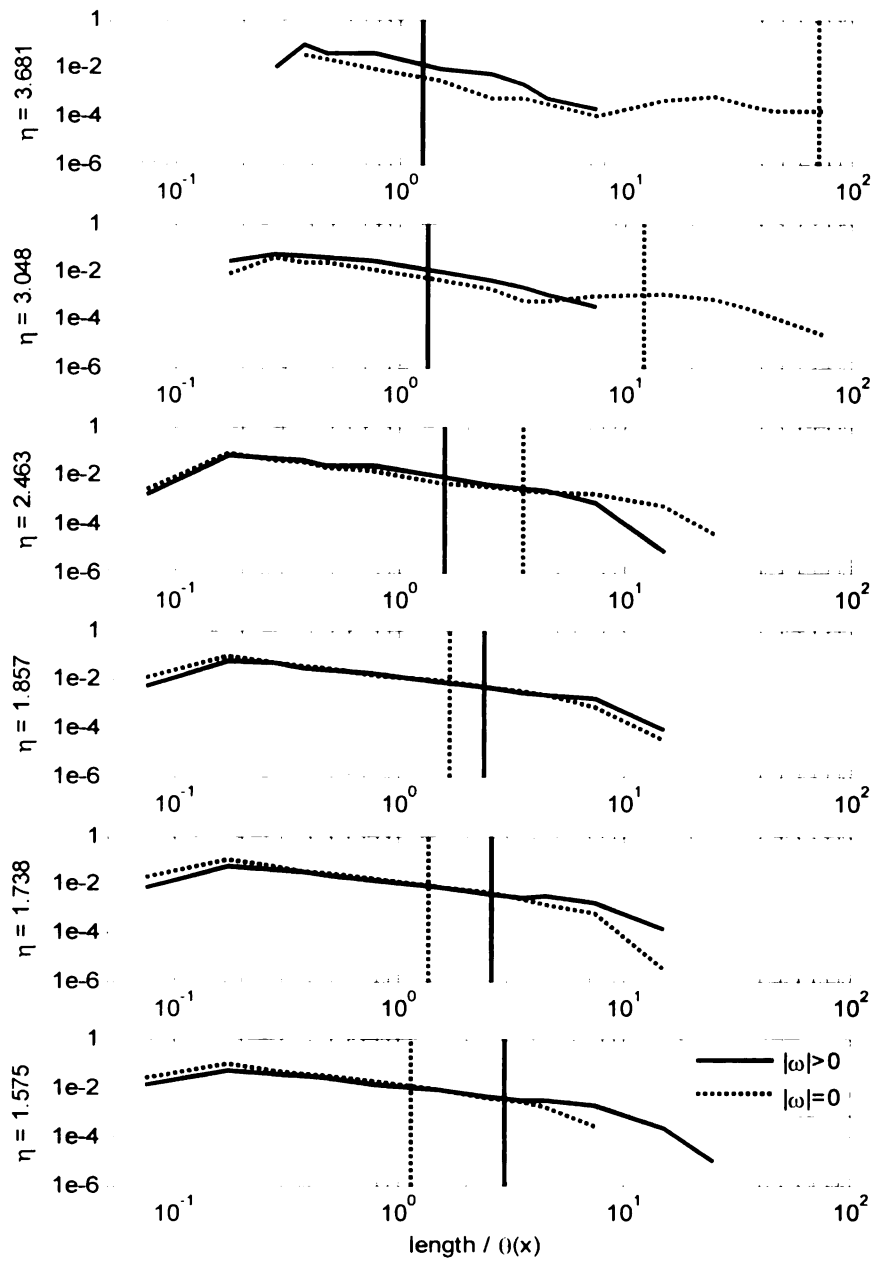
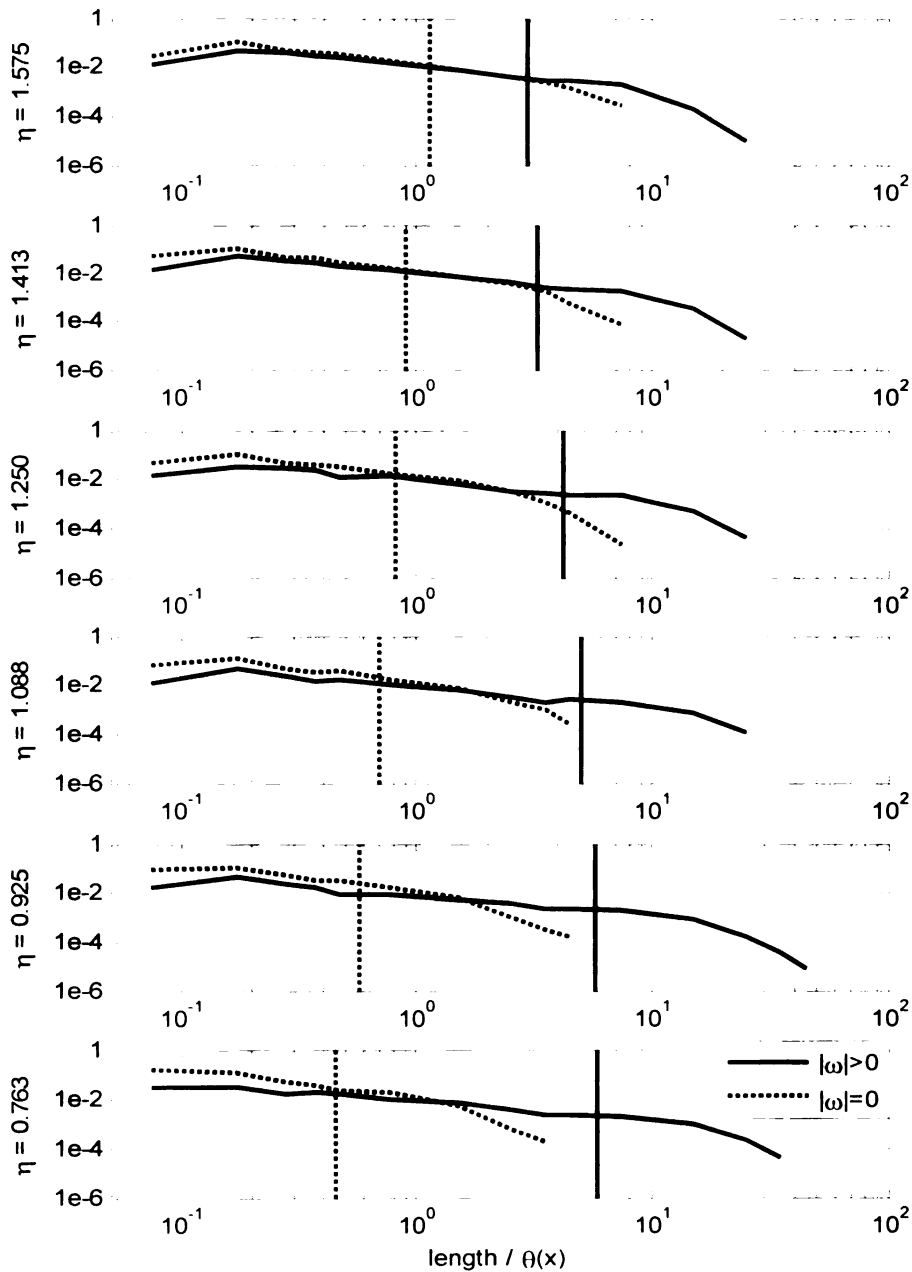


FIGURE 4.6 Probability density distribution of conditional duration in time, non-dimensionalized by local Taylor microscale. The vertical lines in each distribution represent the mean value of each distribution. Note that the upper two axes of this figure are the same as the two lower axes of Figure 4.5.



**FIGURE 4.7** Probability density distribution of conditional duration in length, non-dimensionalized by the momentum thickness (18.47 cm) at streamwise location  $x/\theta_0 = 484$ . The vertical lines in each distribution represent the mean value of each distribution.



**FIGURE 4.8** Probability density distribution of conditional duration in length, non-dimensionalized by the momentum thickness (18.47 cm) at streamwise location  $x/\theta_0 = 484$ . The vertical lines in each distribution represent the mean value of each distribution. Note that the upper axes of this figure are the same as the lower axes of Figure 4.7.

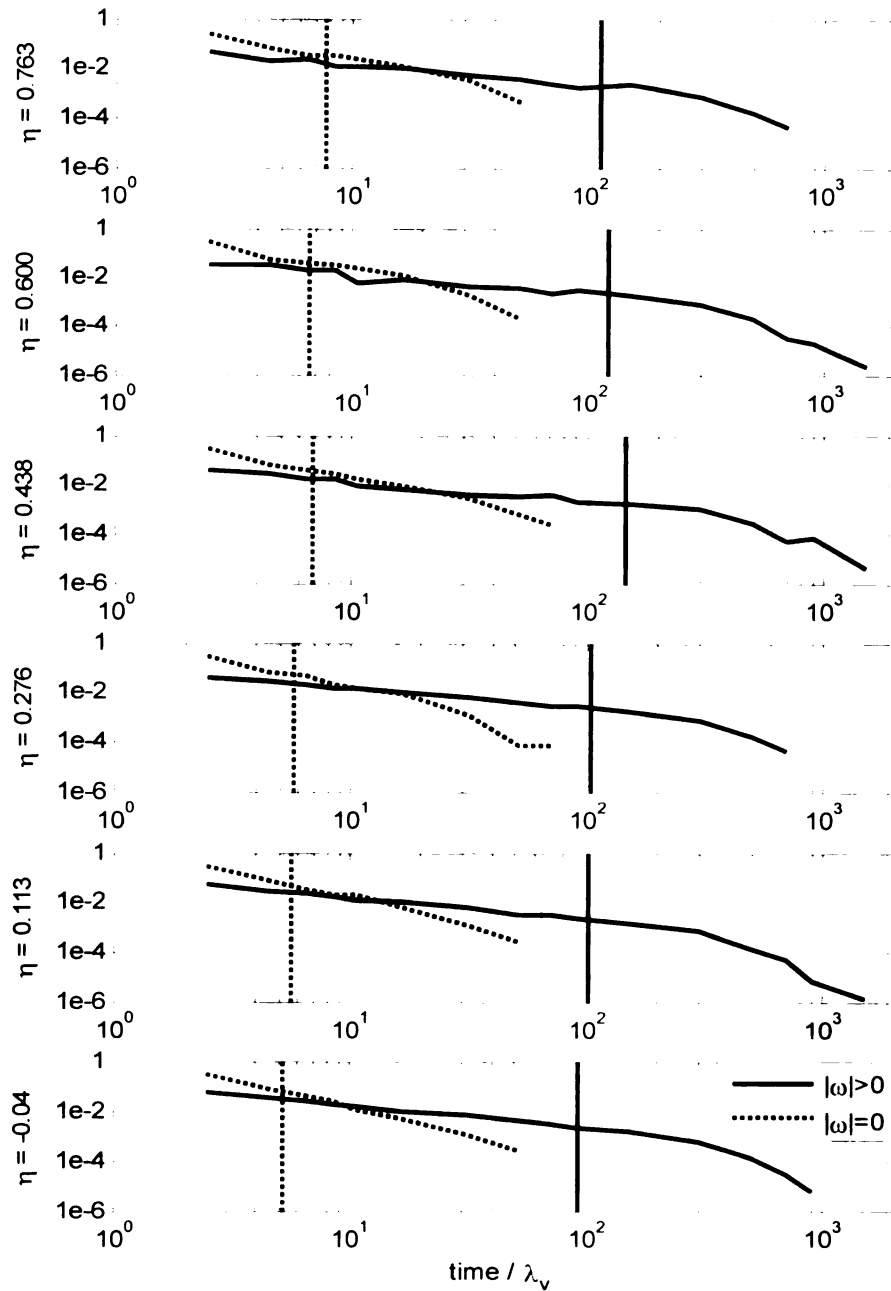


FIGURE 4.9 Probability density distribution of conditional duration in length, non-dimensionalized by the momentum thickness (18.47 cm) at streamwise location  $x/\theta_0 = 484$ . The vertical lines in each distribution represent the mean value of each distribution. Note that the upper axes of this figure are the same as the lower axes of Figure 4.8.

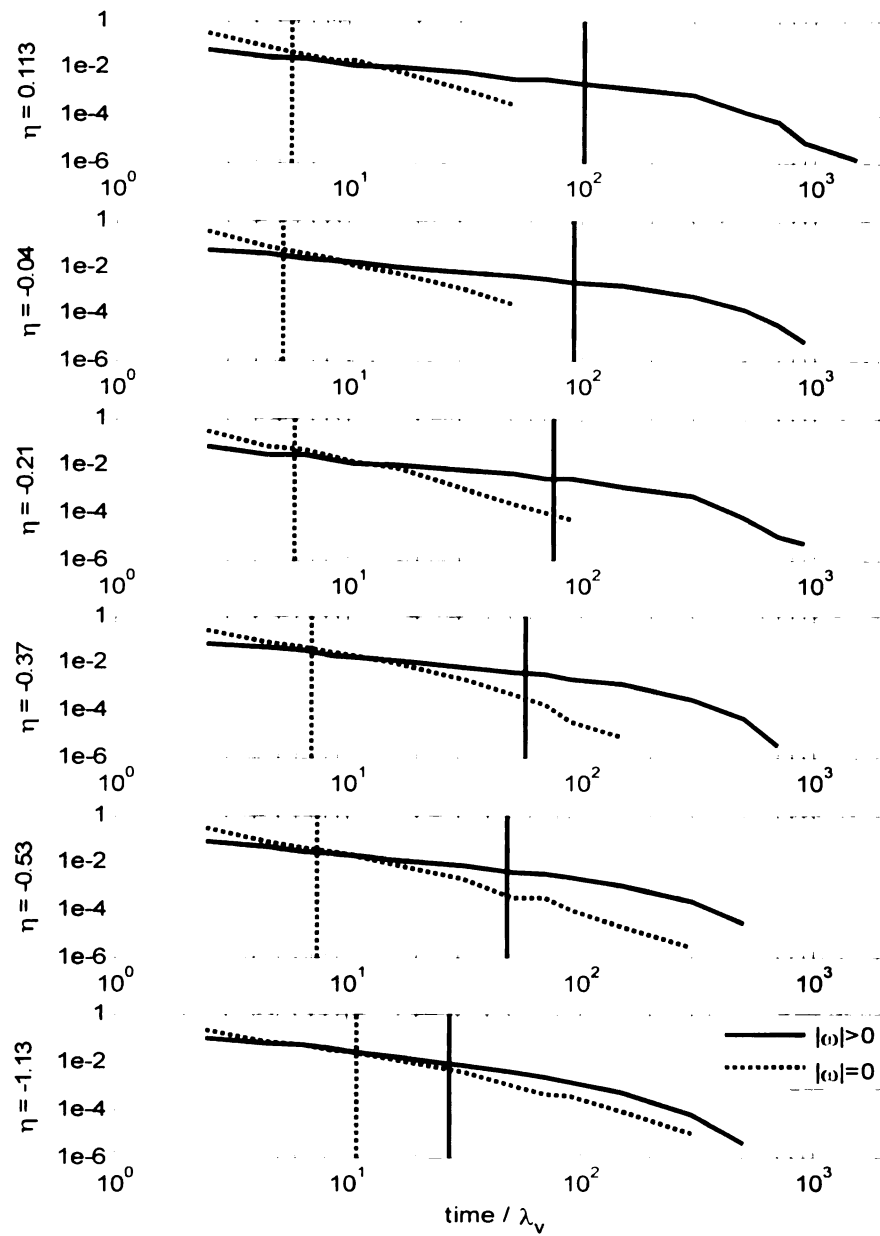


FIGURE 4.10 Probability density distribution of conditional duration in length, non-dimensionalized by the momentum thickness (18.47 cm) at streamwise location  $x/\theta_0 = 484$ . The vertical lines in each distribution represent the mean value of each distribution. Note that the upper two axes of this figure are the same as the lower two axes of Figure 4.9.



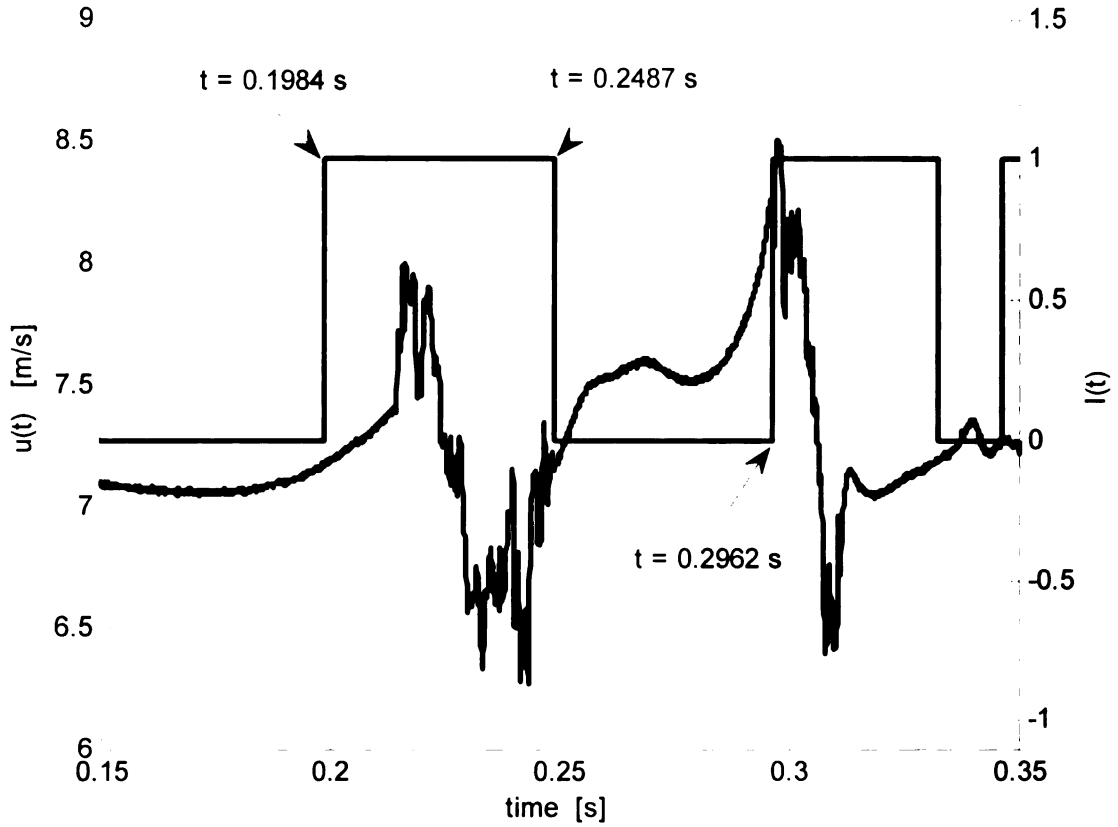


FIGURE 4.11 Sample time series of streamwise component of velocity and intermittency. The measurement location is  $\eta = 2.46$ .

The vortical duration in time represented by the first two marked times is 0.0503 s. The mean streamwise component of velocity during this time is 7.16 m/s. The vortical duration in space during this time is therefore:

$$d_{\omega} = 0.0503 \times 7.16 = 0.358m \quad (4.14)$$

The non-vortical duration in time represented by the second and third marked times is 0.0475 s. The mean streamwise component of velocity during this time is 7.57 m/s. The non-vortical duration in space during this time is therefore:

$$d_{n-\omega} = 0.0475 \times 7.57 = 0.363m \quad (4.15)$$

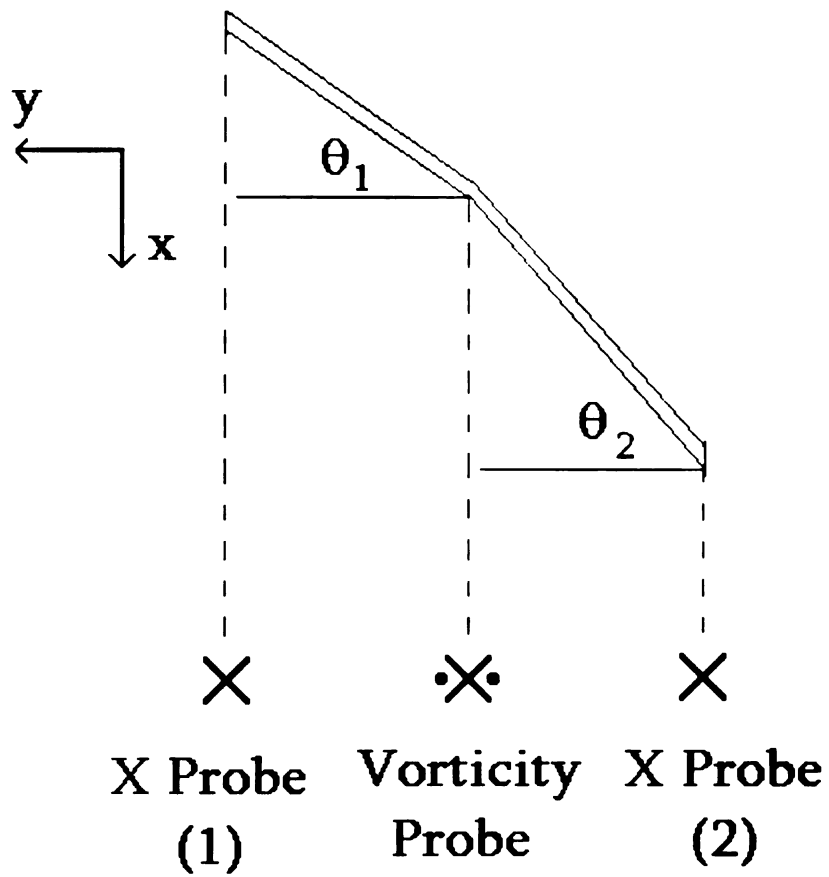


FIGURE 4.12 Illustration of the rake of probes used to measure the angle of the VSL relative to the transverse direction. The front angle is given by  $(\theta_1 + \theta_2)/2$ .

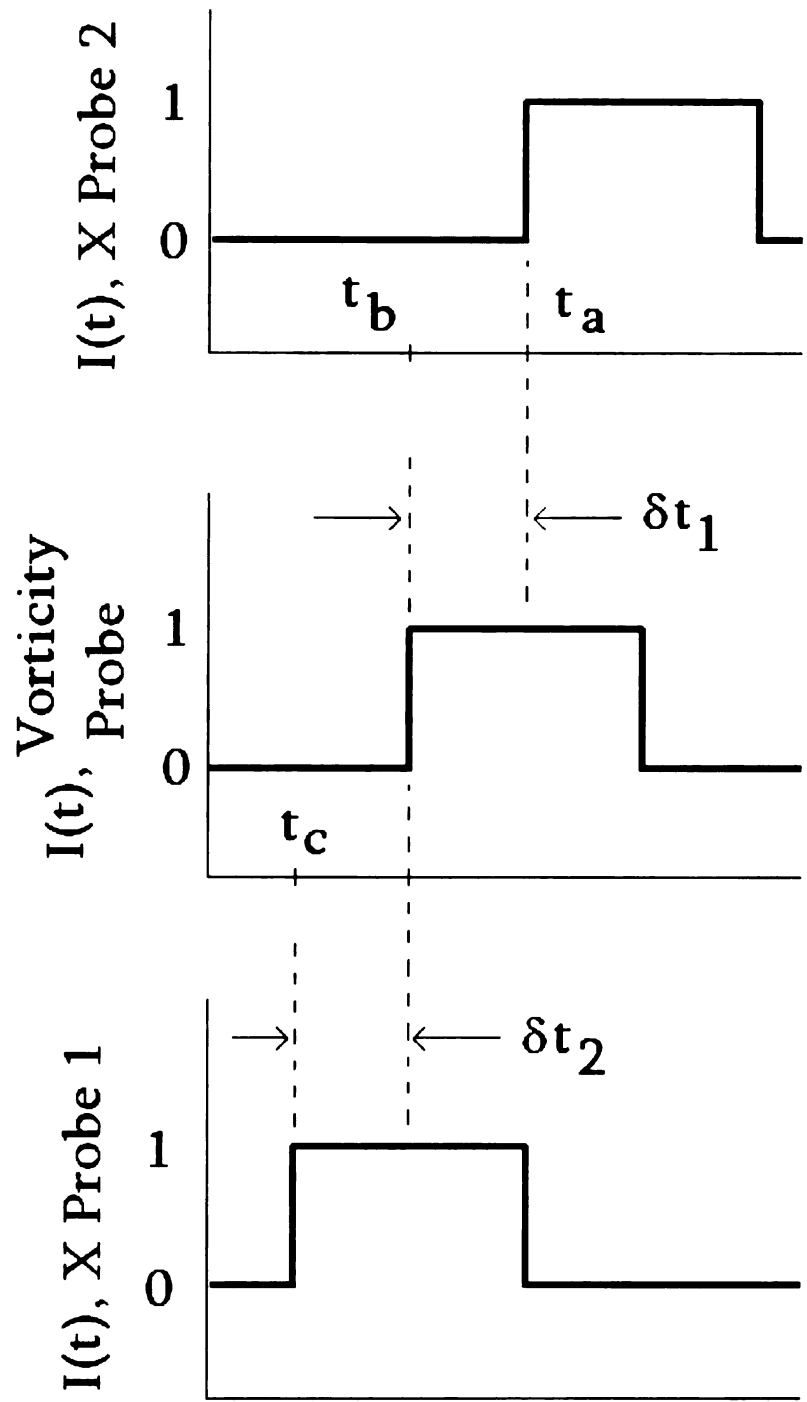
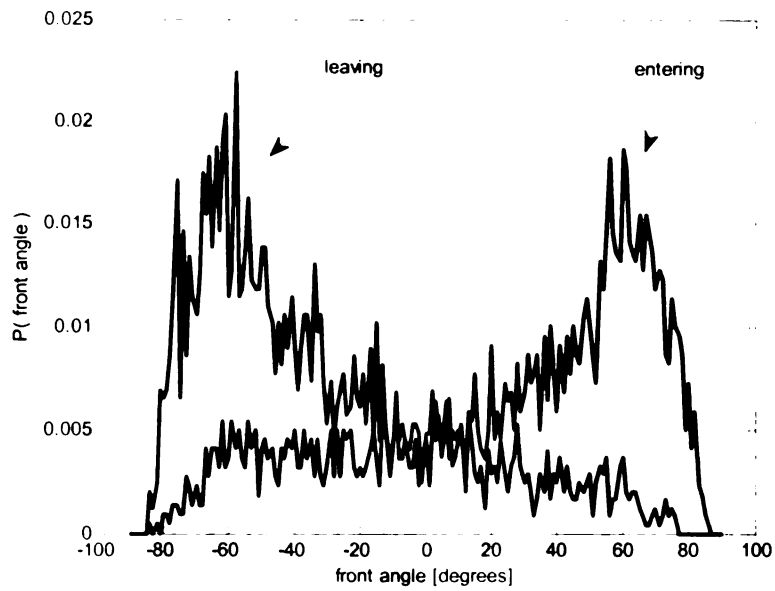
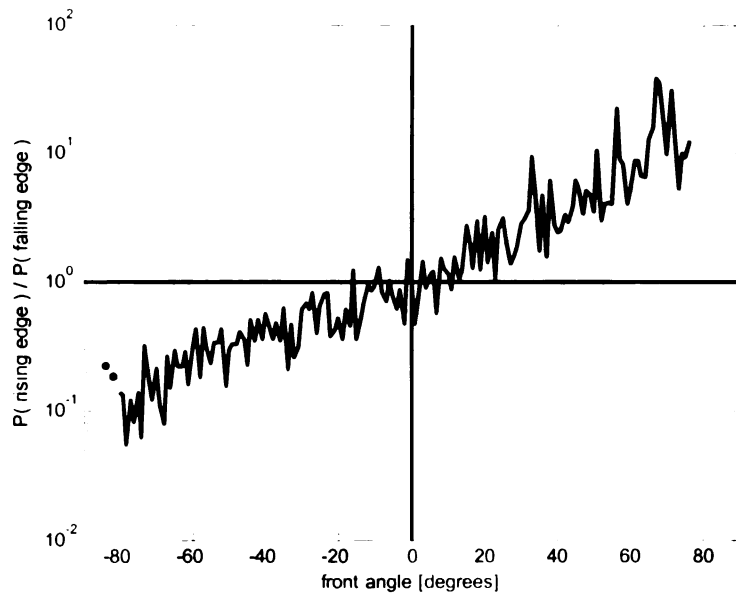


FIGURE 4.13 Timing scheme used in the algorithm to compute front angle. The pattern shown would be viewed as an “entering” edge.



**FIGURE 4.14 Probability density distribution of VSL angle for both entering (vortical to non-vortical) and leaving (non-vortical to vortical) conditions.**



**FIGURE 4.15 Ratio of probabilities,  $P(\text{entering})/P(\text{leaving})$ .**

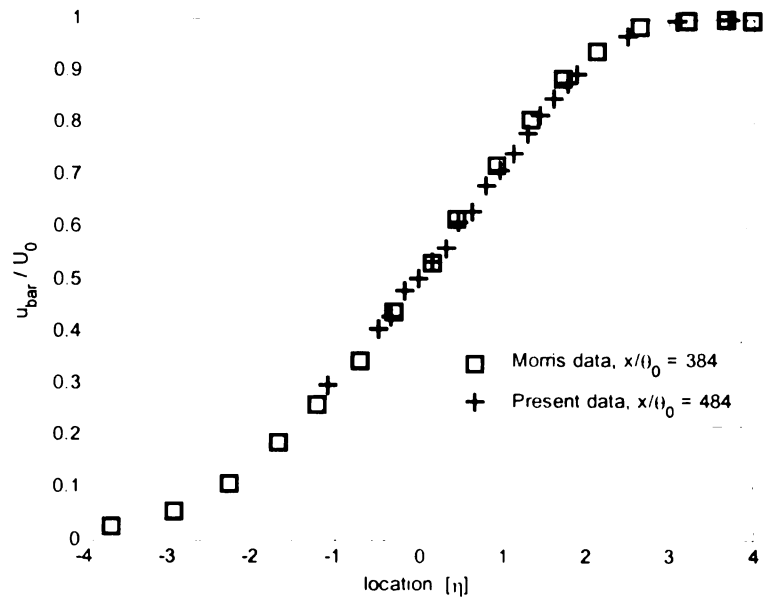


FIGURE 4.16 Mean value, streamwise component of velocity. Data from Morris (2002) are shown for comparison.

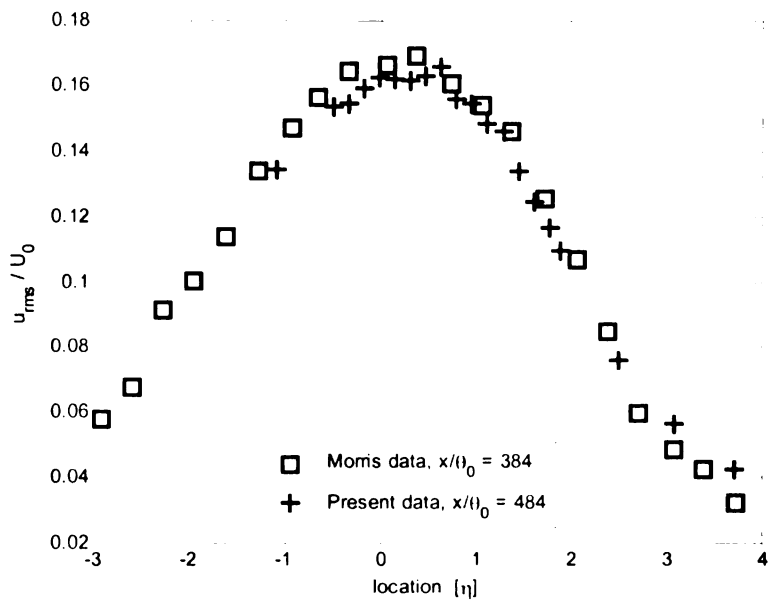


FIGURE 4.17 Standard deviation, streamwise component of velocity, Data from Morris (2002) are shown for comparison.

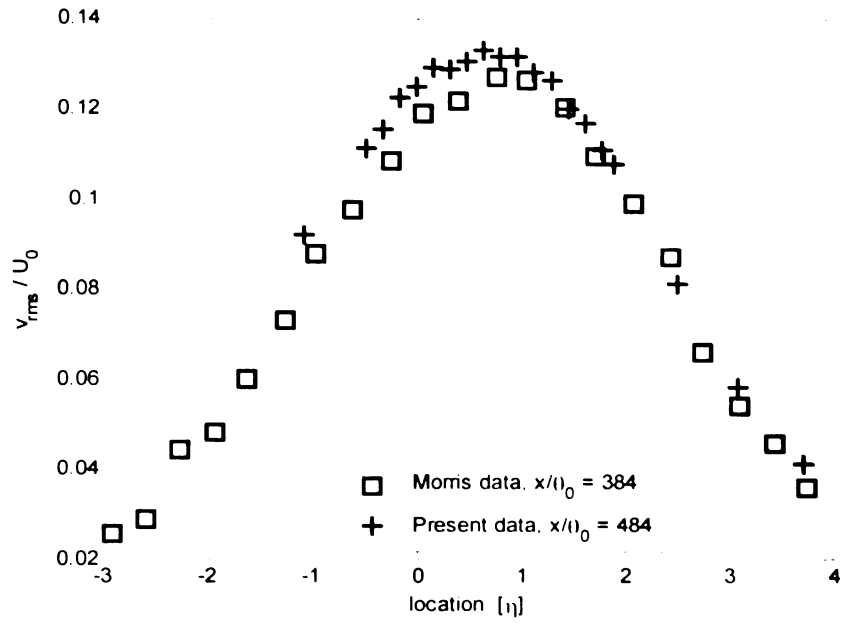


FIGURE 4.18 Standard deviation, transverse component of velocity. Data from Morris (2002) are shown for comparison.

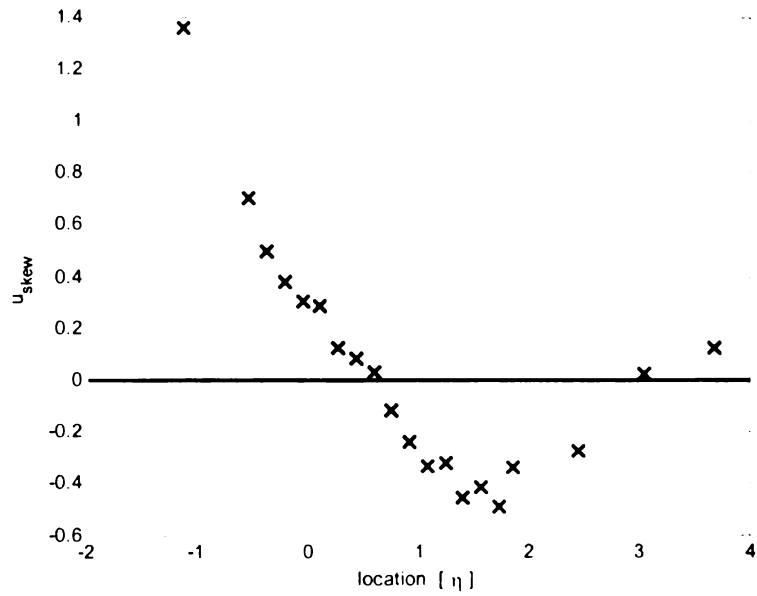


FIGURE 4.19 Skewness, streamwise component of velocity.

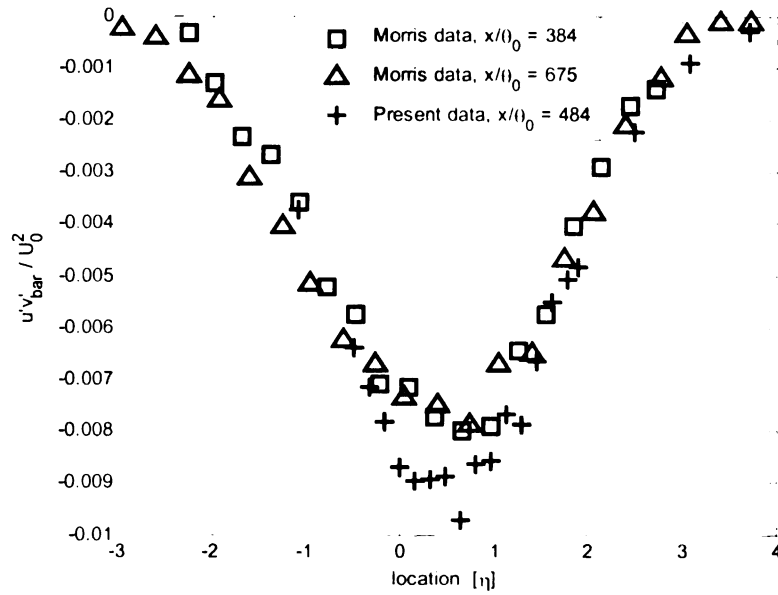


FIGURE 4.20 Reynolds stress non-dimensionalized by square of free stream velocity. Data from Morris (2002) are shown for comparison.

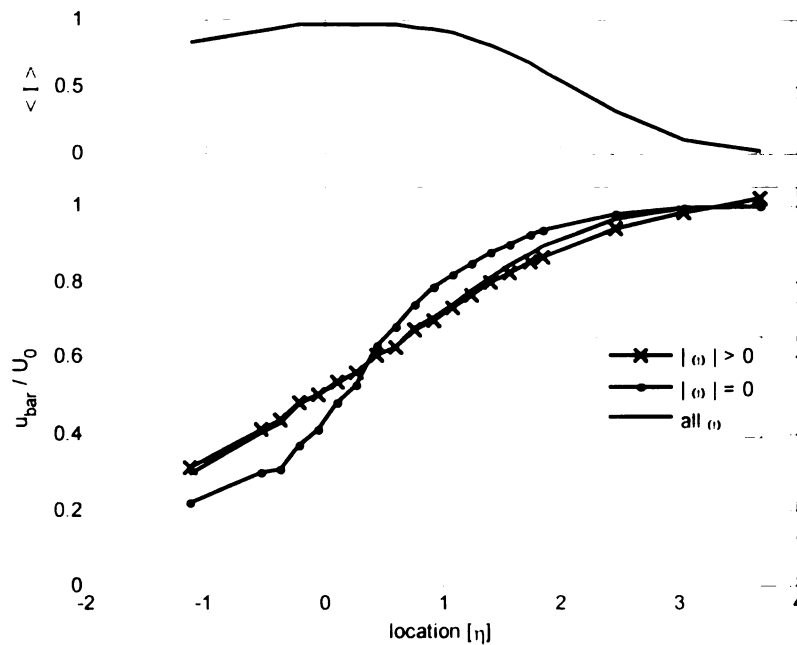


FIGURE 4.21 Mean value, streamwise component of velocity. Vortical, non-vortical and unconditional values. (The mean value of intermittency is presented on the upper axis for reference.)

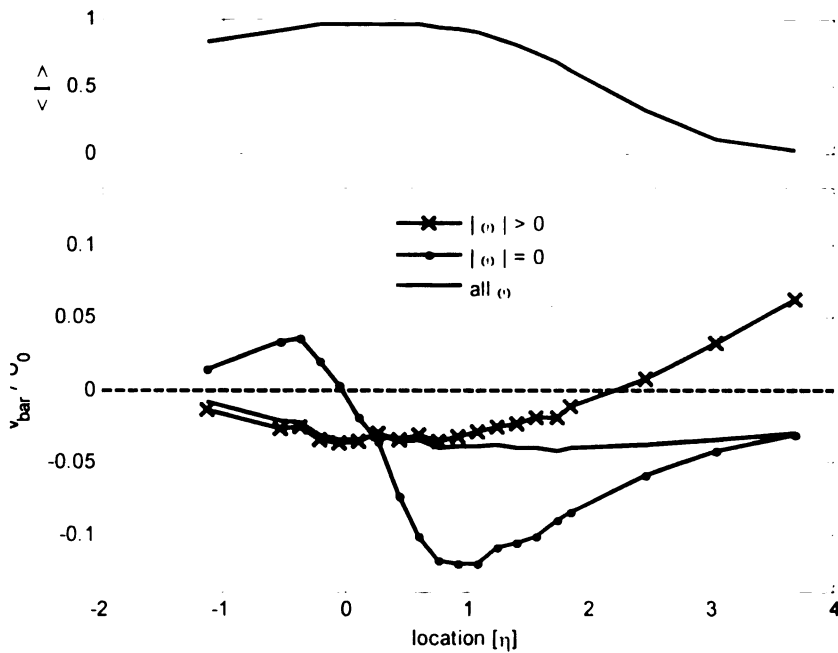


FIGURE 4.22 Mean value, transverse component of velocity. Vortical, non-vortical and unconditional values. (The mean value of intermittency is presented on the upper axis for reference.)

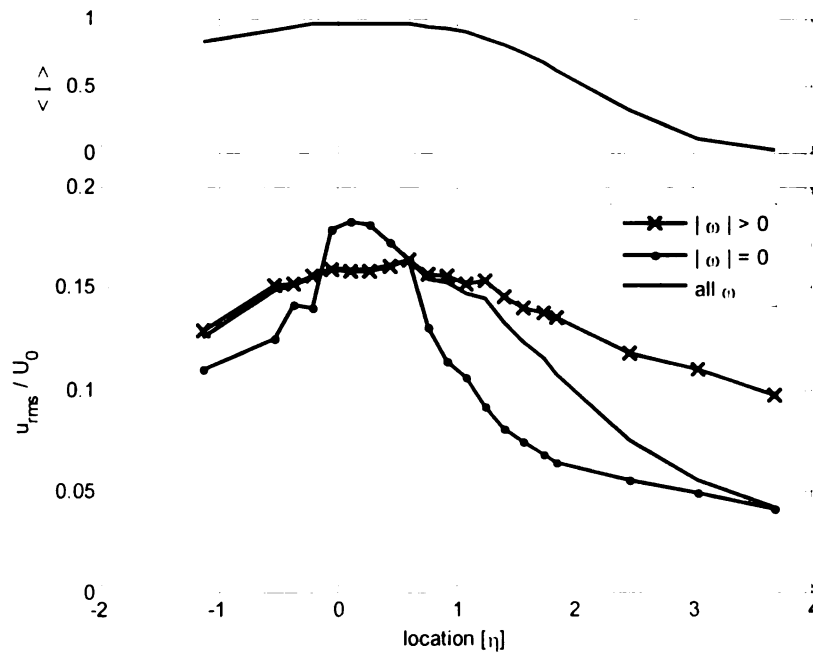
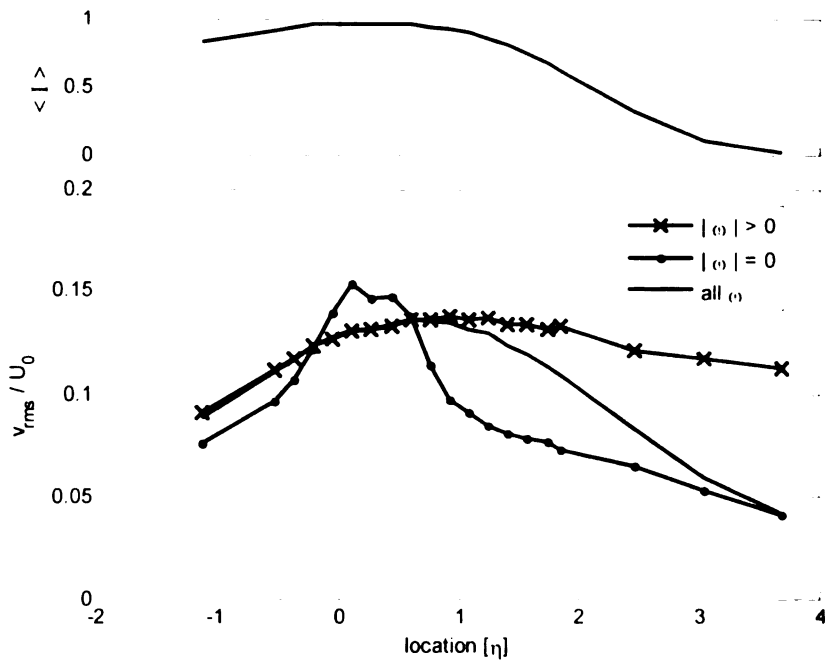


FIGURE 4.23 Standard deviation, streamwise component of velocity. Vortical, non-vortical and unconditional values. (The mean value of intermittency is presented on the upper axis for reference.)





**FIGURE 4.24** Standard deviation, transverse component of velocity. Vortical, non-vortical and unconditional values. (The mean value of intermittency is presented on the upper axis for reference.)

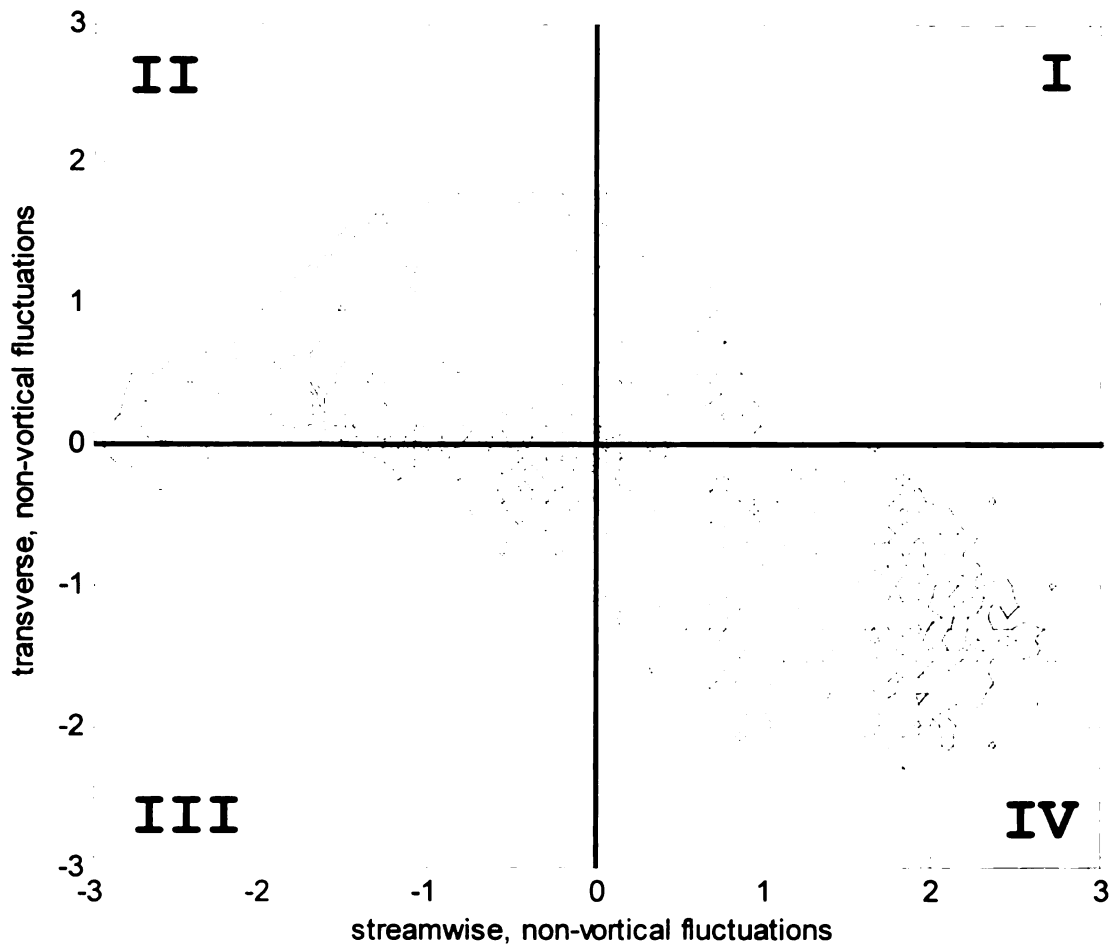


FIGURE 4.25 Joint probability density distribution of fluctuating, non-vortical streamwise and transverse components of velocity at  $\eta = 0.05$ . Note that the solid black lines represent the *unconditioned* mean of streamwise and transverse velocity.

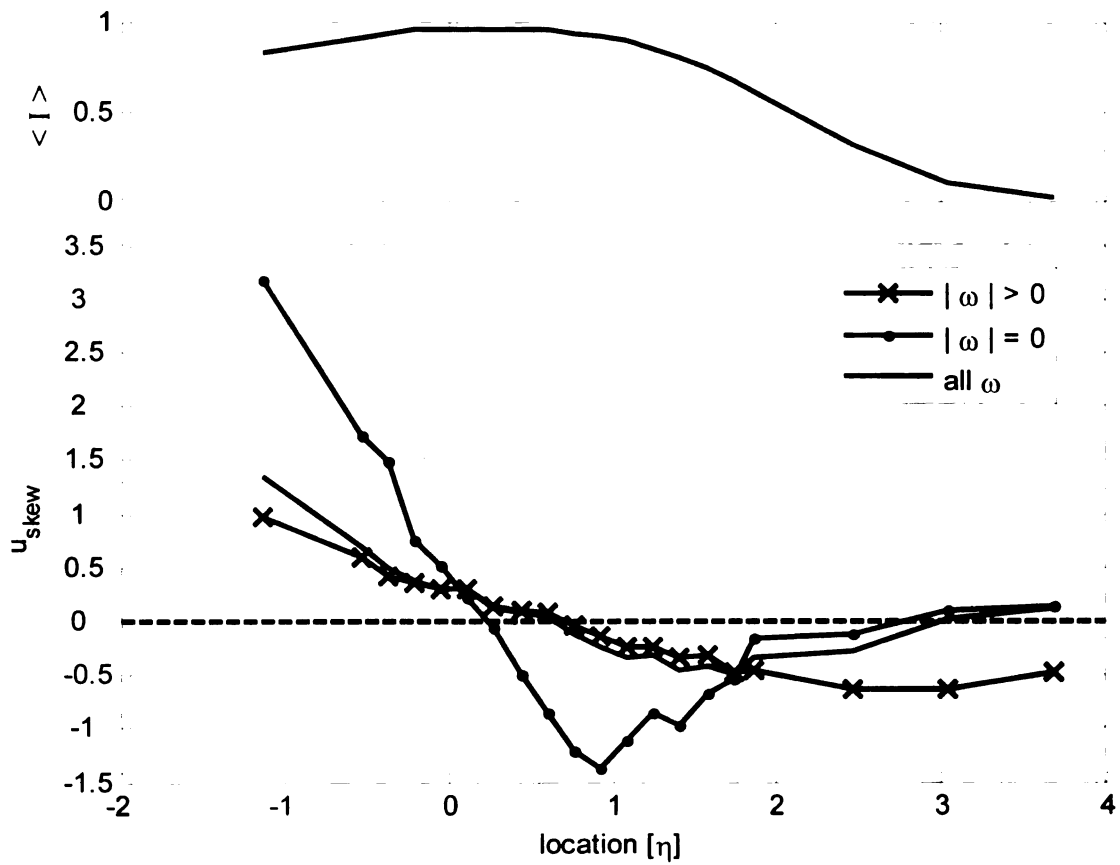
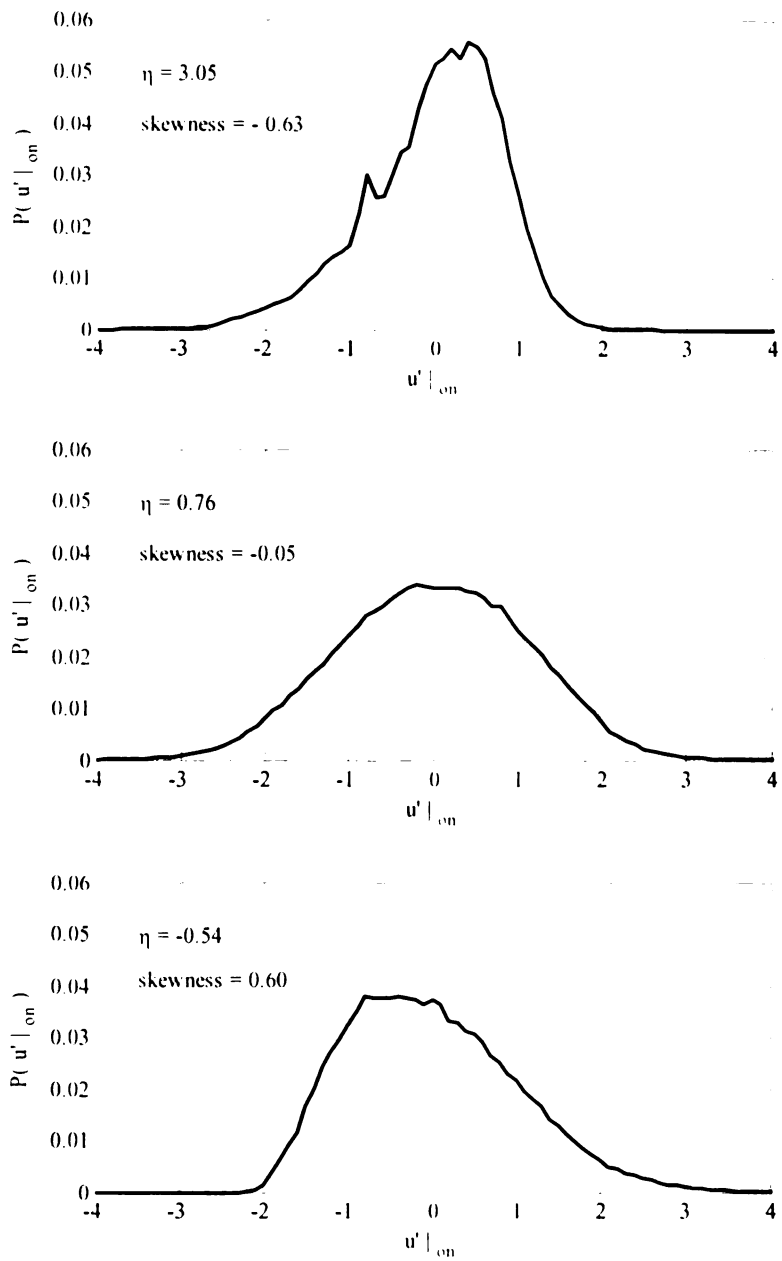


FIGURE 4.26 Skewness, streamwise component of velocity. Vortical, non-vortical and unconditional values. (The mean value of intermittency is presented on the upper axis for reference.)



**FIGURE 4.27** Probability density distributions of streamwise component of velocity, vortical condition, at three transverse locations

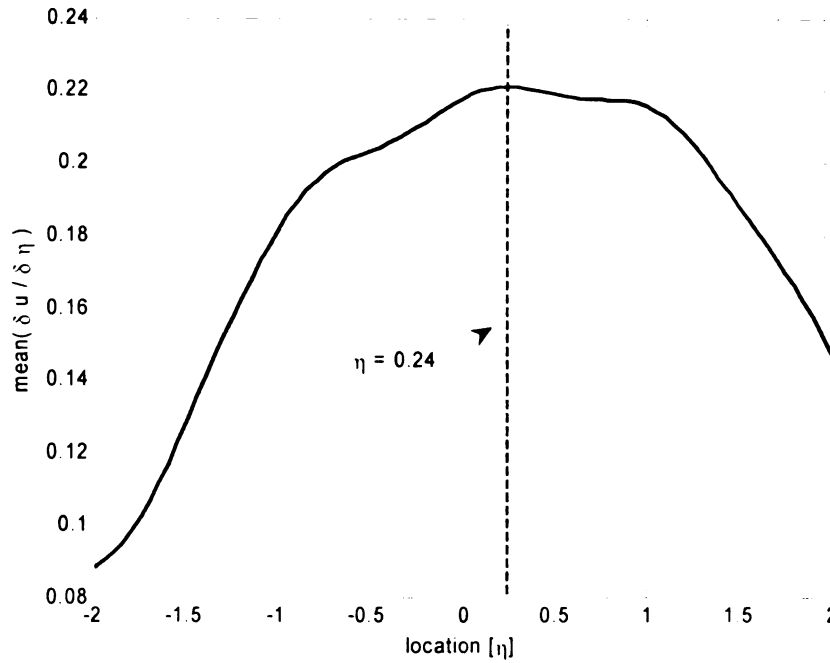


FIGURE 4.28 Mean shear across the shear layer. The derivative was computed by fitting the  $x/\theta_0 = 484$  streamwise velocity values with a piecewise polynomial spline, then differentiating that spline.

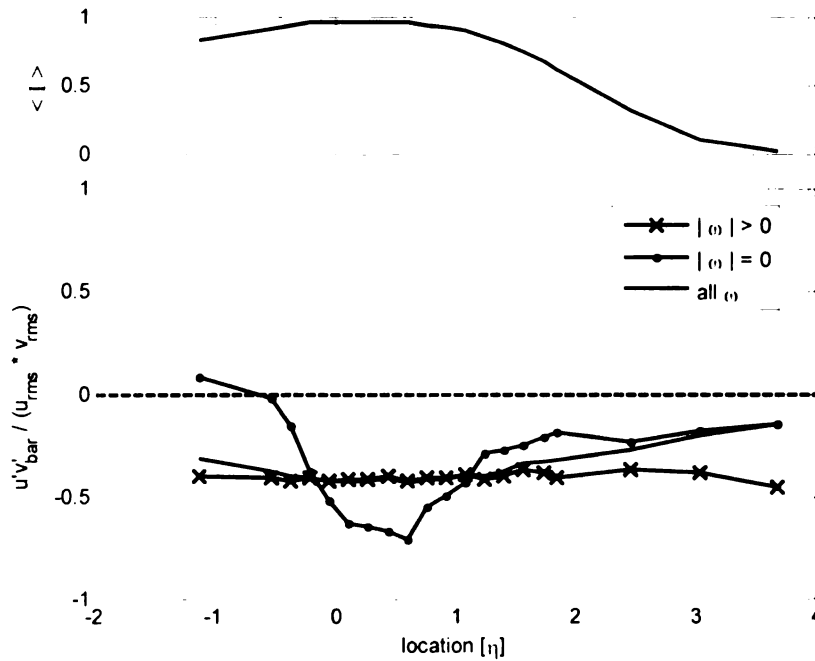


FIGURE 4.29 Reynolds stress divided by the product of standard deviations, also called the correlation coefficient ( $\overline{u'v'}/(\tilde{u}\tilde{v})$ ). Vortical, non-vortical and unconditional values. (The mean value of intermittency is presented on the upper axis for reference.)

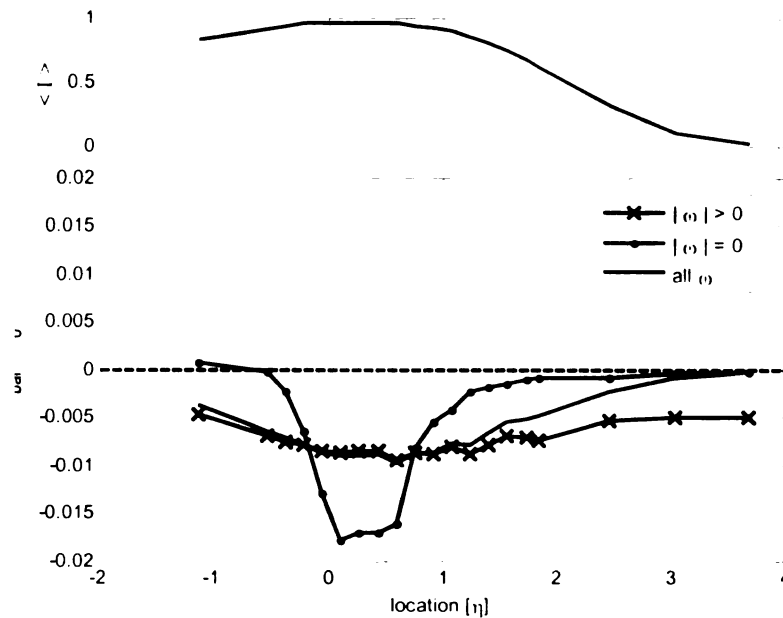


FIGURE 4.30 The Reynolds stress non-dimensionalized by the square of free-stream velocity ( $\overline{u'v'}/U_0^2$ ). Vortical, non-vortical and unconditional values. (The mean value of intermittency is presented on the upper axis for reference.)

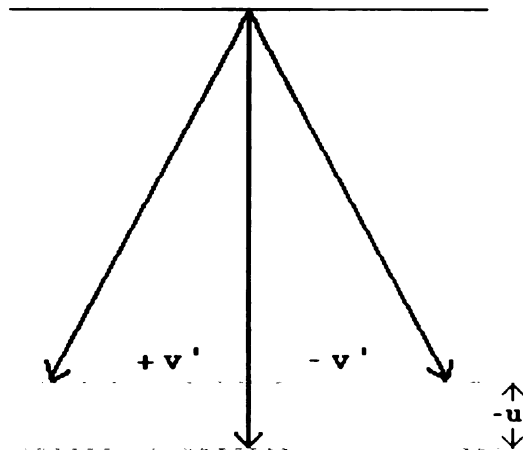


FIGURE 4.31 Model of non-vortical velocity fluctuations near the free stream--discredited by Figure 4.29's communication of distinctly non-zero correlation coefficient in non-vortical velocity near the free stream. In this model, negative streamwise fluctuations would have been equally associated with both positive and negative transverse fluctuations.

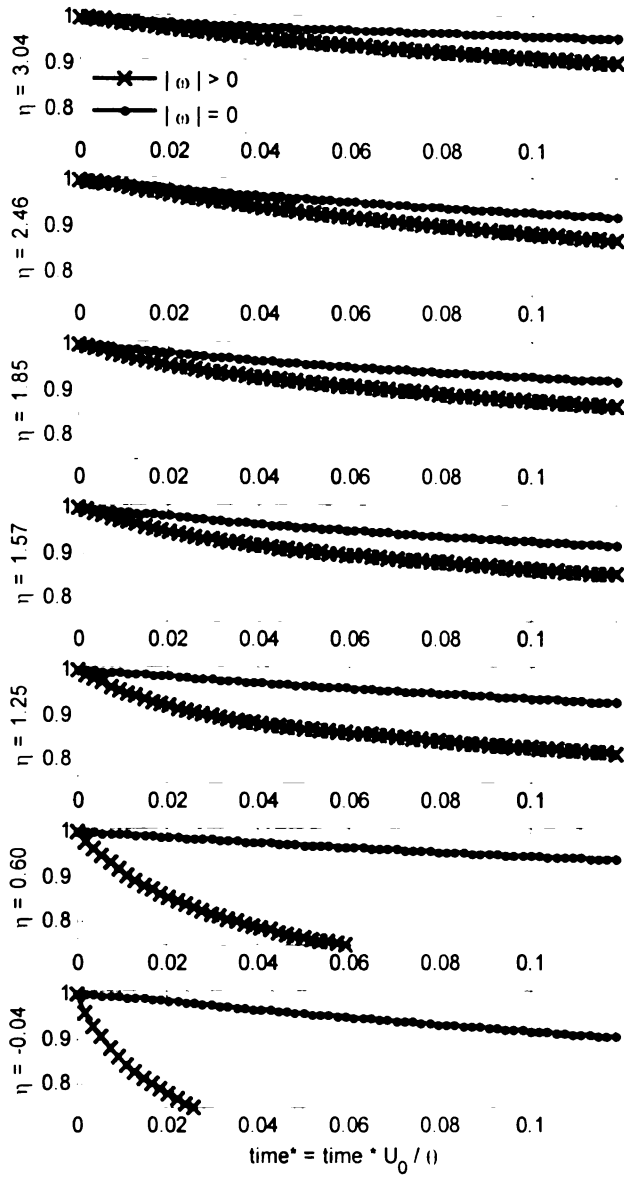


FIGURE 4.32 Conditional Autocorrelation of streamwise velocity component at seven positions on the high-speed side of the shear layer.

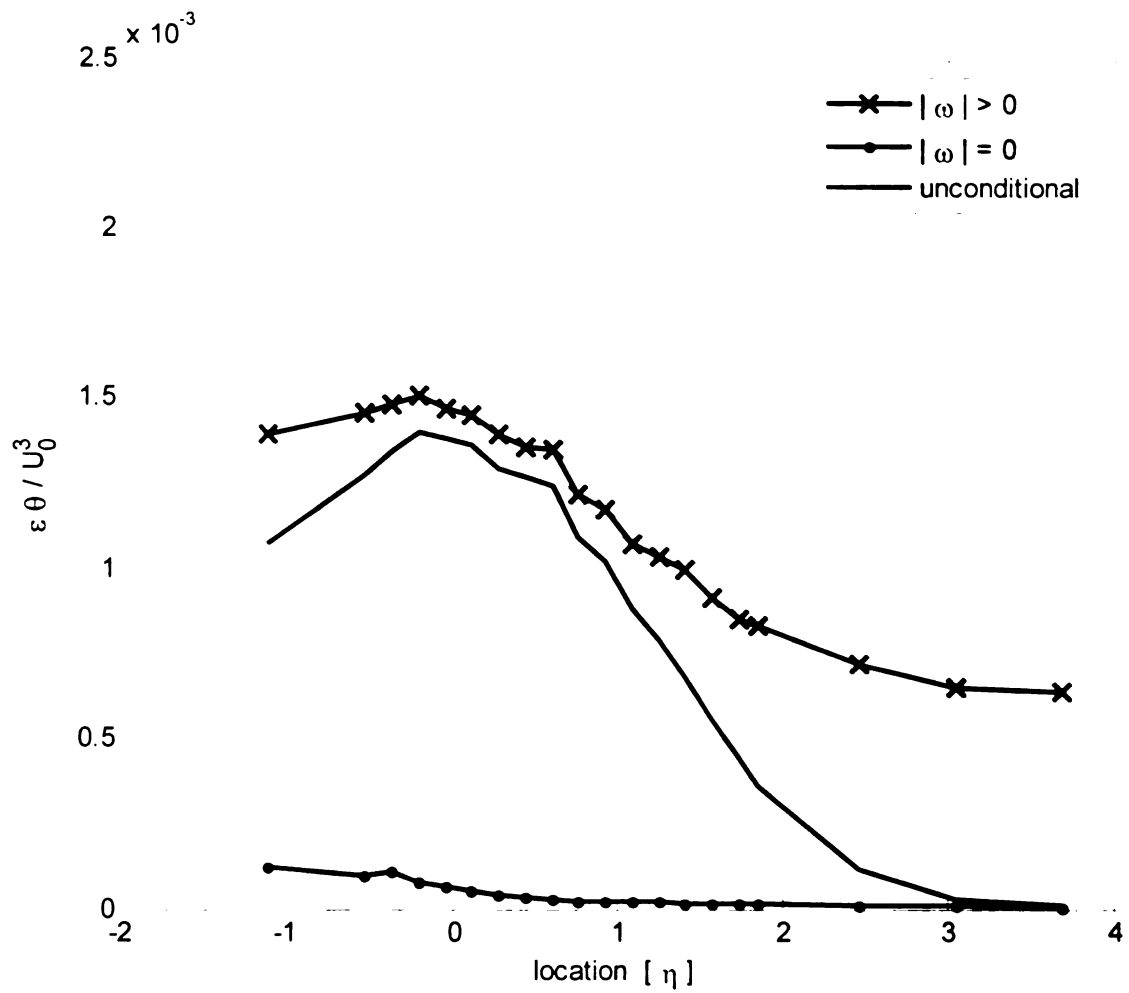


FIGURE 4.33 Dissipation, non-dimensionalized. Vortical, non-vortical, and unconditioned values. The equation defining the approximation of  $\varepsilon$  shown is Equation 4.13.



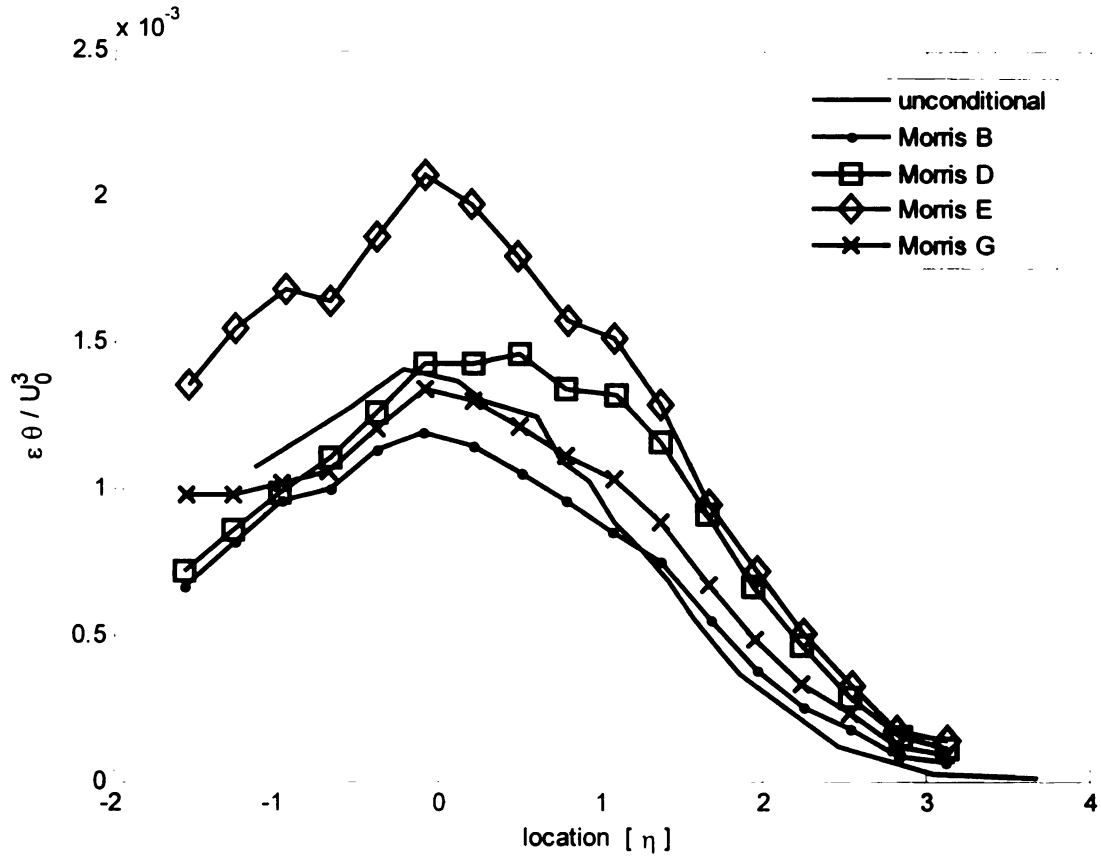


FIGURE 4.34 Unconditional dissipation, compared to values computed in Morris (2002).

Morris B is an isotropic measure:

$$\epsilon_{isotropy} = 15\nu \frac{\overline{u'^2}}{\lambda_v^2} \quad (4.16)$$

Morris D, E, and G are all “semi-isotropic”:

$$\epsilon_D = \nu \left[ \frac{5}{3} \overline{\left(\frac{\partial u}{\partial x}\right)^2} + 2 \overline{\left(\frac{\partial u}{\partial z}\right)^2} + \frac{8}{3} \overline{\left(\frac{\partial v}{\partial z}\right)^2} + 2 \overline{\left(\frac{\partial v}{\partial x}\right)^2} \right] \quad (4.17)$$

$$\epsilon_E = 3\nu \left[ \overline{\left(\frac{\partial u}{\partial x}\right)^2} + 2 \overline{\left(\frac{\partial u}{\partial y}\right)^2} + \overline{\left(\frac{\partial u}{\partial z}\right)^2} \right] \quad (4.18)$$

$$\epsilon_G = \nu \left[ \overline{\left(\frac{\partial u}{\partial x}\right)^2} + \overline{\left(\frac{\partial u}{\partial y}\right)^2} + \overline{\left(\frac{\partial u}{\partial z}\right)^2} + \overline{\left(\frac{\partial w}{\partial z}\right)^2} + 5 \overline{\left(\frac{\partial w}{\partial x}\right)^2} \right] \quad (4.19)$$

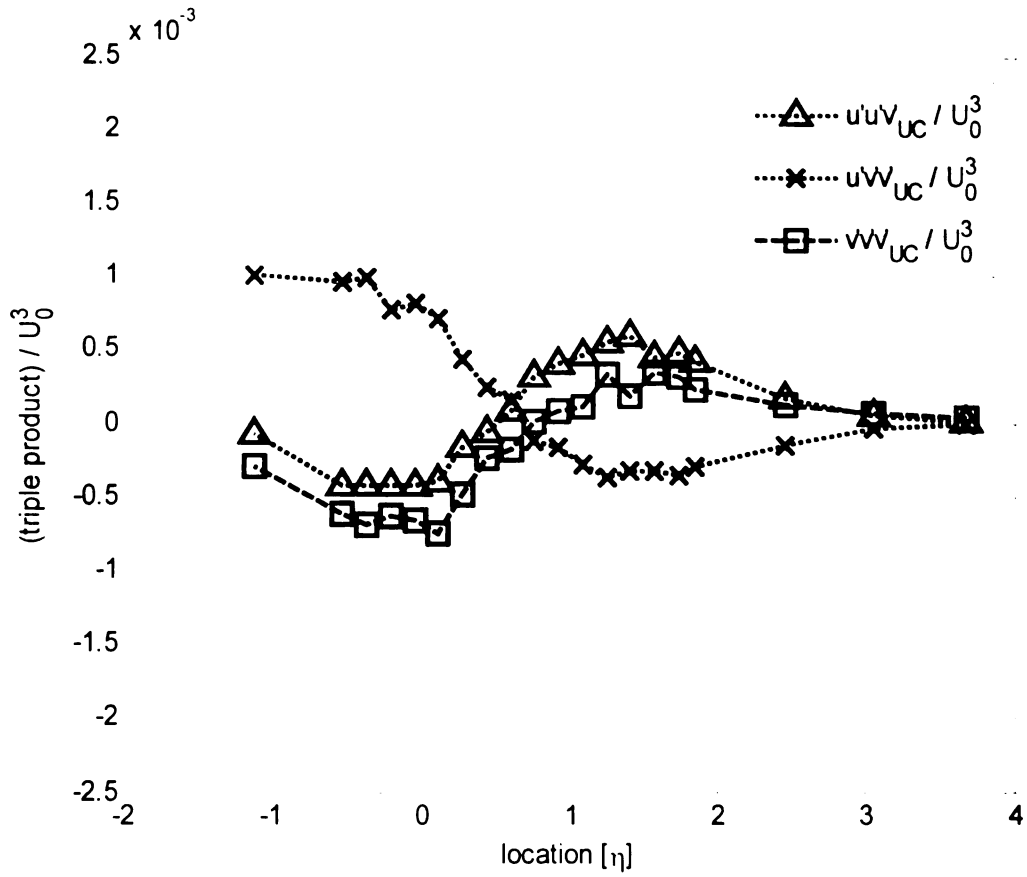


FIGURE 4.35 Triple products of fluctuating velocity, non-dimensionalized by cube of free-stream velocity, unconditioned

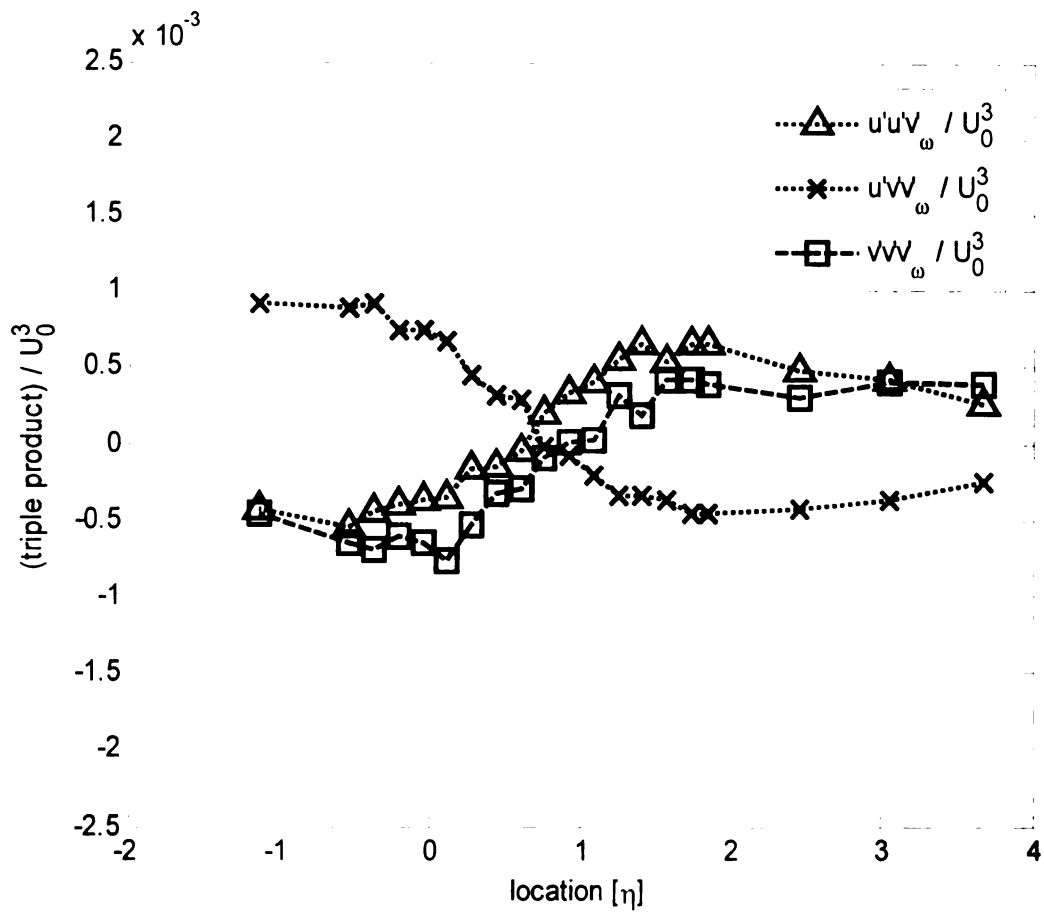


FIGURE 4.36 Triple products of fluctuating velocity, non-dimensionalized by cube of free-stream velocity, vortical

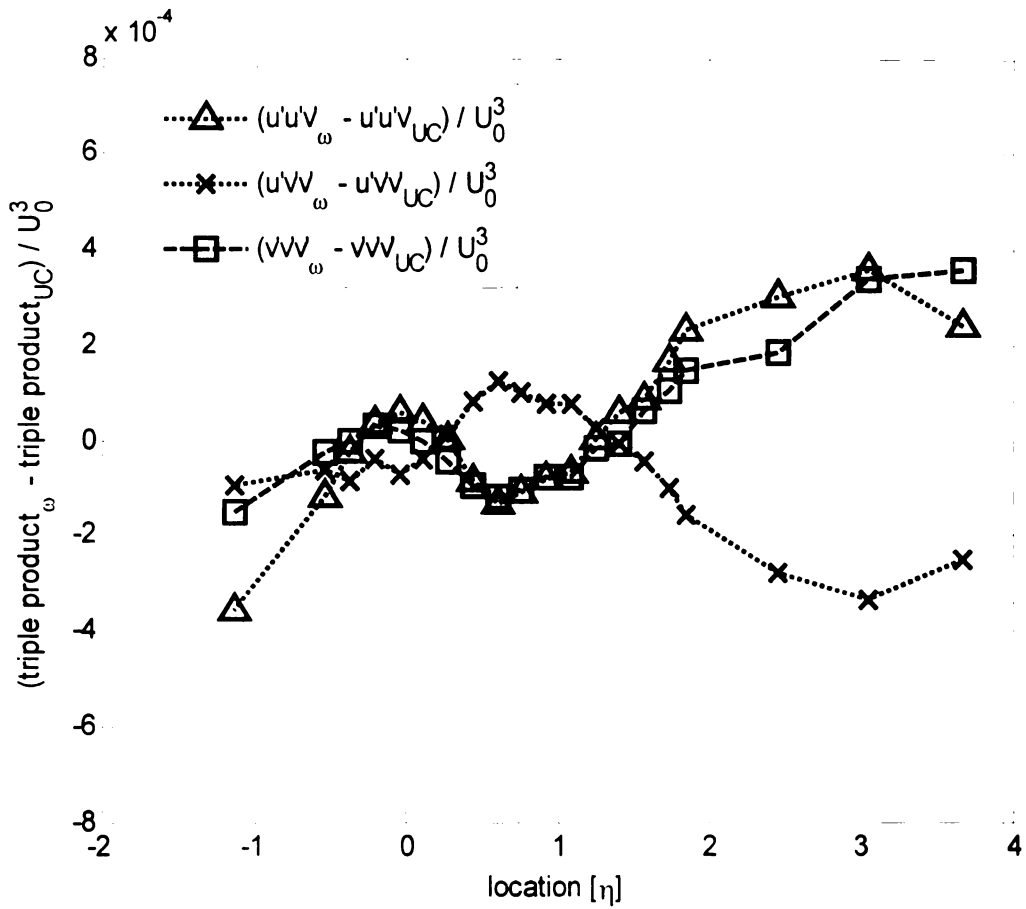
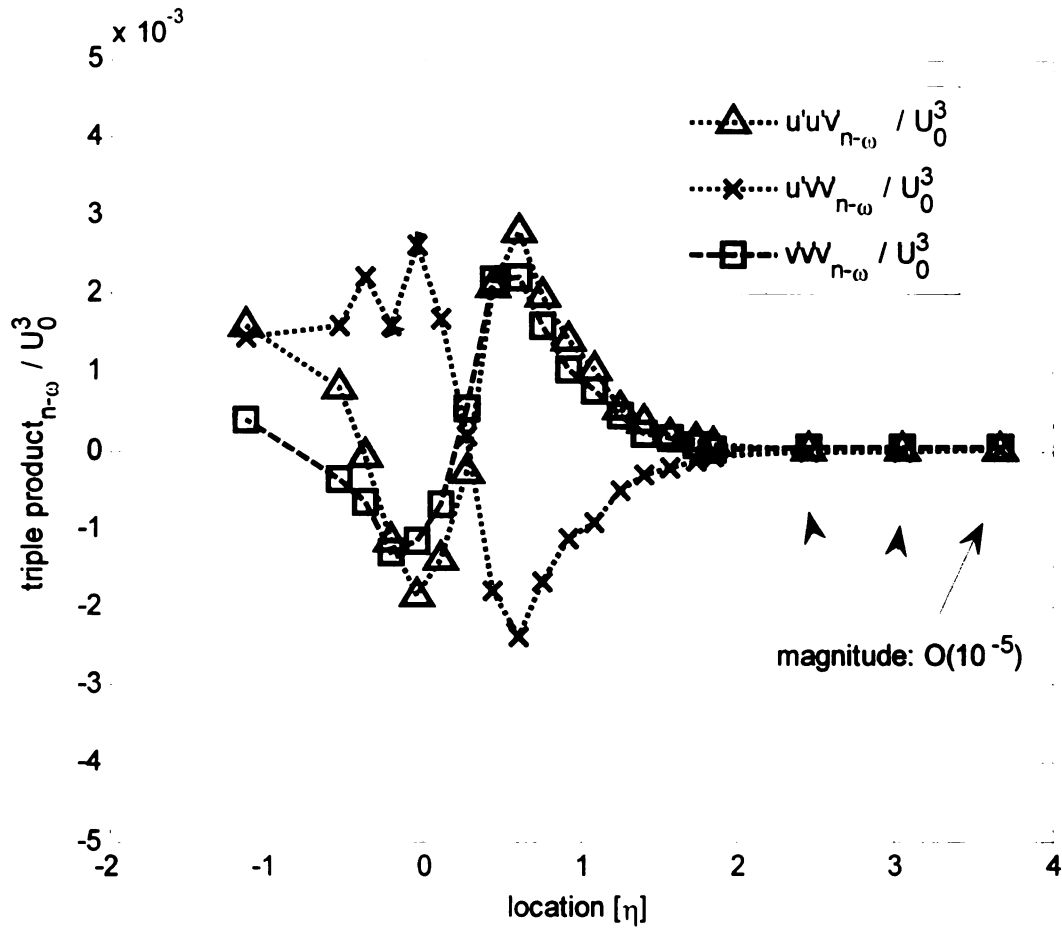


FIGURE 4.37 Difference between vortical and unconditioned triple velocity products.



**FIGURE 4.38** Triple products of fluctuating velocity, non-dimensionalized by cube of free-stream velocity, non-vortical. (Note that the ordinate has twice the range of Figs. 4.35 and 4.36.)

## REFERENCES

1. Abdel-Rahman, A., Tropea, C., Slawson, P., and Strong A., (1987) "On temperature compensation in hot-wire anemometry", *Journal of Physics, E: Sci. Instrum.*, Vol 20, pp. 315-319.
2. Bendat, J.S and Piersol, A.G., (1986). Random Data: Analysis and Measurement Procedures. Second Edition. John Wiley and Sons.
3. Bernard, P.S. and Wallace, J.M. (2002). Turbulent Flow. John Wiley and Sons.
4. Brown, L.W..B., Antonia, R.A., and Chua, L.P. (1989) "Calibration of X-Probes for Turbulent Flow Measurement". *Experiments in Fluids*, Vol. 7, pp. 201-208.
5. Bruun, H.H. (1995). Hot-wire Anemometry Principles and Signal Analysis. Oxford University Press.
6. Corrsin, S. (1943) "Investigation of flow in an axially symmetrical heated jet of air." NACA WR W-94, NACA, Washington D.C.
7. Corrsin, S., and Kistler, A.L.(1955). "Free-Stream Boundaries of Turbulent Flows". National Advisory Committee for Aeronautics, Report 1244.
8. Foss, J.F, Bohl, D.G., and Hicks, T.J., (1996). "The pulse width modulated-constant temperature anemometer". *Measurement Science and Technology*, Vol. 7, pp. 1388-1395.
9. Haw, R.C., Foss, J.K. and Foss, J.F., (1989). "Vorticity Based Measurements in a Single Stream Shear Layer". Advances in Turbulence 2, editors Fernholz, H.H and Fiedler, H.E.. Springer-Verlag Berlin.
10. Hedley, T.B., and Keffer, J.F., (1974). "Turbulent/non-turbulent decisions in an intermittent flow". *Journal of Fluid Mechanics*. Vol. 64, pp. 625-644.

11. Landahl, M.T. and Mollo-Christensen, E. (1994). Turbulence and Random Processes in Fluid Mechanics, second edition. Cambridge University Press.
12. Morris, S.C., (2002). The Velocity and Vorticity Fields of a Single Stream Shear Layer. Ph.D Thesis, Michigan State University.
13. Phillips, O.M., (1972). "The entrainment interface". *Journal of Fluid Mechanics*. Vol 51, pp. 97-128.
14. Pope, S.B., (2000). Turbulent Flows. Cambridge University Press.
15. Potter, M.C. and Foss, J.F., (1975) Fluid Mechanics. Great Lakes Press.
16. Taylor, G.I., (1938). "The Spectrum of Turbulence". *Proceedings of the Royal Society of London, Series A*. 476-490.
17. Townsend, A. A, (1956). The Structure of Turbulent Shear Flow. Cambridge University Press.
18. Wallace, J.M. and Foss, J.F., (1995). "The Measurement of Vorticity in Turbulent Flows". *Annual Review of Fluid Mechanics*. Vol. 27, pp. 469-514.
19. Wygnanski, I. and Fiedler, H. E., (1970). "The two-dimensional mixing region". *Journal of Fluid Mechanics*, Vol. 41, pp. 327-361.

MICHIGAN STATE UNIVERSITY LIBRARIES



3 1293 02845 7657